SANDIA REPORT

SAND2012-0127
Unlimited Release
Printed January and 2012

Phonon Manipulation with Phononic Crystals

Ihab El-Kady, Roy H. Olsson III, Patrick E. Hopkins, Zayd C. Leseman,
Drew F. Goettler, Bongsang Kim, Charles M. Reinke, and Mehmet F. Su

Prepared by
Sandia National Laboratories
Albuquerque, New Mexico 87185 and Livermore, California 94550

Sandia National Laboratories is a multi-program laboratory managed and operated by Sandia Corporation,
a wholly owned subsidiary of Lockheed Martin Corporation, for the U.S. Department of Energy's
National Nuclear Security Administration under contract DE-AC04-94AL85000.

Approved for public release; further dissemination unlimited.

Sandia National Laboratories

Issued by Sandia National Laboratories, operated for the United States Department of Energy by Sandia Corporation.

NOTICE: This report was prepared as an account of work sponsored by an agency of the United States Government. Neither the United States Government, nor any agency thereof, nor any of their employees, nor any of their contractors, subcontractors, or their employees, make any warranty, express or implied, or assume any legal liability or responsibility for the accuracy, completeness, or usefulness of any information, apparatus, product, or process disclosed, or represent that its use would not infringe privately owned rights. Reference herein to any specific commercial product, process, or service by trade name, trademark, manufacturer, or otherwise, does not necessarily constitute or imply its endorsement, recommendation, or favoring by the United States Government, any agency thereof, or any of their contractors or subcontractors. The views and opinions expressed herein do not necessarily state or reflect those of the United States Government, any agency thereof, or any of their contractors.

Printed in the United States of America. This report has been reproduced directly from the best available copy.

Available to DOE and DOE contractors from
U.S. Department of Energy
Office of Scientific and Technical Information
P.O. Box 62
Oak Ridge, TN 37831

Telephone: (865) 576-8401
Facsimile: (865) 576-5728
E-Mail: reports@adonis.osti.gov
Online ordering: http://www.osti.gov/bridge

Available to the public from
U.S. Department of Commerce
National Technical Information Service
5285 Port Royal Rd.
Springfield, VA 22161

Telephone: (800) 553-6847
Facsimile: (703) 605-6900
E-Mail: orders@ntis.fedworld.gov
Online order: http://www.ntis.gov/help/ordermethods.asp?loc=7-4-0#online

SAND2012-0127
Unlimited Release
Printed January 2012

Phonon Manipulation with Phononic Crystals

Ihab El-Kady and Charles M. Reinke
Photonic Microsystems Technologies Department

Roy H. Olsson III, Zayd C. Leseman, Drew F. Goettler, and Bongsang Kim
MEMS Technologies Department

Patrick E. Hopkins
Microscale Science & Technology Department

Sandia National Laboratories
P.O. Box 5800
Albuquerque, New Mexico 87185-MS1082

Mehmet F. Su
Mechanical Engineering Department
University of New Mexico
1 University of New Mexico
Albuquerque, New Mexico 87131-0001

Abstract

In this work, we demonstrated engineered modification of propagation of thermal phonons, i.e. at THz frequencies, using phononic crystals. This work combined theoretical work at Sandia National Laboratories, the University of New Mexico, the University of Colorado Boulder, and Carnegie Mellon University; the MESA fabrication facilities at Sandia; and the microfabrication facilities at UNM to produce world-leading control of phonon propagation in silicon at frequencies up to 3 THz. These efforts culminated in a dramatic reduction in the thermal conductivity of silicon using phononic crystals by a factor of almost 30 as compared with the bulk value, and about 6 as compared with an unpatterned slab of the same thickness.

ACKNOWLEDGMENTS

The Principle Investigator, Ihab El-Kady, would like to thank Mahmoud Hussein, Alan McGaughey, Eric Shaner, Bruce Davis, Charles Harris, Thomas Beechem, Khalid Hattar, Janet Nguyen, Yasser Soliman, and Maryam Ziaei-Moayyed for their contributions to this research. Their efforts were invaluable in making this project a success.

CONTENTS

1. Introduction 11
   1.1. Thermoelectrics 11
      1.2.1. Thermoelectric Basics 11
      1.2.1. Challenges to Current TE Technologies 14
   1.2. Thermal Conductivity Applications of Phononic Crystals 15

2. Calculation of the Thermal Conductivity of Phononic Crystals 19
   2.1. Callaway-Holland Methods 19
   2.2. Bloch Mode Plane-Wave Expansion Technique 21
   2.3. Lattice Dynamics Technique 24
   2.4. Thermal Conductivity Calculations 25
      2.4.1. Density of States Method 25
      2.4.2. DOS with Slab Padding 27
      2.4.3. Dispersion Method with Mode Velocities 28
      2.4.4. Multi-Scale Method 29

3. Fabrication of Phononic Crystal Devices 31
   3.1. MESA Silicon-Fab 31
   3.2. Focused Ion Beam 33

4. Characterization of Thermoelectric Figure-of-Merit 39
   4.1. In-Plane Measurement Techniques 39
      4.1.1. Equilibrium Thermoelectric Measurements 39
      4.1.2. Suspended Island Technique 42
   4.2. Cross-Plane Thermal Conductivity Measurement 47
      4.1.2. Time Domain Thermoreflectance Technique 47
      4.2.1. Cross-Plane TDTR 47
      4.2.2. In-Plane TDTR 54

5. Results 55
   5.1. Experimental Measurements 55
      5.1.1. Measurement of Thermal and Electrical Conductivity Reduction in PnCs 55
      5.1.2. Dependence of Thermal Conductivity on Lattice Type and Topology 61
      5.1.3. Full ZT Characterization of PnC Samples 62

6. Conclusions and Future Outlook 67

7. References 69

Appendix A: Publications, Conferences, and Awards 73
   A.1. Journal Publications 73
   A.2. Conferences 73
      A.2.1. Organized Conferences 73
      A.2.2. Conference Presentations 73
   A.1. Patents 76

Distribution 77

FIGURES

Figure 1. A schematic diagram of a thermoelectric power generator. 11
Figure 2. A schematic diagram of a thermoelectric cooler. 12
Figure 3. Phononic crystal concept: a) Schematic of the phonon distribution in a bulk material. b) Schematic of the phonon distribution in a 2D PnC structure. c) Conceptual visualization of Bragg and Mie resonance scattering. d) SEM image of a fabricated PnC consisting of a square array of tungsten rods in a Si membrane; *a* is the lattice constant, *r* is the radius of the tungsten rods, and *t* is the membrane thickness (not shown in image). 15
Figure 4. a) Right panel shows the calculated band structure for a PnC composed of air holes in a Si matrix (blue) compared with the band structure f an unpatterned Si slab (red) of the same thickness "*t*". Left panel shows the corresponding PnC density of states (DOS). b) The integrated density of photon states for the PnC and Si slabs for the exemplar case of $a = 500$ nm, $r/a = 0.3$, and $t/a = 1.0$, where *a* is the lattice constant, *r* is the radius of the air hole and *t* is the slab thickness. 16
Figure 5. Classification of phonon spectrum. 17
Figure 6. Schematic of a TE PnC thermoelectric device. 18
Figure 7. Illustration of the computation domain used for the supercell PWE calculation, with air layers above and below the Si PnC later (red). The actual unit cell used in the simulations is shown in blue. 23
Figure 8. Bandgap map versus hole radius for a PnC composed of air holes in Si for various slab thicknesses. 24
Figure 9. Phononic dispersion of bulk Si for Γ–X (black curves), along with the corresponding dispersion from the Debye approximation for transverse (red dashed curve) and longitudinal (blue dashed curve) modes 26
Figure 10. The thermal conductivity of Si structures at room temperature as a function of L for the PnCs (unfilled squares), microporous solids (filled pentagons), nanomesh (filled diamond), and a suspended 500 nm thick Si films that is, an unpatterned Si slab (unfilled circle). The references are from [26]. The solid line represents predictions of the unpatterned slab at room temperature as a function of *L*. The dashed line represents predictions of the PnC thermal conductivity using DOS data from PWE calculations. 27
Figure 11. Integrated DOS for a Si slab of 500 nm thickness and a PnC of the same thickness and with 150 nm radius air holes. 28
Figure 12. A schematic of the thermal conductivity test structure design. A phononic crystal bridge is suspended from the substrate. Serpentine aluminum traces are installed at both the bridge center and both bridge ends. While heat is supplied at the center, the temperature gradient across the bridge is measured to extract device thermal characteristics. 32
Figure 13. Schematics of the fabrication process for the thermal conductivity measurement structures. 32
Figure 14. SEM images of fabricated simple cubic (SC) phononic crystal thermal conductivity test devices. 33
Figure 15. Schematic of a focused ion beam (FIB) system. Ions are extracted and then focused by multiple apertures and electromagnetic fields onto a sample. All of the FIB components and sample are under vacuum to prevent degradation. (Image courtesy of FEI) 33

Figure 16. Drawing of a liquid metal ion source. Liquid metal wets a sharp tip and an extractor lens extracts ions from the metal by using a high accelerating voltage in the kV range. 34
Figure 17. Sputter rates for various materials as a function of angle. Incident ion is Ga^+ at 30kV. Sputter rates were calculated using a Monte Carlo simulation package named TRIM. Solid black lines are interpolated values. 35
Figure 18. Fabrication process for creating a thin-freestanding membrane for PnCs. a) Cross sectional view of fabrication process. b) Released freestanding membrane. 36
Figure 19. Second fabrication method for creating a thin-freestanding PnC. a) Cross sectional view of fabrication process. b) Released freestanding PnC. 36
Figure 20. 30kV Ga+ ion penetration into 50 nm thick layer of Ni on top of 50 nm layer of Si. No ions reach the Si layer. 37
Figure 21. Trace resistance vs. temperature calibration data from a heated chuck measurement. a) Measured resistance values of heater trace and sensor trace with changing temperature. b) For both heater and sensor traces, their relative resistance changes were almost identical. The slope of this line is 0.0027. 39
Figure 22. Test setup diagram for thermal conductivity measurement. 40
Figure 23. An example plot of measured temperature vs. heating power plot (Device ID-7). Temperature difference across the phononic crystal bridge was measured using calibrated serpentine traces while heating power supplied at the bridge center was sweeping between 0 to 1 mW. 40
Figure 24. a) ANSYS FEM simulation model and b) equivalent thermal circuit model of thermal conductivity test structures. 41
Figure 25. An example of extracted thermal conductivity values using the models shown in Figure 24. At low heating power, the data are scattered. In this study, thermal conductivities values at 300 K were used, which were more reliable and repeatable. Red circles indicate when the temperature was ramping up and blue circles when ramping down. This plot is the measured data of Device ID-7. 42
Figure 26. SEM images of multi-use test platform for measuring thermal conductivity of phononic crystals. Both images are tilted 52° with respect to normal. a. Overview of suspended islands. b. Zoom-in of the SiN_x bridge connecting the heater and sensing islands. Pt pads on either side of the bridge provide a location for the PnCs to be welded on to the islands. 43
Figure 27. Process flow for fabrication of in-plane thermal conductivity test platform. 43
Figure 28. SEM images of PnCs measured with multi-use platform. a. Simple cubic PnC. b. Hexagonal PnC. 44
Figure 29. PnC mounted onto a thermal conductivity platform. 45
Figure 30. Electrical and Thermal Circuit of test platform. 46
Figure 31. Schematic of TDTR experiment built at Sandia as part of this LDRD. 51
Figure 32. TDTR data from a 117 nm Al film evaporated on a Si substrate along with the best fit from the thermal model. The thermophysical properties determined from the model best fits are $h_K = 210$ MW m^{-2} K^{-1} for the Al/Si interface and $\kappa = 141$ W m^{-1} K^{-1} for the Si substrate. 53
Figure 33. Thermal sensitivities in TDTR to h_K and κ of the substrate in 100 nm Al/Si and Al/SiO_2 systems. 53
Figure 34. The steps of image processing for the hole size measurement. a) SEM images containing 16~20 holes were taken. b) Complementary images were made. c) By setting the gray threshold, the hole boundaries are determined and the number of white pixels were counted to calculated hole areas and diameters. 56

Figure 35. Measured thermal conductivity values. The control device (Device ID-1), which has no holes, measured $k_m = 104$ W m^{-1} K^{-1}; this is consistent with literature values for 500 nm-thick single crystal silicon. 56
Figure 36. a) ANSYS FEM simulation for the effective conductivity reduction by introducing periodic holes. b) Volume reduction effect factors comparison between ANSYS FEM simulation model and Maxwell-Eucken model. 57
Figure 37. Comparison between $k_m/k_{m,control}$ (relative thermal conductivity with respect to the control device), $\sigma_m/\sigma_{m,control}$ (relative electrical conductivity with respect to the control device), and F_{FEM} (reduction effect factor from ANSYS FEM). The measured $\sigma_m/\sigma_{m,control}$ match very well with F_{FEM} for all Device IDs; some data points are difficult to distinguish because they exactly overlap with each other. However, the $k_m/k_{m,control}$ ratios are much smaller than F_{FEM} for all cases, inferring a reduction in the thermal conductivity that is beyond the contribution from the volume reduction effect. 58
Figure 38. Comparison of k_n versus limiting dimension with the same lattice constant. As the limiting dimension decreases, the k_n decreases, which indicates that incoherent scattering plays a significant role to reduce thermal conductivity of phononic crystals. Numbers adjacent the data points are the Device IDs. Each data point is averaged from 6 measured devices. 59
Figure 39. Comparison of k_n versus lattice constant with the same limiting dimension. Even with the same limiting dimensions, k_n decreases, as the lattice constant increases, which infers that incoherent scattering is not the only mechanism for the thermal conductivity reduction. Numbers adjacent the data points are the Device IDs. Each data point is averaged from 6 measured devices. 60
Figure 40. Hypothetical schematic explaining coherent scattering enhancement at a given limiting dimension. As the lattice constant increases, the two Bragg resonant frequencies approach each other, opening a phononic bandgap at some point which widens as the lattice constant increases. 60
Figure 41. Calibration data from a test platform. Black refers to the heater island and blue refers to the sensor island. Both the heater and sensor showed linear trends across a 40° C temperature range. 61
Figure 42. Plot of input power vs. heater resistance for the hexagonal PnC. 62
Figure 43. A schematic of the *ZT* measurement test structure design. A phononic crystal bridge is suspended from the substrate. One half of the bridge is doped n-type while the other half is doped p-type. Electrical contacts are provided at the bridge ends to measure the amount of thermoelectrically induced current and voltage when heat is supplied at the bridge center. 63
Figure 44. Schematics of the fabrication process for the *ZT* measurement structures. 64
Figure 45. Sumary of predicted *ZT* enhancement for the fabricated PnC devices. 65

TABLES

Table 1. Material parameters used in PWE simulations of Si PnCs 24
Table 2. Summary of designed hole pitches and diameters. 55
Table 3. Summary of the measured thermal conductivity values (300 K). 56
Table 4. Comparison between $k_m/k_{m,control}$ (relative thermal conductivity with respect to the control device), $\sigma_m/\sigma_{m,control}$ (relative electrical conductivity with respect to the control device), and F_{FEM} (modeled volume reduction effect from ANSYS FEM). 58

Table 5. Summary of k_n, relative thermal conductivity values ($k_m/k_{m,control}$) normalized by ANSYS FEM volume reduction effect factors (F_{FEM}).. 59
Table 6. Results of thermal conductivity for hexagonal and simple cubic PnC.......................... 62

NOMENCLATURE

DOS	density of states
IBZ	irreducible Brillouin zone
FEM	finite element modeling
FIB	focused ion beam
LD	lattice dynamics
MEMS	microelectromechanical systems
PnC	photonic crystal
PWE	plane-wave expansion
RLV	reciprocal lattice vector
RTD	resistance temperature detector
SEM	scanning electron microscope
SNL	Sandia National Laboratories
SOI	silicon-on-insulator
TCR	temperature coefficient of resistance
TDTR	time domain thermoreflectometry
TE	thermoelectric
ZT	dimensionless thermoelectric figure-of-merit

1. INTRODUCTION

1.1. Thermoelectrics

1.2.1. Thermoelectric Basics

The **thermoelectric effect** is defined as the process whereby a sustained temperature gradient across a material generates a proportional electric potential difference, and vice versa. On an atomic scale the effect can be understood by noting that an applied temperature gradient causes charged carriers in the material to diffuse from the hot side to the cold side in accordance with the second law of thermodynamics hence inducing a thermal current and consequently a potential difference. Such a phenomenon can thus be used to transform heat into electricity, in which case it is commonly referred to as the "*Peltier effect*" and has the potential to enable the recycling of waste heat or thermal energy, a natural outcome of almost all artificial and natural processes, to the more useful form of electrical energy. While the thermoelectric effect can and was initially observed in metals, we are particularly interested in the case where the material in use is a semiconductor for reasons that will become self-evident later on in our discussions.

Consider for example the scenario depicted in Figure 1. Here an n-type and a p-type semiconductor are both electrically connected from at one end and placed in contact with a heat source (e.g., a microprocessor) meanwhile the other end is maintained at a lower temperature (e.g., a heat sink). Because of the temperature gradient, the carriers in both legs start diffusing from the hot side to the cold side. If both legs on the cold side are then connected to a load resistor, the difference in the carrier type in both legs (electrons in the n-type, and holes in the p-type) generate an electric current that flows in the direction of the arrows shown in Figure 1. The potential drop across the load resistor can now be used to derive an appropriate electric device assuming enough power is generated. In this scenario, in is clear that the amount of electric power generated depends directly on the temperature gradient ΔT that can be sustained across the thermoelectric module.

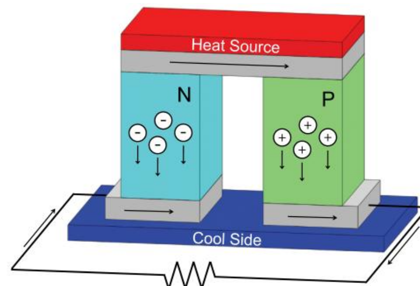

Figure 1. A schematic diagram of a thermoelectric power generator.

Conversely, by applying an external voltage and managing the polarity of the electrical connections, the Peltier effect can be used for cooling applications. Consider for example the case depicted in Figure 2. Here the applied electric potential forces the carriers to migrate from the cold surface to the hot surface resulting in the decrease in temperature of the cold side and an increase in that of the hot side. Alternately, in this scenario of operation, the amount of cooling

or temperature drop on the cold side is directly proportional to the applied electric voltage, which also directly depends on the temperature difference ΔT between the hot and the cold sides of the thermoelectric module.

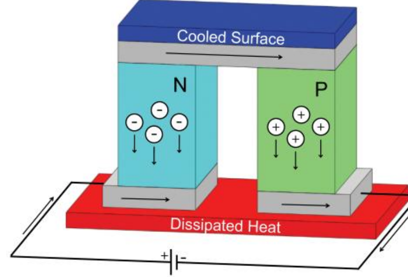

Figure 2. A schematic diagram of a thermoelectric cooler.

Whether the thermoelectric (TE) device is operated as a cooler or a power generator, it is evident that the ability to mold and control the direction of motion of the charge carriers in the system is key to the operation of the TE device. In fact the performance of a material's efficacy for use in a TE setting is often quantified by the dimensionless figure of merit, *ZT* [1-3]:

$$ZT = \frac{S^2 \sigma}{\kappa} T, \tag{1}$$

where *S* is the Seebeck coefficient, σ is the electrical conductivity, κ is the thermal conductivity and *T* is the temperature. For an actual TE module with both n-type and p-type legs, the expression for the figure of merit is slightly more complicated and takes on the form:

$$Z\overline{T} = \frac{(S_p - S_n)^2 \overline{T}}{\left(\sqrt{\rho_n \kappa_n} + \sqrt{\rho_n \kappa_n}\right)^2}. \tag{2}$$

Here, the subscripts *n* and *p* denote the semiconductor leg-type, and $\overline{T}$ denotes the average temperature of the hot and the cold sides of the TE module.

The importance of the figure of maximizing merit *ZT* becomes quite evident by examining the maximum efficiency $\eta_{\max}$, or the maximum coefficient of performance $\varphi_{\max}$ of a TE power generation or cooling unit respectively [3]:

$$\eta_{\max} = \frac{T_H - T_C}{T_H} \frac{\sqrt{1 + Z\overline{T}} - 1}{\sqrt{1 + Z\overline{T}} + \left(\frac{T_C}{T_H}\right)}, \tag{3}$$

$$\varphi_{\max} = \frac{T_C}{T_H - T_C} \frac{\sqrt{1 + Z\overline{T}} - \left(\frac{T_H}{T_C}\right)}{\sqrt{1 + Z\overline{T}} + 1}. \tag{4}$$

In Eqs. (3) and (4), the subscripts H and C refer to the hot and the cold sides of the TE module, respectively.

It is worthwhile looking at the composition of *ZT* to gain insight into the role of each of its fundamental components. *S*, is the open circuit voltage and is a measure of the magnitude of an induced thermoelectric voltage in response to a temperature difference across that material, while σ measures the ability of the charge carriers to diffuse from one side of the TE device to the

other. The increase in the value of both quantities is thus favorable form a TE deice perspective, and hence their appearance in the numerator the in expression in Eq. (1). κ, on the other hand measures the ability of heat to freely flow from the hot side to the cold side, thus resulting in the minimization of ΔT across the TE device. The minimization of κ is thus favorable for optimal TE performance, hence its appearance in the denominator of Eq. (1).

When attempting to optimize TE performance, it is worth paying special attention to the interdependence of the 3 Z components. For example, since S is a measure of the entropy per carrier [2], it is generally maximized by increasing the disorder in the system, while σ, on the other hand, is a measure of the ability of the charge carriers to navigate the system, and hence decreases with increased disorder (e.g. scattering) in the system. This inverse relationship between S and σ is best captured in the formulation of the Mott relation [4]:

$$S \sim \left.\frac{d\ln(\sigma(\varepsilon))}{d\varepsilon}\right|_{\varepsilon=\varepsilon_F} = \left.\frac{1}{\sigma}\frac{d\ln(\sigma(\varepsilon))}{d\varepsilon}\right|_{\varepsilon=\varepsilon_F}, \tag{5}$$

where ε is the carrier energy and ε_F is the Fermi level energy.

While both S and σ are governed by the electrical properties of the system, κ on the other hand is a composite quantity that has an electronic and a phononic component. Bearing in mind that in a semiconducting material κ is dominated by the phononic contribution, and that phonons do not carry any electrical charge, they will simply act to quench the temperature difference between the hot and cold sides of a TE module without contributing to the generation of the electrical current in a TE generation scheme (Figure 1); meanwhile, since they are unaffected by the biasing potential in Figure 2, they would flow opposite to the direction of the charge carriers from the hot side to the cold side, thus leading to a decrease in the cooling performance.

Thus the most obvious way to increase ZT is by attempting to suppress the phonon contribution to κ, leaving the electron component unaltered. Fundamentally, such approaches make use of the fact that the electron mean free path in most TE materials (especially the most popular semiconductor-based ones) is at least an order of magnitude smaller than that of the phonons. This allows for a large percentage of the thermal conductivity to be reduced with minor perturbations to the electrical conductivity. Examples of such approaches are phonon control based on texturing the surface to increase phonon scattering or shrinking the effective cross-section in the direction of current flow to prevent bulk propagation, much like a cutoff waveguide. The waveguide cutoff approach, however, is only capable of cutting-off low frequency phonons, rather than the high frequency phonons that are most relevant to heat transfer. Surface texturing, on the other hand, suppresses only surface phonon states that lie within the narrow spectral range comparable to the texturing length scale. Thus, both approaches lack the fundamental ability to manipulate a wide spectral range of phonons at the relevant terahertz (THz) frequencies, not to mention the fact that the introduced hard interfacial boundaries inadvertently scatter electrons, resulting in a simultaneous decrease in both σ and κ, thus yielding no net gain in ZT.

1.2.1. Challenges to Current TE Technologies

The interdependence of the 3 Z components makes it extremely difficult to optimize all 3 of them concurrently. As such, almost all existing literature on Z employ an "Edisonian" approach whereby the focus is on the enhancement of only one of its three components, leaving the remaining two to chance. Even when successful in enhancing the TE performance, one of the most fundamental challenges is the transitioning of new TE technologies into actual deployed devices. There, concerns about practicality, integration, and mass production on a large scale are major barriers. For example, while it has proven to be a difficult task to ensure the increase in σ at the expense of κ, given that electrons conduct both heat and electricity, nanotubes have achieved just that by promoting the ballistic transport of electrons though the hollow core of the tube. The major drawback in such an approach remains one of device development and the integration of such nanotubes into realistic devices for applications.

Other approaches like super lattices [5-7] have relied on lattice matching between the different layers in the stack, thus enabling the electrons to tunnel from one layer to the next with minimal scattering. The issue here is that the thicknesses of the individual stack layers are on the angstrom length scale and are usually deposited via atomic layer deposition techniques. This renders mass production extremely difficult and very costly. Furthermore, a common drawback in both the nano-wire/tube based approaches and those that rely on super lattices is the fact that the ZT enhancement is in the vertical direction parallel to the length of the wire/tube or in the stacking direction. Given the small size of the overall device, this limits the maximum sustainable temperature gradient and hence caps the TE operational efficiency.

Furthermore, given the strong interdependence of S and σ and their opposite correlation to carrier entropy, it has been suggested that one possible way to increase S with minimal effects to σ is via quantum confinement and reduced dimensionality [8, 9]. Here the idea is to maximize the entropy per carrier, where the reduction in dimensionality automatically increases the carrier contribution to entropy and hence automatically increases S. To avoid the issues pertaining to one-dimensional systems described above, the idea is then to operate in what is equivalent to a two-dimensional electronic system. This, however, implies a thin-membrane like topology whose cross-section is on the order of the electron mean free path, i.e. a few nanometers. Despite the novelty of the idea, the practicality and integration of such a solution pose fundamental challenges.

Thus, from a practical standpoint, any proposed TE solution aiming at enhancing ZT must at the same time observe the practicality requirement. In other words, what is needed is a TE solution where a large spatial separation between the hot and cold sides can be maintained. Furthermore, such a solution must be amenable to mass production and lend itself with ease to plausible integration schemes. It is our thesis in this work that that phononic crystals can act as the vehicle for that solution. In the next few sections, we define what a phononic crystal is, explain how it operates, and outline the path with which it can be used to enhance TE performance. We further provide experimental and theoretical evidence on the possibility of doubling the ZT value of material systems that are amenable to the phononic crystal technology.

1.2. Thermal Conductivity Applications of Phononic Crystals

A phononic crystals (PnC) is the acoustic analogue of a photonic crystal, and typically consists of a periodic arrangement of scattering centers embedded in a homogeneous background matrix with a lattice spacing comparable to the acoustic wavelength [10] (Figure 3b and d). When properly designed, a superposition of Bragg and Mie resonant scattering results in the opening of a frequency band over which there can be no propagation of elastic waves in the crystal, regardless of direction [11, 12]. In addition to the coherent scattering mechanisms responsible for the bandgap creation, coherent scattering also results in a rich complicated dispersion spectrum accompanied by a redistribution of the phononic density of states (DOS). This new anomalous dispersion spectrum, shown in Figure 4a as compared to the unperturbed bulk material, results in the creation of dispersion-less (flat) bands where the phonon group velocity is greatly reduced, in addition to negatively sloping bands (negative group velocities) or backward propagation of phonons (backscattering).

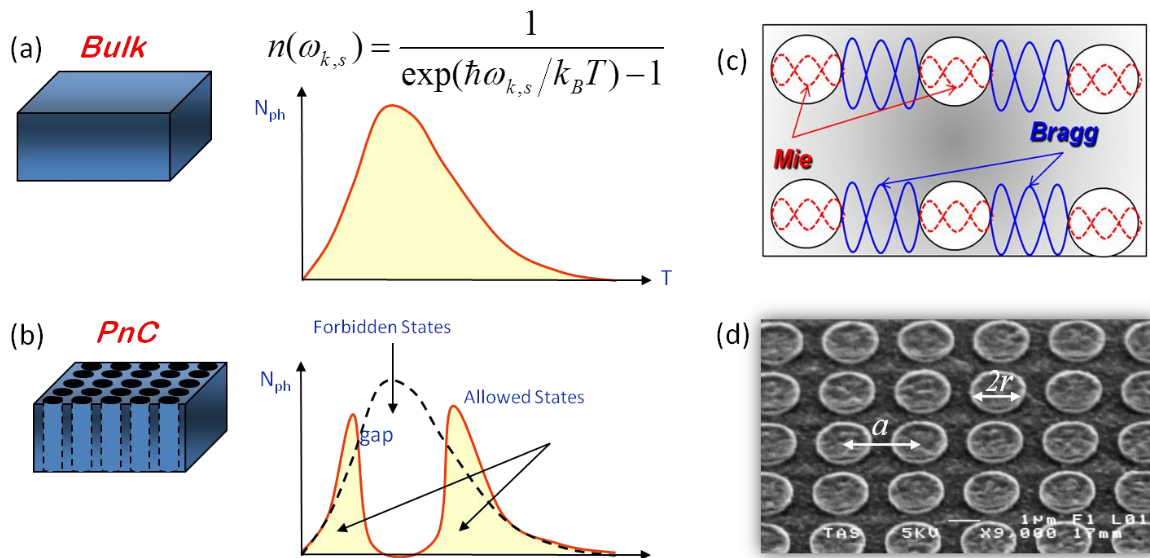

Figure 3. Phononic crystal concept: a) Schematic of the phonon distribution in a bulk material. b) Schematic of the phonon distribution in a 2D PnC structure. c) Conceptual visualization of Bragg and Mie resonance scattering. d) SEM image of a fabricated PnC consisting of a square array of tungsten rods in a Si membrane; *a* is the lattice constant, *r* is the radius of the tungsten rods, and *t* is the membrane thickness (not shown in image).

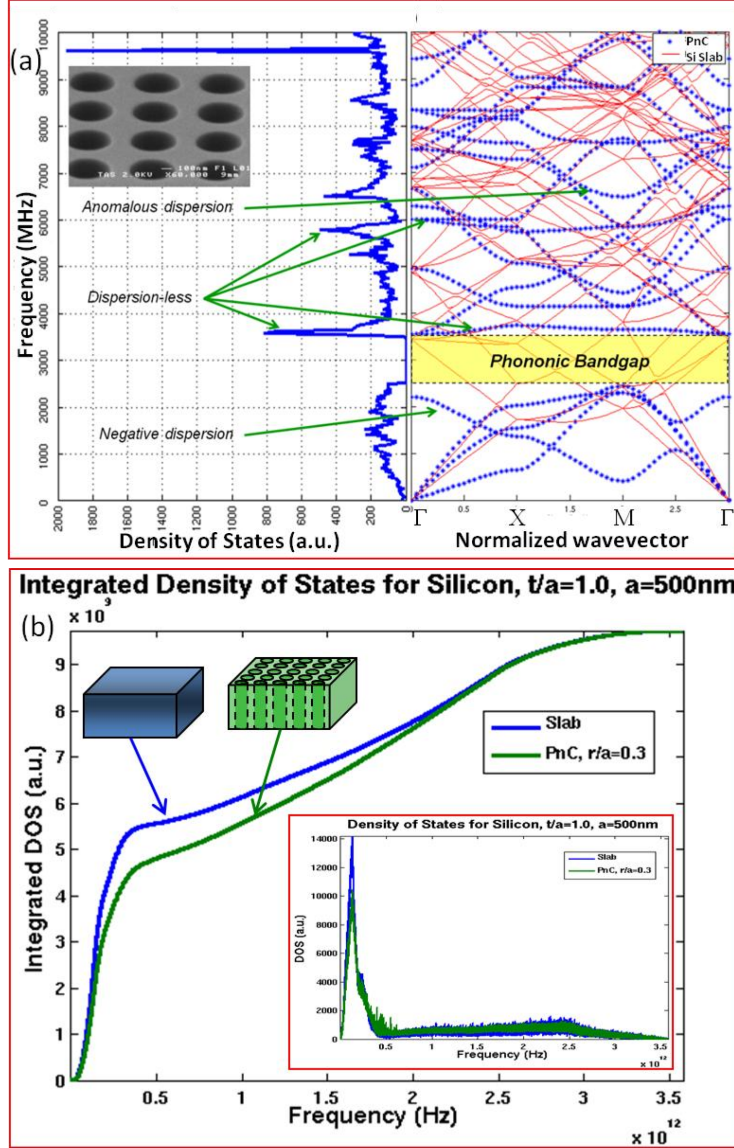

Figure 4. a) Right panel shows the calculated band structure for a PnC composed of air holes in a Si matrix (blue) compared with the band structure f an unpatterned Si slab (red) of the same thickness "*t*". Left panel shows the corresponding PnC density of states (DOS). b) The integrated density of photon states for the PnC and Si slabs for the exemplar case of a = 500 nm, r/a = 0.3, and t/a = 1.0, where a is the lattice constant, r is the radius of the air hole and t is the slab thickness.

In general we can classify the phonon spectrum in any material into 2 regions: *acoustic* and *optical* phonons (see Figure 5). At a given temperature, the contribution of these phonons to κ is mandated by their mean free path and the Boltzman distribution for a given material dispersion. In general, depending on the thickness of the slab, up to ~30% of the thermal conductivity can come from the optical branches [13, 14]. To understand how one can modify κ, we use the Holland-Callaway model description:

$$\kappa = \frac{1}{6\pi^2} \sum_j \int_q \frac{\hbar^2 \omega_j^2(q)}{k_B T^2} \frac{\exp\left[\frac{\hbar \omega_j(q)}{k_B T}\right]}{\left(\exp\left[\frac{\hbar \omega_j(q)}{k_B T}\right] - 1\right)^2} v_j^2(q) \tau_j(q) q^2 dq \tag{6}$$

where $\hbar$ is the reduced Planck's constant, $\omega(q)$ is the phonon dispersion, k_B is the Boltzmann constant, T is the phonon temperature, $v(q) = \partial\omega(q)/\partial q$ is the phonon group velocity, $\tau_j(q)$is the phonon scattering time, and q is the wavevector. Here, κ is summed over all phonon modes "j". Assuming only Umklapp and boundary scattering: $\tau_j(q) = \left(\tau_{U,j}^{-1}(q) + v_j(q)/L\right)^{-1}$, where $\tau_{U,j}^{-1}(q) = AT\omega^2(q)\exp[-B/T]$, A and B are dispersion-fit coefficients, and L is the minimum distance between sample boundaries (minimum feature size). Thus, in order to modify κ, we have to engineer the dispersion $\omega(q)$ or the phonon lifetime $\tau(q)$.

The periodic mechanical impedance mismatch in a PnC [15] results in anomalous dispersion not found in a homogeneous material. This includes the creation of phononic bandgaps, dispersionless (low group velocity) bands, and even negative dispersion (negative group velocity or backward scattering) bands. Figure 4 shows an illustration of these phenomena in a SiC/air PnC. The result is the complete inhibition of phonon propagation in the bandgap region and generally a large reduction in the phonon mobility elsewhere. All such phenomena are termed "coherent scattering" and are manifested only in the frequency ranges where the phonon wavelength is of the same order of the PnC lattice periodicity. Thus, in PnCs with minimum feature sizes on the order of 250 nm, we predict that these coherent effects will affect acoustic Si phonons up to the validity of the Debye material limit, i.e., 15 THz for the acoustic longitudinal phonons and 10 THz for the transverse acoustic ones. However, coherent scattering can also affect ultra-high frequency phonons in an indirect yet effective manner. This is due to the fact that 30% of all optical phonon relaxation processes involve an acoustic phonon [16]. Thus by suppressing the acoustic phonon population we indirectly inhibit the optical phonon relaxation by up to 30% and hence limit their contribution to thermal conductivity.

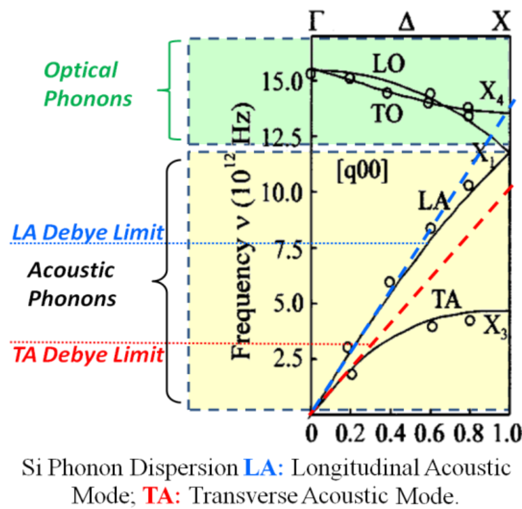

Figure 5. Classification of phonon spectrum.

In addition to coherent scattering, incoherent boundary scattering events are concurrently present in the PnC lattice. These are instigated by the simple existence of the scattering centers irrespective of their arrangement. The dominant factor here is the edge-to-edge separation of the scattering centers, or minimum feature size *L*, which caps the phonon lifetime τ. Incoherent scattering influences phonons across the high frequency bands, provided that their corresponding wavelengths are **smaller than** or **on the order of** the minimum feature size of the PnC lattice. This ultimately results in a reduction in the thermal conductivity by as much as 90% [15] with minimal effects on the electrical conductivity.

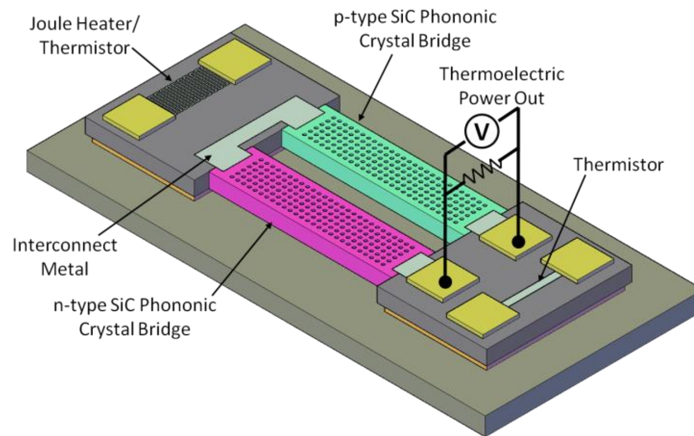

Figure 6. Schematic of a TE PnC thermoelectric device.

The overall effect is anticipated to be the doubling of the thermoelectric figure of merit *ZT* over that of the underlying material, in this case Si. Given the fact that the PnC technology is portable to any material set, we anticipate that this factor of 2 enhancement in *ZT* can be realized in any material system subject to it lending itself to PnC fabrication and assuming that κ is phonon dominated. This result promises to have profound implications for TE technology, and we anticipate that it may indeed lead to the creation of the next generation of high-*ZT* TE devices, such as the schematic shown in Figure 6.

A detailed description of the experimental and theoretical validation of these results is given in the following sections.

2. CALCULATION OF THE THERMAL CONDUCTIVITY OF PHONONIC CRYSTALS

The thermal conductivity of a crystalline solid is directly dependent on the phonon band structure. Properties such as the phonon group velocity, heat capacity, and phonon scattering rates can be extracted from the phonon dispersion. The Callaway-Holland method combines these properties to predict thermal conductivity, and is applicable for materials where the thermal conductivity is dominated by phonon, rather than electron, transport. The plane wave expansion (PWE) technique is employed in this work to determine dispersion for various PnC systems, with the material modeled as a continuum at the macro-scale. This information is incorporated into the Callaway-Holland model, while also the lattice dynamics (LD) behavior for the host bulk material is utilized.

2.1. Callaway-Holland Methods

There are two general forms of the Callaway-Holland model for the calculation of the thermal conductivity from phonon dispersion. The difference lies in whether the dispersion information is integrated over frequency space (which includes a density of states calculation) or wave vector space. Both forms require knowledge of the modal velocities, heat capacity, and scattering lifetimes deduced from the dispersion. One form of this model may be more convenient to implement over the other depending on variables such as the occurrence of branch crossings in frequency versus wave vector space and the ease of calculating the phonon density of states of a given system.

Both forms of the Callaway-Holland originate from the first law of thermodynamics, where energy is conserved as it is transferred by phonons through the lattice. The Boltzmann transport equation further defines the problem for crystalline structures by relating the change of phonon distribution to an applied temperature gradient and wave speed through the medium. The three factors considered when calculating thermal conductivity κ are: the volumetric specific heat C_p of the phonons, the group velocity at which the phonons travel through the lattice $\vec{v}_g$, and their rate of scattering τ. Thus, the thermal conductivity can be calculated by integrating these factors together over the non-dimensional wave vector q and summed for all polarization branches λ [17]:

$$\kappa = \sum_{\lambda} \int (v_g(q,\lambda) \cdot \hat{l})^2 C_p(\vec{q},\lambda)\, \tau(\vec{q},\lambda)\, d\vec{q}. \tag{7}$$

In Eq. (7), the phonon heat capacity is expressed per volumetric unit a^3 and the phonon velocity is dotted with the unit vector l along the principle axes. A change of variable from q to k, which has dimensions of m^{-1}, is done to incorporate the lattice constant a:

$$d\vec{q} = d\vec{k}a/2\,. \tag{8}$$

A factor of 2π appears in the formula to account for the volume of the Brillouin zone geometry of face-centered cubic structures. This enables us to replace C_p with C_{ph}, which is the heat capacity expressed in units of joules per Kelvin. Now Eq. (7) becomes

$$\kappa = \frac{1}{(2\pi)^3} \sum_{\lambda} \int C_{ph}(k,\lambda) (\vec{v}_g(k,\lambda) \cdot \hat{l})^2 \tau(k,\lambda)\, d\vec{k}\ . \tag{9}$$

The material in this case is assumed to be isotropic, allowing for the variable of integration k to be evaluated over the volume of a sphere and expressed as a scalar, that is

$$\int d\vec{k} = 4\pi\int_0^{2\pi/a} k^2 dk \,. \tag{10}$$

This is an approximation to the near-spherical shape of the first Brillouin zone. In addition, the dot product in Eq. (9) for a 3D system or three coordinate directions is reduced to $3^{-1/2}$:

$$(\vec{v}_g(k,\lambda)\cdot\hat{\imath}) = \frac{v}{\sqrt{3}} \,. \tag{11}$$

The final form of the Callaway-Holland equation in k-space is expressed for a face-centered cubic lattice along the Γ-X path (0 to $2\pi/a$) as

$$\kappa = \frac{4\pi/3}{(2\pi)^3}\sum_{\lambda}\int_0^{2\pi/a} C_{ph}(k,\lambda)v_g^2(k,\lambda)\tau(k,\lambda)k^2 dk \,. \tag{12}$$

The heat capacity C_{ph} measures the energy of each phonon mode and incorporates the Boltzmann-Einstein distribution to account for quantum effects at low wavenumbers. Here ω is the phonon frequency, k_B is the Boltzmann constant, $\hbar$ is the reduced Plank's constant, and T is the temperature:

$$C_{ph}(k,\lambda) = k_B\left(\frac{\hbar\omega(k,\lambda)}{k_B T}\right)^2 \frac{\exp(\hbar\omega(k,\lambda)/k_B T)}{\left[\exp(\hbar\omega(k,\lambda)/k_B T)-1\right]^2} \tag{13}$$

The phonon group velocity is calculated by taking the derivative of the phonon frequency with respect to the wave number:

$$v_g(k,\lambda) = \frac{\partial\omega(k,\lambda)}{\partial k} \tag{14}$$

Finally, the phonon scattering lifetime can be broken into three major components based on the Umklapp (τ_U), impurity (τ_I), and boundary (τ_B) scattering processes. The inverse of these variables are summed according to Matthiessen's rule, which enables certain terms to be dominant over the others:

$$\begin{aligned}\tau(k,\lambda) &= \left(\tau_U^{-1}(k,\lambda) + \tau_I^{-1}(k,\lambda) + \tau_B^{-1}(k,\lambda)\right)^{-1} \\ &= \left(AT\omega^2(k,\lambda)e^{-B/T} + D\omega^4(k,\lambda) + c/L\right)^{-1}\end{aligned} \tag{15}$$

The Umklapp scattering, which models the phonon-phonon interactions, has two fitted parameters A and B. The impurity scattering (e.g., from the natural defects of the material) are accommodated by the parameter D. The final term of boundary scattering incorporates surface interactions, or more generally any interactions with interfaces. The boundary scattering is dependent on the speed of sound through the material c (more accurately evaluated as $v(k,\lambda)$) and the minimum feature length L, which is determined by boundaries, grains, or voids introduced within the material.

We use the relationship between the scalar component of the group velocity and that of the phase velocity,

$$v_p(k,\lambda) = \frac{\omega(k,\lambda)}{k} \,, \tag{16}$$

to change the variable of integration of the Callaway-Holland formulation from wave vector space to frequency space. This relationship allows us to modify the integrand as

$$k^2 dk = \frac{\omega^2}{v_p^2}\frac{dk}{d\omega}d\omega = \frac{\omega^2}{v_p^2}\frac{1}{v_g}d\omega \tag{17}$$

This expression can be further simplified by introducing the phonon density of states per unit volume (note that $N=\int k^2 dk$) defined as [18]:

$$D(\omega,\upsilon) = \frac{dN}{d\omega} = \frac{dN}{dk}\frac{dk}{d\omega} = k(\omega,\upsilon)^2 \frac{1}{v_g(\omega,\upsilon)} = \frac{\omega^2}{v_p(\omega,\upsilon)^2}\frac{1}{v_g(\omega,\upsilon)}. \tag{18}$$

The final form of the Callaway-Holland model in frequency space can thus be written as

$$\kappa = \frac{1}{6\pi^2}\sum_{\upsilon}\int_0^{\omega_0} C_{ph}(\omega,\upsilon)v_g^2(\omega,\upsilon)\,\tau(\omega,\upsilon)\,D(\omega,\upsilon)d\omega \tag{19}$$

where υ is the available states (e.g., branch polarizations) across $d\omega$. This is the most general form of the frequency space version of the model; however, due to the difficulty in identifying the mode type in the phonon dispersion calculations (especially when the band structure is complex), Eq. (19) is implemented in this work with the following approximation

$$\kappa \cong \frac{1}{6\pi^2}\int_0^{\omega_0} C_{ph}(\omega)v_g^2(\omega)\,\tau(\omega)\left(\sum_{\upsilon} D(\omega,\upsilon)\right)d\omega \tag{20}$$

where $C_{ph}(\omega)$ is the heat capacity at a given frequency irrespective of the dispersion branch, $v_g(\omega)$ is the group velocity of the bulk material at a given frequency averaged over the first three branches, $\tau(\omega)$ is the scattering time constant calculated according to Eq. (15) at a given frequency irrespective of the dispersion branch and using $v_g(\omega)$ for the sound velocity, and the density of states is summed over all dispersion branching prior to integrating.

2.2. Bloch Mode Plane-Wave Expansion Technique

Many methods are available for calculating the transmission and dispersion properties of PnCs, depending on the behavior being studied; whether time-domain or frequency-domain information is desired; and what *a priori* assumptions, if any, can be made. Perhaps the most commonly used of these techniques are finite-difference time-domain (FDTD), finite element modeling (FEM), and plane-wave expansion (PWE). In this work, we primarily utilized the FDTD and PWE methods, with lattice dynamics (LD) used solely for the calculation of the bulk phonon dispersion of Si. FDTD is useful for simulating structures having finite dimensions (rather than infinitely periodic) and obtaining transmission and reflection data that can be used to directly compare with experimental results. However, for revealing phononic bandgaps and calculating the heat transport properties of PnCs, it is often more appropriate to assume and infinite crystal and calculate the dispersion behavior of the unperturbed PnC. Thus, PWE was used extensively in this study, since it provides frequency and spatial profile information about the dispersion of all elastic modes allowed by the periodicity of the PnC. The technique and its application to thermal conductivity modeling are described here.

The plane-wave expansion technique [19, 20] operates under the assumption of Bloch's theorem for periodic media, which asserts that the elastic wave displacement $\boldsymbol{u}(\boldsymbol{r})$ can be written in the following form:

$$\boldsymbol{u}(\boldsymbol{r}) = \boldsymbol{u}_{\boldsymbol{k}} e^{i\boldsymbol{k}\cdot\boldsymbol{r}}, \tag{21}$$

where $\boldsymbol{r}$ is the position vector, $\boldsymbol{k}$ is wave vector and $\boldsymbol{u_k}$ is a periodic function having the same periodic structure as the materials that make up the PnC. The density $\boldsymbol{\rho}(\boldsymbol{r})$ and elastic stiffness tensor $\boldsymbol{C}(\boldsymbol{r})$ can be written as expressions having corresponding forms. Using Fourier analysis, the components of the displacement can be expanded as

$$u_j = \sum_{\boldsymbol{G}} u_{\boldsymbol{G}}^j e^{i(\boldsymbol{k}+\boldsymbol{G})\cdot\boldsymbol{r}-i\omega t}, \text{ where } i, j, k = 1-3 \tag{22}$$

where $\boldsymbol{u_G}$ is a Fourier coefficient, ω is the angular frequency, t is time, and $\boldsymbol{G}$ is the reciprocal lattice vector. This Fourier expansion can be substituted into the second-order elastic wave equation for displacement fields with no body force, written as

$$\rho(\vec{r})\ddot{u}_j(\vec{r},t) = \sum_{j,k,l} \frac{\partial}{\partial x_i}\left(C_{ijkl}(\vec{r}) \frac{\partial u_k(\vec{r},t)}{\partial x_l} \right), \tag{23}$$

where x_i is the i-th component of the position vector. After expanding the resulting set of equations and collecting like terms, an eigenvalue problem can be constructed of size $3N$ x $3N$, where N is the number of reciprocal lattice vectors (RLVs) used to expand the displacement field. The eigenvalues of this equation system correlate with the frequencies of each mode at a given point in k-space; hence the dispersion diagram for a PnC is calculated by finding the eigenvalues at consecutive points defining the irreducible Brillouin zone (IBZ) of the periodic lattice. The corresponding eigenvectors contain information about the spatial distribution of the elastic displacement field, and can be used to reconstruct the displacement field of a given PnC mode.

While this technique as presented is perfectly suitable for 2D simulations or simulations of 3D that are periodic in all three dimensions, an adjustment must be made to simulate planar PnC structures that have a finite thickness in the third dimension. In this case, the supercell method [21] can be used to account for the finite thickness of the PnC slab. With this modification, the Fourier structure factor components are calculated for a full 3D structure, where a slab of air is included above and below the slab to isolate it elastically from the adjacent virtual" unit cells in the vertical direction, as shown schematically in Figure 7. Although RLVs corresponding to the third dimension are now included, the z-component of the wave vector is zero, since there is not actual periodicity in that direction. Additionally, several terms in the eigenvalue problem that dropped out in the 2D case can no longer be neglected, resulting in a significantly more complicated calculated at each k-point. Note that unlike in Ref. [21], where the Fourier structure factor components were calculated analytically, the code used for this study used a more universal fast-Fourier transform (FFT) implementation.

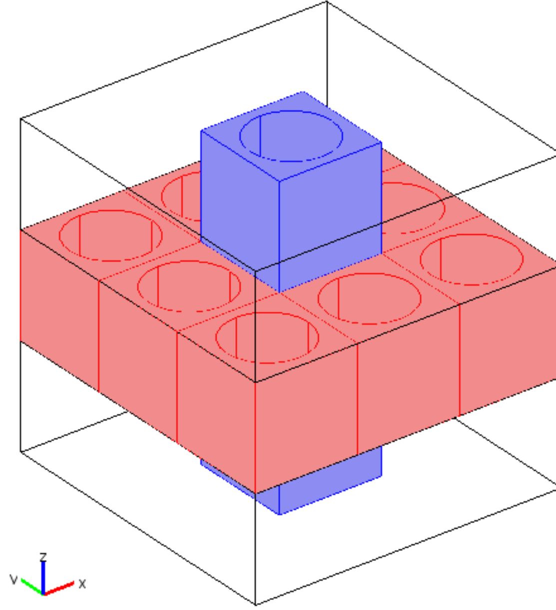

Figure 7. Illustration of the computation domain used for the supercell PWE calculation, with air layers above and below the Si PnC later (red). The actual unit cell used in the simulations is shown in blue.

A notable improvement to the plane-wave expansion scheme can be implemented in a straightforward fashion using the reduced Bloch-mode expansion (RBME) technique. This modification allows for convergence of the calculated dispersion using fewer RLVs by expanding the displacement field with calculated solutions to the eigenvalue problem at nearby *k*-points. Thus, the full $3N$ x $3N$, problem need only be solved the high-symmetry points of the IBZ, after which those Bloch wave solutions are used in place of the ordinary plane waves to expand the fields for the intermediate points. This can result in more than an order of magnitude reduction in the required computation time for calculation of the dispersion diagram of a PnC, greatly speeding up parametric sweep calculations used to plot the bandgap map of a given PnC topology. The resulting bandgap map for a finite-thickness PnC composed of cylindrical air holes in a Si matrix is shown in Figure 8, where complete bandgap formation is observed only for normalized radii $r/a > 0.4$ and slab thicknesses between $t/a = 0.25$ and 2 [22]. The material properties assumed in the simulation are given in Table 1; notice that non-physical parameters were used for “air” to ensure stability of the code.

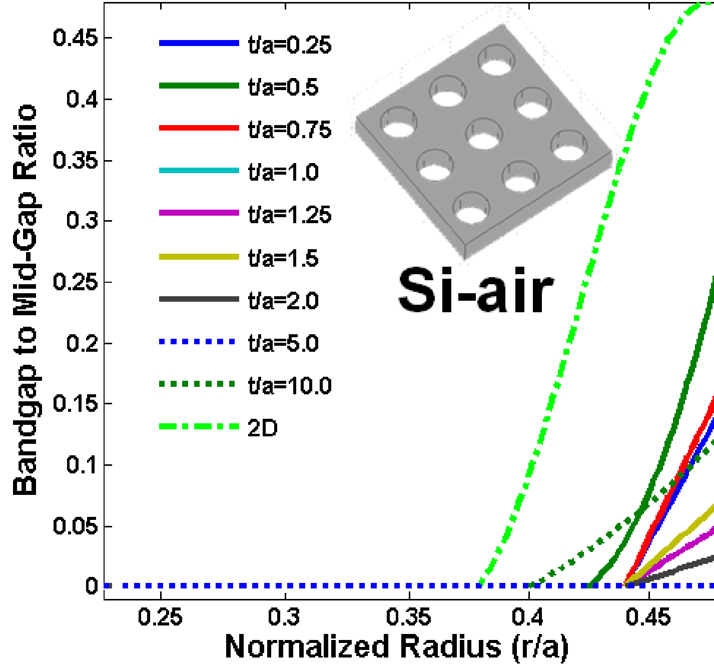

Figure 8. Bandgap map versus hole radius for a PnC composed of air holes in Si for various slab thicknesses.

Table 1. Material parameters used in PWE simulations of Si PnCs

Material	Density (kg/m^3)	C_{11} (GPa)	C_{12} (GPa)	C_{44} (GPa)
Silicon	2330	217.3	84.5	66.4
Air	10^{-4}	10^{-3}	-10^{-3}	10^{-3}

2.3. Lattice Dynamics Technique

For bulk silicon, we consider a discrete (e.g., an atomic-level) model for which we obtain the dispersion using LD [23]. We consider a primitive cell consisting of a two-atom basis (with each having three degrees of freedom) and generate the equations of motion by identifying the prescribed interactions of each atomic pair. An interatomic energy potential, which can be obtained empirically, is used to derive the force constant matrix Φ for atoms j and j'. The equations of motion are thus written as

$$m_j \ddot{u}_\alpha = -\sum_{j'\beta} \Phi_{\alpha\beta}(j;j') u_\beta(j;j'), \tag{24}$$

where u denotes displacement, m denotes atomic mass and α and β represent Cartesian directions. Upon assuming a travelling wave solution,

$$u(r,t) = Ae^{ik\cdot r - i\omega t}, \tag{25}$$

where A denotes complex displacement amplitude, the following eigenvalue problem is constructed (under the quasi-harmonic approximation):

$$\left[D(\kappa) - \omega^2(\kappa) I\right] A(\kappa) = 0 \tag{26}$$

In Eq. (26), D is the dynamical matrix of size of $3M$ x $3M$, where M represents the number of atoms considered in the primitive cell. Upon solving Eq. (26) we obtain $\omega(\kappa)$ and $A(\kappa)$, which are the phonon frequencies and polarization vectors, respectively. As in the continuum

mechanics method using plane wave expansion, the dispersion is calculated by finding the eigenvalues at consecutive *k*-points defining the boundary of the irreducible Brillouin zone which in this case corresponds to the primitive cell of bulk silicon.

The Tersoff potential [24, 25] is used to model the interatomic forces with second nearest neighbor interactions considered, allowing for a relaxed Si-Si atomic separation distance of a = 0.38nm. The available degrees-of-freedom for two atoms allow for six branches to be plotted across the Γ-to-X direction of the primitive cell IBZ with a *k*-space resolution n_κ set to be greater than 256. The baseline thermal conductivity of Si was calculated from these data using the above Callaway-Holland *k*-space formulation.

2.4. Thermal Conductivity Calculations

Both forms of the Callaway-Holland require knowledge of the modal velocities, which in the bulk case can be calculated from LD simulations, and the phonon scattering lifetimes, which are typically parameterized and fit numerically to experimental data. In the PnC case, the modal velocities cannot be easily calculated due to the complexity of the dispersion diagram, and are therefore approximated using various methods, as described next.

2.4.1. Density of States Method

Using the DOS formulation, the phononic DOS is calculated by first calculating the dispersion behavior, not for just the boundary of the IBZ, but for the entire *k*-space area enclosed in it. The frequency axis is then divided into bins, and the number of modes lying within each bin is summed, giving the DOS. Note that it is impossible to separate modes of different types (i.e. longitudinal, in-plane transverse, or out-of-plane transverse) in this calculation, making direct calculation of the appropriate velocity for a given mode very difficult and thus necessitating an approximation of the velocity to be made. The simplest approximation that can be made that still preserves a measure of accuracy is based on the Debye model [18], which essentially assumes that dispersion of the bulk material is linear, giving a single velocity for the transverse and longitudinal modes, respectively. As shown in Figure 9, this approximation gives significant errors in the velocity of the bulk material on the highly-dispersive frequencies ranges, and in the case of the transverse modes in the region where there is a mode gap.

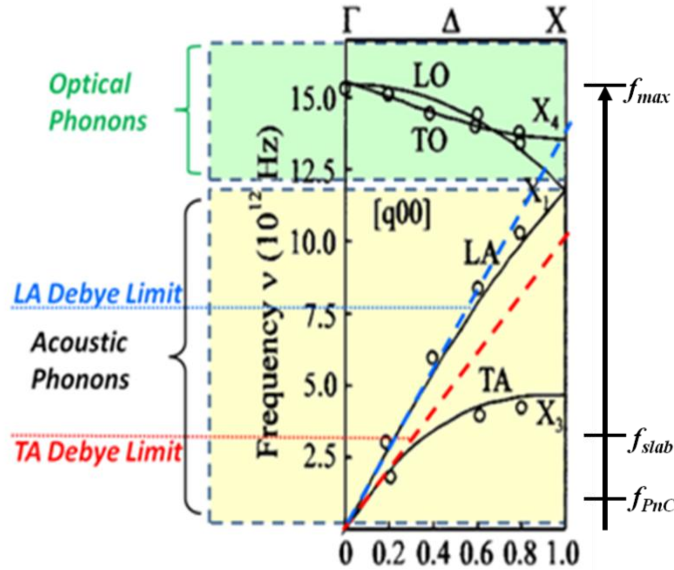

Figure 9. Phononic dispersion of bulk Si for Γ–X (black curves), along with the corresponding dispersion from the Debye approximation for transverse (red dashed curve) and longitudinal (blue dashed curve) modes.

Additionally, the PWE technique is also limited by the available computing resources as to how high in frequency the dispersion behavior can be calculated, since more RLVs are required to reach higher frequencies. Since the size of the problem is approximately dependent on the square of the number of RLVs, the computational load requirements quickly become larger than what can be handled by a supercomputer in a reasonable amount of time. For example, a PWE dispersion calculation for 20 *k*-points using 25^3 RLVs takes about 60 hours to complete on the Redsky supercomputer at Sandia Labs using 8 processors (8 cores each) and 96 GB of memory. This hefty calculation yields a maximum frequency of only 3 THz for a PnC having a lattice constant of 500 nm. Furthermore, the since the results of PWE are known to be inaccurate for at least the highest half of the frequencies calculated, these values must be thrown out, further limiting the maximum frequency that can be reached. Therefore, the Callaway-Holland calculation of thermal conductivity is carried up to the maximum phonon frequency in Si of about 15 THz by simply supplementing the PWE data with the known bulk dispersion behavior of Si for frequencies greater than what can be calculated accurately using PWE.

However, the errors introduced by these issues are mitigated by dividing the calculated thermal conductivity of a given PnC structure by the thermal conductivity of a slab of the same thickness but having no air holes ($r = 0$) calculated using the same assumptions. In this way, the errors due to approximation, which should be roughly the same in the two calculations, can be canceled out, resulting in a reasonable estimation of the thermal conductivity of the sample relative to an unpatterned slab. Given that the thermal conductivity of a slab can be calculated relative to a bulk material of known thermal conductivity, the reduction in thermal conductivity of a PnC relative to bulk (as well as the absolute value) can be extracted as well.

This method was used to calculate the thermal conductivity reduction of a set of PnC samples fabricated in Mesa facilities at Sandia Labs, composed of 500 nm thick Si with a square lattice of

air holes with lattice constants ranging from 500 to 800 nm and hole radii from 150 to 200 nm [26]. The results of the simulations are shown in Figure 10, along with a model of the thermal conductivity of an unpatterned slab and measured data from three other published results. For the thermal conductivity predictions, the velocities used in the Callaway-Holland model were a weighted combination of the Debye velocities for the Γ–X direction in Si, assuming that there are two transverse modes for each longitudinal one. The measured thermal conductivities of the porous structures are multiplied by a factor of $(1 + 2ff/3)/(1 - ff)$ (where *ff* is the filing fraction) to account for the porosity of the structures, and thereby directly compare the thermal conductivity of the solid matrix in the porous structures to the model of the unpatterned slab. Clearly, Figure 10 demonstrates that the calculated thermal conductivity ratios agree well with the experimental data measured using the TDTR technique described in Section 4.2.

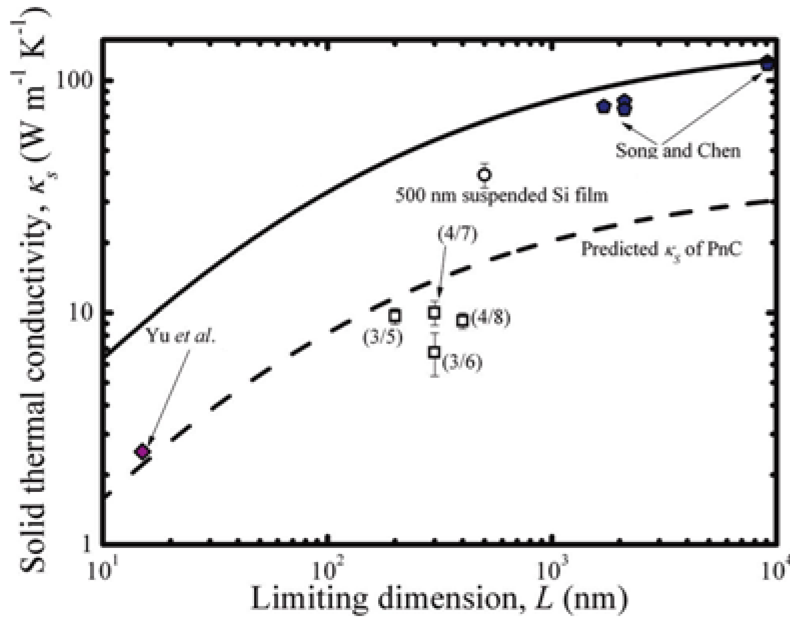

Figure 10. The thermal conductivity of Si structures at room temperature as a function of L for the PnCs (unfilled squares), microporous solids (filled pentagons), nanomesh (filled diamond), and a suspended 500 nm thick Si films that is, an unpatterned Si slab (unfilled circle). The references are from [26]. The solid line represents predictions of the unpatterned slab at room temperature as a function of *L*. The dashed line represents predictions of the PnC thermal conductivity using DOS data from PWE calculations.

2.4.2. DOS with Slab Padding

Since the PWE method only account for porosity and coherent scattering (not incoherent scattering), it is reasonable to expect that the dispersion behavior of a PnC slab should gradually approach that of an unpatterned slab as frequency increases due to the shorter wavelength phonons no longer "seeing" the periodic lattice of "large" inclusions but rather a bulk effective medium. This is confirmed by plotting the integrated DOS for both a given PnC and its corresponding slab. As seen in Figure 11, the difference between the two curves becomes negligible after a point, indicating that the behavior of the two structures from the thermal conductivity point of view is equivalent. Moreover, since the PWE simulations are performed using normalized parameters (i.e. frequency scales inversely with lattice constant) and an

unpatterned slab has no in-plane variation with lattice constant, the data from the slab simulations can be rescaled to reach higher frequencies. In other words, assuming that the slab thickness does not change, a slab having a normalized thickness $t/a = 1$ has similar dispersive behavior to a slab of thickness $t/a = 10$, but with a lattice constant that is 10 times smaller (resulting in frequencies that are 10 times higher). Thus, the PnC DOS data can be "padded" with slab data for frequencies greater than this point, eliminating some of the error in approximating the structure as bulk for frequencies greater than what can be reached with PWE.

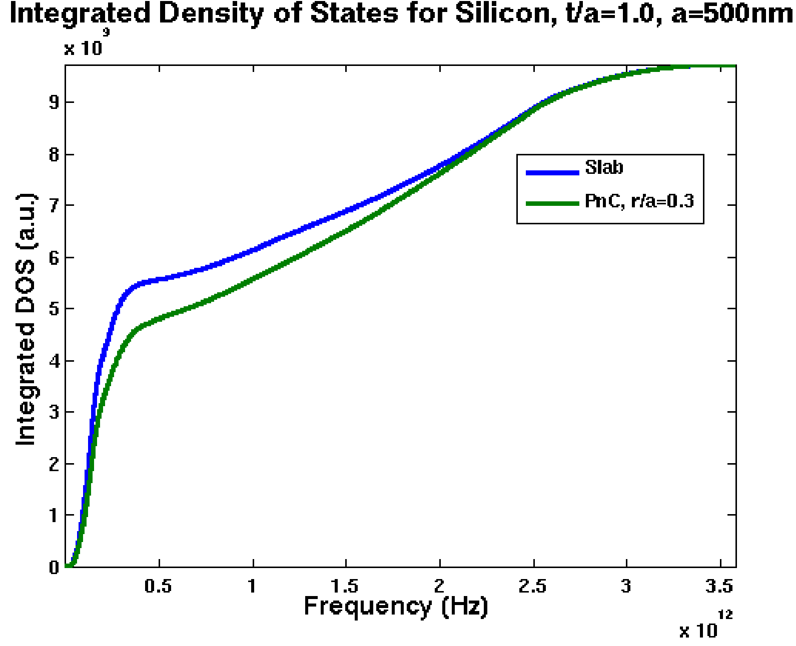

Figure 11. Integrated DOS for a Si slab of 500 nm thickness and a PnC of the same thickness and with 150 nm radius air holes.

2.4.3. Dispersion Method with Mode Velocities

In an effort to further improve the accuracy of the PWE calculations, particularly at higher frequencies, a scheme was developed to account for the dispersive behavior of bulk Si in the Callaway-Holland model. The theory behind this scheme is that the dispersion of Si can be approximately accounted for in PWE, which assumes that the material parameters are constant with respect to frequency (i.e. dispersionless), by calculating an effective mode velocity at each point in the dispersion diagram based on the actual modal velocities of the bulk material. The underlying assumption in this method is that the dispersive effects of the PnC act as a perturbation of the bulk dispersion in the vicinity of the corresponding frequency. Thus, the velocity of a given mode at a point in the dispersion can be approximated as a weighted average of the two modal velocities of the bulk material at that frequency, given by

$$v_{PWE}(\omega) = \sqrt{\frac{u_z^2 v_L^2(\omega) + \left(u_x^2 + u_y^2\right) v_T^2(\omega)}{u_x^2 + u_y^2 + u_z^2}} \tag{27}$$

where v_{PWE} is the velocity of a mode at frequency ω calculated using PWE; ux, uy, and uz are the x, y, and z components of the displacement, respectively; v_L is the longitudal mode velocity of the bulk material at frequency ω, and v_T is the transverse mode velocity of the bulk material at

frequency ω. The mode velocities of the bulk material are calculated from the dispersion from the LD technique. Using this approach, the linear dispersion approximation from the Debye model is removed, and even though transverse modes at frequencies in the mode gap will incorrectly appear in the PWE calculations, they will be assigned zero velocity, thus eliminating them from consideration in the Callaway-Holland calculation.

2.4.4. Multi-Scale Method

A final improvement to the inherent approximations in the PWE technique involves combining the dispersion calculated from PWE for a PnC with the PWE dispersion for a slab of the same thickness and LD dispersion for the bulk material in a strategic manner to capture the effects of the PnC on thermal conductivity as accurately and efficiently as possible. Using this multiscale approach, dispersion from PWE is used at lower frequencies, where the PnC has the greatest effect on phonon propagation, and is padded with the dispersion from LD for the bulk material at higher frequencies, where PWE calculation become inaccurate or intractable. Since the PnC will still be padded with data for the slab of corresponding thickness, as described above in Section 5.2.2, there are now two adjustable parameters in the frequency domain: the upper frequency for which the PWE dispersion is accurate and is distinguishable from the slab DOS, and the upper frequency for which the Debye approximation is still accurate and thus the re-scaled PWE dispersion for the unpatterned slab can still be used. The former frequency, f_{PnC}, is approximately 1 THz, and the latter frequency, f_{slab}, is approximately 2.5 THz (lower of the Debye limits for the transverse and longitudinal modes), as shown schematically in Figure 9. The parameters must be "tuned" to best fit experimental data, and generally vary slightly depending on the dimensions of the PnC under consideration.

3. FABRICATION OF PHONONIC CRYSTAL DEVICES

To validate our theoretical predictions above, we needed to fabricate phononic crystal samples with a high degree of fidelity and yield. Below is a description of the two methods that were used as venues for achieving the desired structural values.

3.1. MESA Silicon-Fab

The Microsystems & Engineering Sciences Applications (MESA) Complex at Sandia National Laboratories represents the essential facilities and equipment to design, develop, manufacture, integrate, and qualify microsystems for the nation's national security needs that cannot or should not be made in industry—either because the low volumes required for these applications are not profitable for the private sector or because of stringent security requirements for high-consequence systems such as nuclear warheads. Microsystems extend the information processing of silicon integrated circuits to add functions such as sensing, actuation, and communication—all integrated within a single package. The MESA Complex integrates the numerous scientific, engineering, and computational disciplines necessary to produce functional, robust, integrated microsystems at the center of Sandia's investment in microsystems research, development, and prototyping activities.

The designed test structures, shown in Figure 12, were fabricated in Sandia MESA facility. Figure 13 shows the schematics of the thermal conductivity test structure fabrication process. The fabrication starts with 6-inch silicon-on-insulator (SOI) wafers. The device layer is 500 nm-thick lightly p-type doped (boron, concentration $10^{16}/cm^3$) single crystal silicon. On top of the SOI wafers, 100 nm of undoped amorphous silicon was blanket deposited as an electrical isolation layer between the underlying device layer and the following metal contact layer (Figure 13a). High temperature annealing was used to relax the high stress in the amorphous silicon layer. Then, aluminum was deposited and patterned to form heaters, temperature sensors, interconnects, and bondpads (Figure 13b). Using plasma etching, phononic crystals and release trenches were defined in the silicon layers (Figure 13c). As the final step, the buried oxide (SiO_2) underneath the test structure was removed by a timed HF vapor etch to release the bridge (Figure 13d). Figure 14 shows scanning electron microscope (SEM) images of a fabricated thermal conductivity test structure.

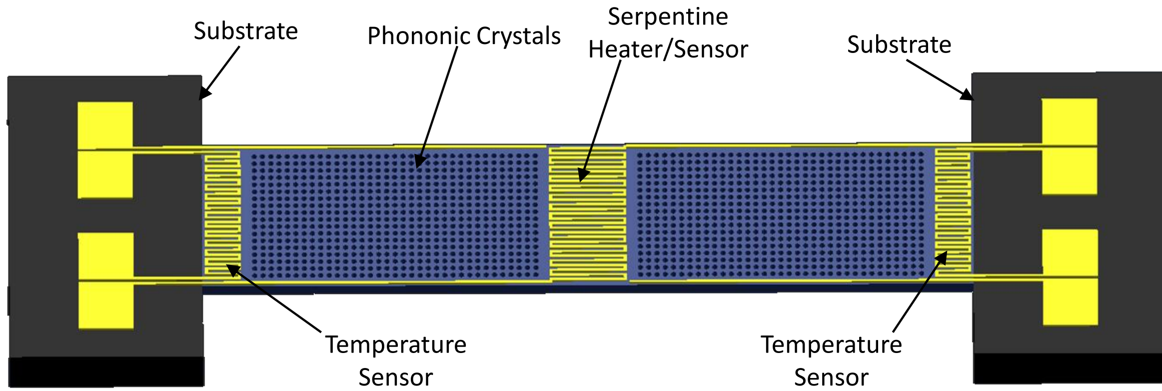

Figure 12. A schematic of the thermal conductivity test structure design. A phononic crystal bridge is suspended from the substrate. Serpentine aluminum traces are installed at both the bridge center and both bridge ends. While heat is supplied at the center, the temperature gradient across the bridge is measured to extract device thermal characteristics.

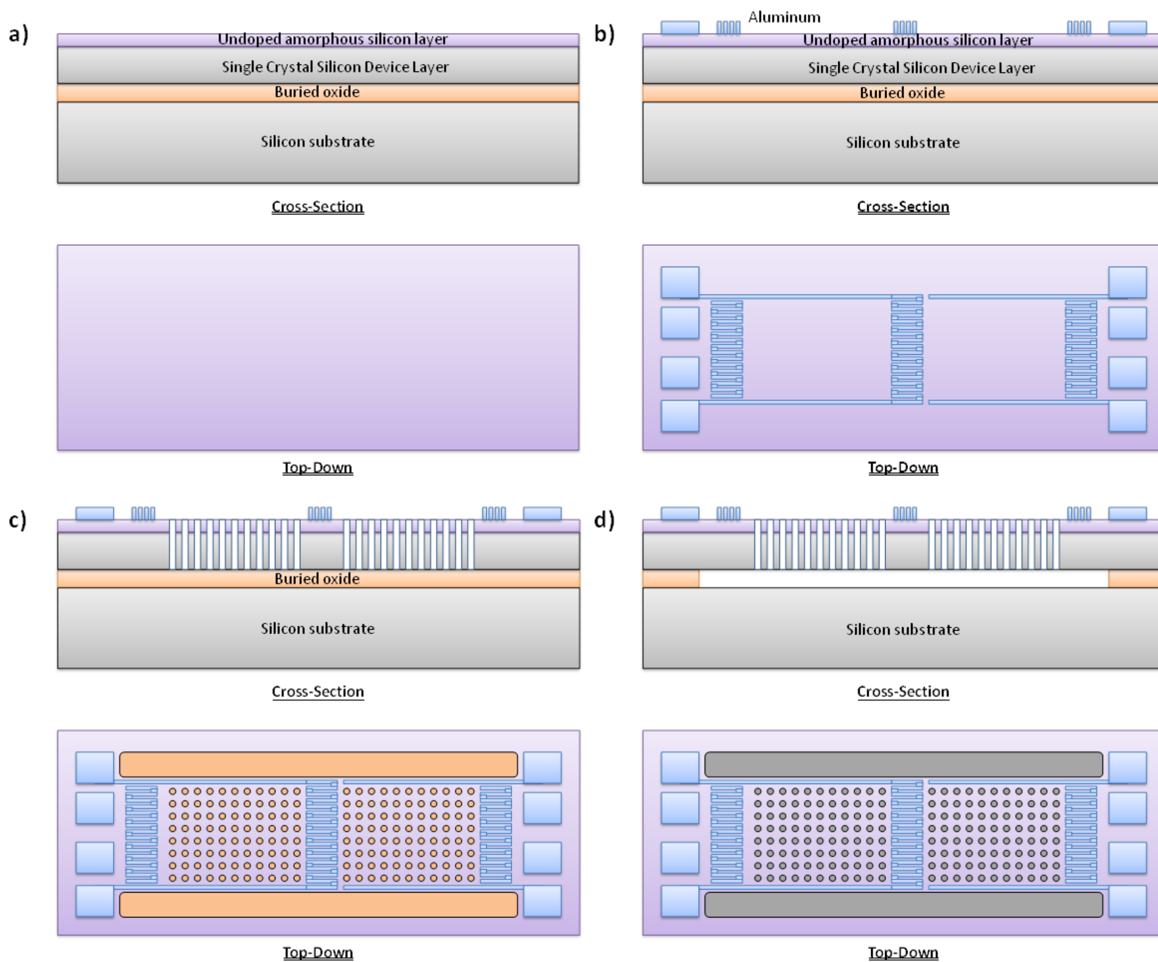

Figure 13. Schematics of the fabrication process for the thermal conductivity measurement structures.

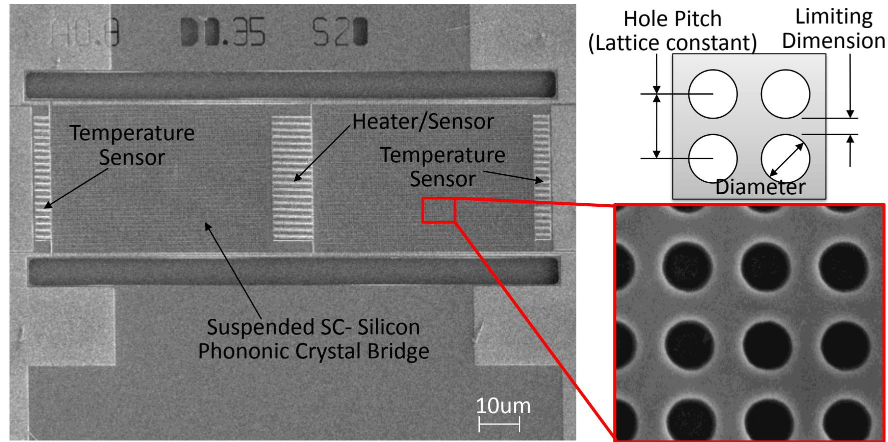

Figure 14. SEM images of fabricated simple cubic (SC) phononic crystal thermal conductivity test devices.

3.2. Focused Ion Beam

This section describes how PnCs were fabricated with a tool called a focused ion beam, or FIB. All of the FIB milling and nanoFIBrication in this work was performed on a dual-beam Quanta 3D FEG made by the FEI Corporation. The dual-beam refers to the system having both a FIB and an SEM.

A FIB is a system that generates a focused stream of charged particles (ions). Ions are extracted from a material, accelerated, and then focused into a narrow beam with a Gaussian density distribution using various apertures and electro-magnetic fields in an octopole arrangement. Figure 15 shows a schematic of the basic components in a FIB.

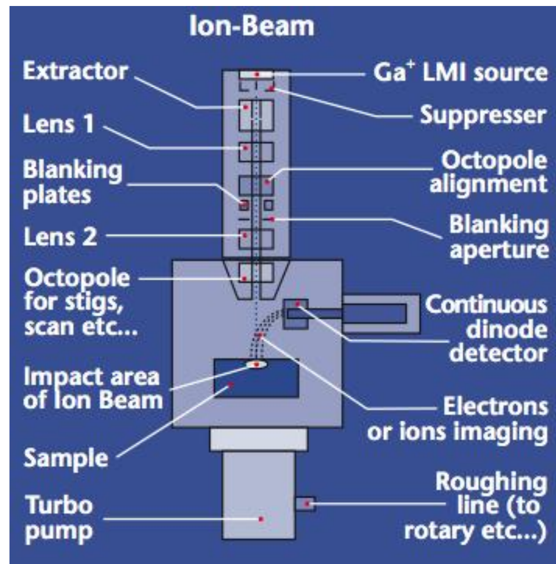

Figure 15. Schematic of a focused ion beam (FIB) system. Ions are extracted and then focused by multiple apertures and electromagnetic fields onto a sample. All of the FIB components and sample are under vacuum to prevent degradation. (Image courtesy of FEI)

A common source for generating ions is called a liquid metal ion source (LMIS) [27]. Figure 16 shows a drawing of a LMIS. Liquid metal from a reservoir is allowed to flow onto the tip of a sharp needle. The most common metal used is gallium due to its low melting point, low vapor pressure, and low reactivity with other elements, along with the fact that it produces mainly singly charged ions and it has enough mass to dislodge material at an acceptable rate [28]. As the liquid metal rests at the tip of the needle, an extractor lens with a large accelerating voltage pulls positively charged ions from the liquid. Typical accelerating voltages are between 5 and 30 kV.

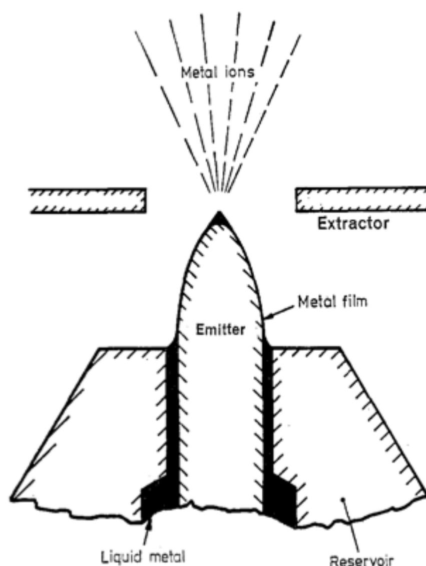

Figure 16. Drawing of a liquid metal ion source. Liquid metal wets a sharp tip and an extractor lens extracts ions from the metal by using a high accelerating voltage in the kV range.

Once the focused beam of ions leave the ion column, they interact with the sample surface. When a single Ga^+ ion strikes the sample surface, it can have enough energy and momentum to cause other atoms at the sample surface be removed, or sputtered away. The mean number of atoms removed for a single ion striking the sample surface is known as the sputter rate of the material, which is a dependent on the type of ion bombarding the surface, the accelerating voltage of the ion, and the angle of incidence. Increasing the accelerating voltage increases the sputter rate. As the angle of incidence changes from 0 to approximately 80° (with respect to normal), the sputter rate increases then quickly drops from 80° to 90°. A plot of sputter rate versus angle for various materials is shown in Figure 17. The ion species is Ga^+ at 30 kV. Sputter rates were calculated using a Monte Carlo simulation package named TRIM (Transport of Ions in Matter). TRIM calculates the stopping and range of ions into matter using a quantum mechanical treatment of ion-atom collisions [29]. The solid lines in Figure 17 are interpolated values.

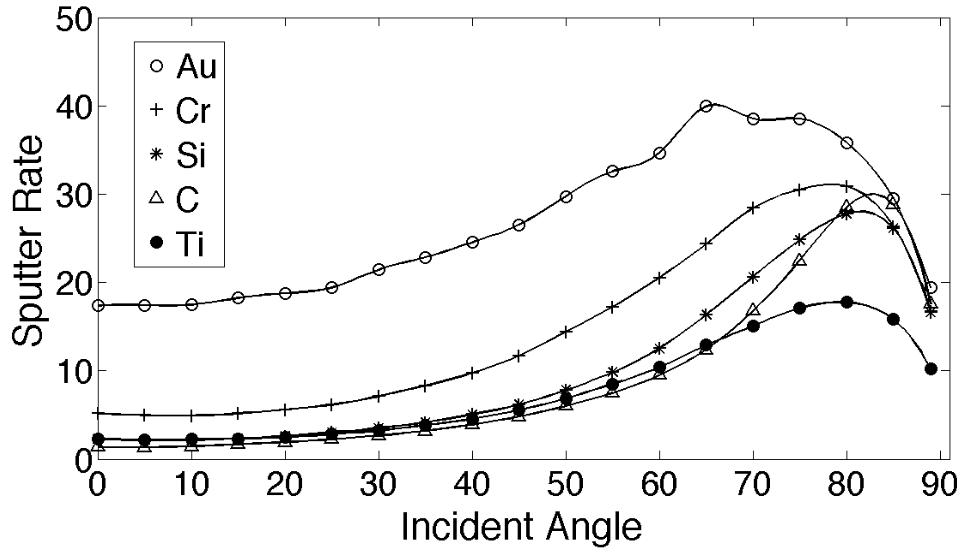

Figure 17. Sputter rates for various materials as a function of angle. Incident ion is Ga^+ at 30kV. Sputter rates were calculated using a Monte Carlo simulation package named TRIM. Solid black lines are interpolated values.

Prior to milling PnCs with the FIB, it was necessary to micro-fabricate freestanding Si membranes that serve as the matrix material of the phononic crystal. Two different paths were used. In the first path, the Si matrices were freely suspended prior to nanoFIBrication, and in the other path, suspension of the PnC was performed after milling with the FIB. Both paths use a top-down approach, starting with a bulk material and selectively removing the unnecessary material.

For the first path, the first step in fabricating PnCs was creating a thin device layer on a silicon-on-insulator (SOI) wafer. Studies show that thin membranes produce a band gap that is unaltered by slab modes [11]. More specifically, the membrane must be thinner than the lattice spacing. For example, a 33 GHz PnC requires a device layer less than or equal to 100 nm. To thin the initial 450 nm thick device layer of the SOI wafer down to a thickness of 100 nm or less, thermal oxide layers were grown from the Si and subsequently etched away until the desired thickness was attained. Initial variation of the device layer (±25 nm) caused similar variation in the final membrane thickness. After thinning, outlines of the PnC were patterned on the wafer. The process for creating the PnC outlines is show in Figure 18a.

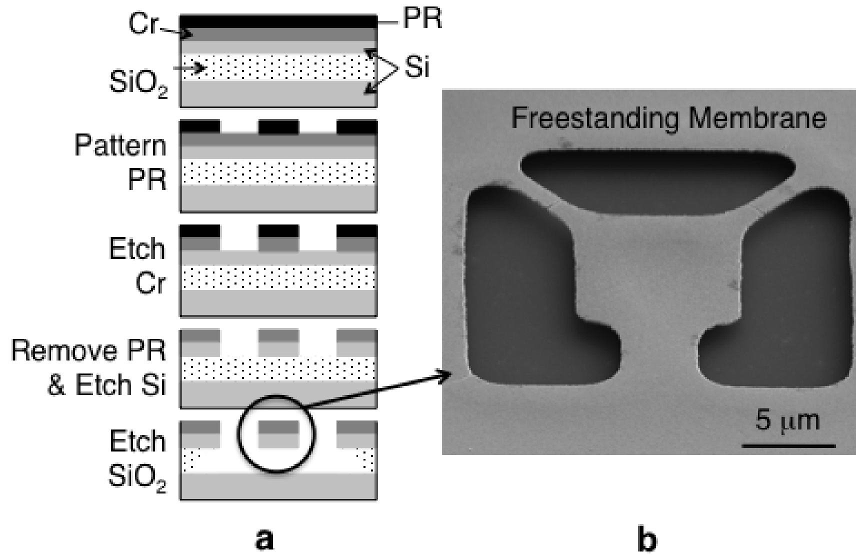

Figure 18. Fabrication process for creating a thin-freestanding membrane for PnCs. a) Cross sectional view of fabrication process. b) Released freestanding membrane.

The second method for fabricating Si matrices is similar to the first method, but the release step is performed after milling with the FIB. The process flow is shown in Figure 19.

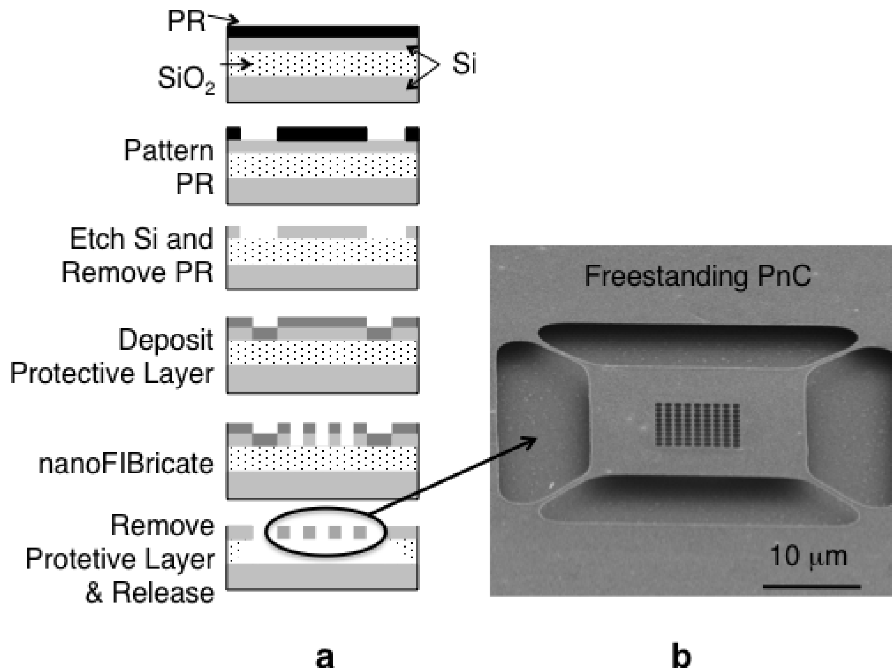

Figure 19. Second fabrication method for creating a thin-freestanding PnC. a) Cross sectional view of fabrication process. b) Released freestanding PnC.

In both methods, a protective layer is placed on top of the Si. The protective layer minimizes Ga^+ doping in the Si layer, which can affect both the electrical [30] and thermal properties [31] of Si. Since the goal of this effort is to determine how a PnC affects the thermal conductivity of

Si, it is important to minimize any additional variables that could affect the thermal properties of Si.

The choice of the proper protective layer is dependent on a number of factors. It must be relatively easy to add and remove. The protective layer needs to be compatible with the fabrication process. It must also be relatively thin. If it is too thick, then the ion beam will have a difficult time penetrating both the protective layer and the Si. Another consideration is electrical conductivity. If it is not conductive, then the incoming charged ions will be affected. As charge builds up on the sample surface, the ion beam will become distorted and will no longer mill the desired area. Last, it should have a sputter rate that is less than that of Si.

The best types of materials to be used as a protective layer are metals. Metals make a good protective layer for multiple reasons. They are easy to deposit, it is easy to find an etchant with a high selectivity between a given metal and Si, they are highly conductive which improves imaging in the SEM, and only a thin layer is required to block Ga^+ ions from penetrating into Si. For example, TRIM calculations of Ni show that 30 kV Ga^+ ions have a mean penetration depth of 9.7 nm into a 100 nm thick layer of Ni, and only a small percentage reach beyond 30 nm (Figure **20**). Unfortunately, Ni reacts with the fluorine in a hydrofluoric acid vapor and leaves a thin, greenish layer of NiF_2 on the PnC. Ti has a mean penetration depth of 17.9 nm, which is greater than Ni, but Ti has the advantage of being etched by hydrofluoric acid. Since hydrofluoric acid is required for removing the BOX layer and thus releasing the PnC, Ti makes a good choice for a protective layer. To ensure no Ga^+ reaches the Si, a 50 nm thick layer of Ti is used as the protective layer for fabricating PnCs with the FIB.

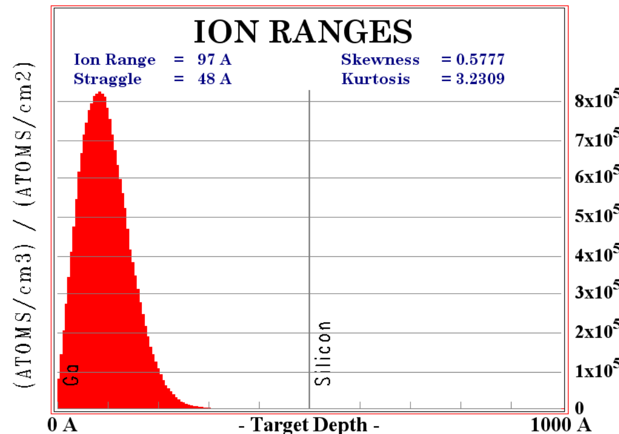

Figure 20. 30kV Ga+ ion penetration into 50 nm thick layer of Ni on top of 50 nm layer of Si. No ions reach the Si layer.

4. CHARACTERIZATION OF THERMOELECTRIC FIGURE-OF-MERIT

Three measurement techniques were implemented under this project to characterize the thermoelectric properties of our phononic crystal samples. Two of these, the four-point measurement and suspended island techniques, were used to probe the in-plane properties of the devices, and the third, time domain thermoreflectance, was used to probe the cross-plane thermal conductivity. The in-plane configuration of this method is mentioned as well, although it was not used in this work. Each of the setups is described in the following sections.

4.1. In-Plane Measurement Techniques

4.1.1. Equilibrium Thermoelectric Measurements

Figure 12 shows the design of the thermal conductivity test structure. Specifically, a 60um-wide and 200 um-long bridge-shaped structure containing periodic holes (PnC) was suspended above the substrate. At the bridge center, a 250nm-wide serpentine aluminum trace was installed that functioned as both heater and a temperature sensor. Two additional temperature sensors (serpentine traces) were placed symmetrically at both edges of the bridge. While heat is supplied at the center, the temperatures of bridge center and edges are measured to estimate device thermal resistance and thermal conductivity of the PnC membrane.

To measure the thermal conductivity of the samples, the temperature dependence of resistances of both the heater serpentine trace at the bridge center and temperature sensor traces at the bridge ends were first calibrated by a separate heated chuck measurement. Figure 21a shows the measured resistance changes with varying temperatures and Figure 21b shows their relative changes (base is 30˚ C). Both the heater trace and sensor traces exhibit almost identical relative resistance change due to temperature change with a temperature coefficient of resistance (TCR) of 0.0027 being extracted from the measured data.

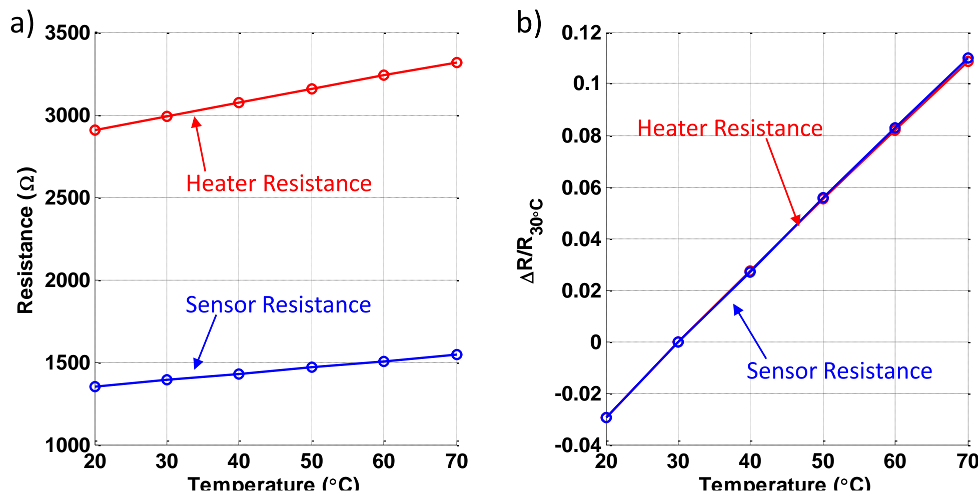

Figure 21. Trace resistance vs. temperature calibration data from a heated chuck measurement. a) Measured resistance values of heater trace and sensor trace with changing temperature. b) For both heater and sensor traces, their relative resistance changes were almost identical. The slope of this line is 0.0027.

Figure 22 shows the thermal resistance measurement setup diagram. Heat is supplied at the center of the test structure by applying power across the serpentine heater. By measuring the voltage across the heater and the current through it, both the supplied heat and resistance change can be simultaneously monitored. At the same time, the resistance change of the sensor traces at the bridge ends is also measured. Using the above TCR of 0.0027 (from Figure 21), the temperature changes of the heater and sensors are calculated. All measurements were conducted in vacuum (< 1 mTorr) while sweeping the heating power from 0 to 1 mW and back to 0 mW again. Figure 23 shows an example plot of the measured temperature vs. heating power. For each design set (hole pitch and diameter combination), 6 devices were tested.

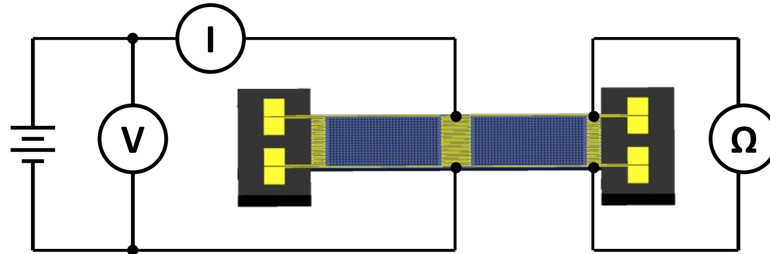

Figure 22. Test setup diagram for thermal conductivity measurement.

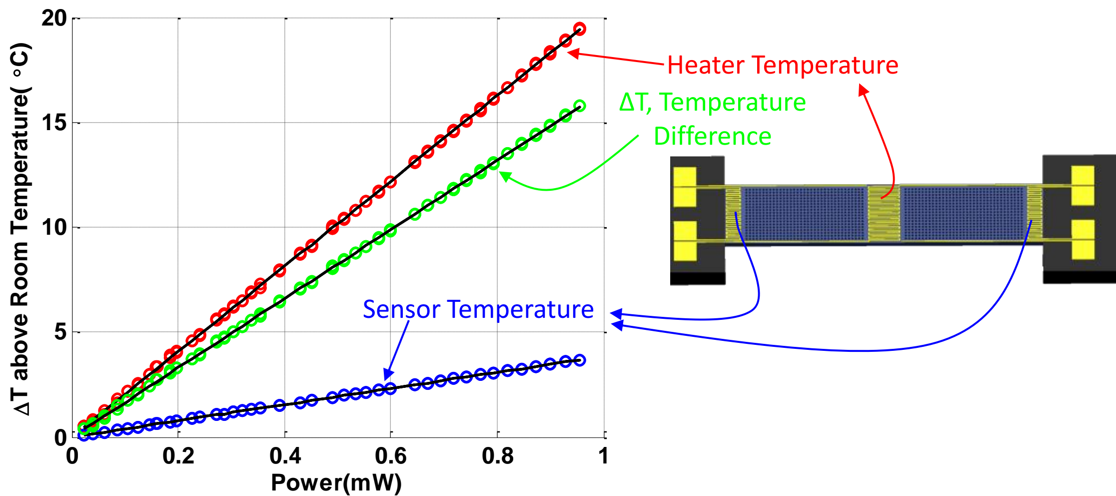

Figure 23. An example plot of measured temperature vs. heating power plot (Device ID-7). Temperature difference across the phononic crystal bridge was measured using calibrated serpentine traces while heating power supplied at the bridge center was sweeping between 0 to 1 mW.

From the measured temperature changes vs. heating power data, the thermal conductivities were extracted using ANSYS Finite Element simulation models and equivalent thermal circuit models, as shown in Figure 24. Since all measurements took place in vacuum, convectional heat leakage can be ignored. Also, radiative heat transfer was estimated to not exceed a maximum of 0.4% of the conductive heat transfer, and therefore was ignored as well in these models.

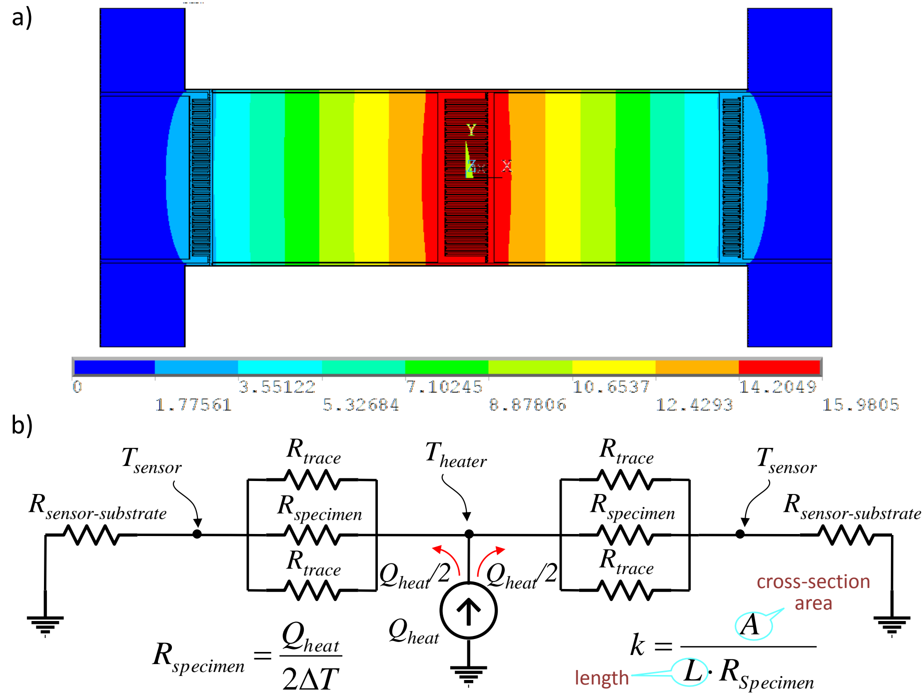

Figure 24. a) ANSYS FEM simulation model and b) equivalent thermal circuit model of thermal conductivity test structures.

The amount of other parasitic thermal resistance (mostly through the traces connecting the heaters and bondpads across the bridge) in these models of Figure 24 were verified by measuring the thermal characteristics of specially prepared samples, of which the phononic crystal regions were cut out using focused ion beam milling. After accounting for these parasitics, the thermal resistances only across the phononic crystal regions were extracted and by multiplying with the cross section areas and dividing with the length, the phononic crystal thermal conductivities were calculated. Figure 25 shows an example plot of extracted thermal conductivity versus temperature. As can be seen, at low heating power, the current measurement is too noisy and it was not easy to obtain reliable and repeatable data. Therefore, for reliability, we used thermal conductivity values when the average temperature across the bridge is 7˚ C above room temperature (300 K).

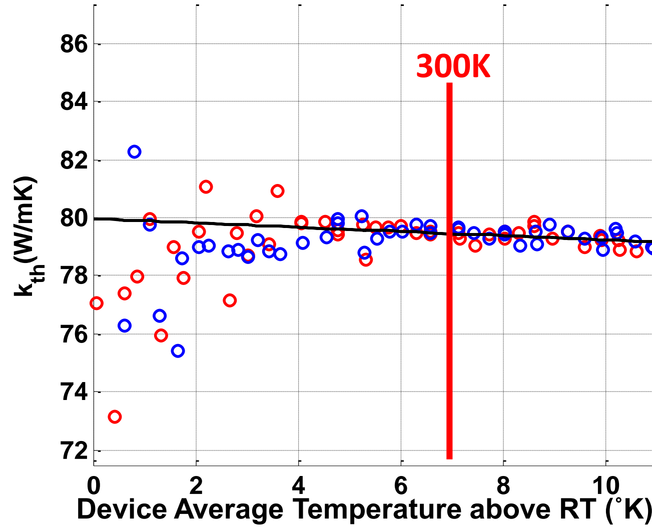

Figure 25. An example of extracted thermal conductivity values using the models shown in Figure 24. At low heating power, the data are scattered. In this study, thermal conductivities values at 300 K were used, which were more reliable and repeatable. Red circles indicate when the temperature was ramping up and blue circles when ramping down. This plot is the measured data of Device ID-7.

4.1.2. Suspended Island Technique

A micron-scale multi-use test platform based on accepted designs in the literature was designed and fabricated that can measure in-plane thermal conductivity, electrical conductivity, and Seebeck coefficient of micro- and nano-scale sized samples [32, 33]. For this report, the samples are phononic crystals (PnCs). Figure **26**a shows a SEM image of the test platform; it is tilted 52° to highlight the undercut of the fabrication process. The platform is comprised of two silicon nitride (SiN_x) islands connected to each other by a small strip of SiN_x. Figure **26**b shows a zoomed-in view of the small SiN_x strip between the islands and also of the Pt contact pads for mounting the PnCs. Prior to making measurements, the SiN_x bridge is cut to remove the potential for heat to flow across it instead of the PnC. On top of each island is a serpentine pattern of Pt acting as a resistance temperature detector (RTD). Each island has four connections; three are for performing three-point measurements on the RTDs and one is for measuring electrical resistance. The island on the left side of Figure **26**a is the heating island. Power is applied to the RTD on the heater and its resistance is simultaneously measured to determine the temperature of the heating island. It is important to freely suspend the heater island so that a majority of the heat generated by Joule heating on the island travels through the sample and to the sensing island. All four legs connected to the heater island are designed to have a considerably larger thermal resistance as compared to the sample connecting the islands, which also ensures that the majority of the heat passes through the PnC. On the right side of Figure **26**a is the sensing island. By measuring the resistances of the RTDs on both islands, one can determine the ΔT across the sample suspended between the two islands.

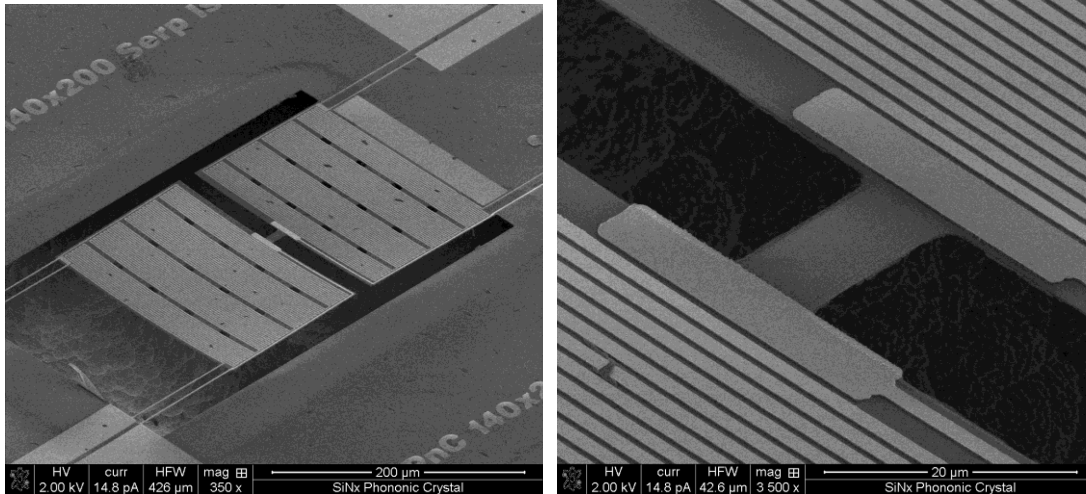

Figure 26. SEM images of multi-use test platform for measuring thermal conductivity of phononic crystals. Both images are tilted 52° with respect to normal. a. Overview of suspended islands. b. Zoom-in of the SiN_x bridge connecting the heater and sensing islands. Pt pads on either side of the bridge provide a location for the PnCs to be welded on to the islands.

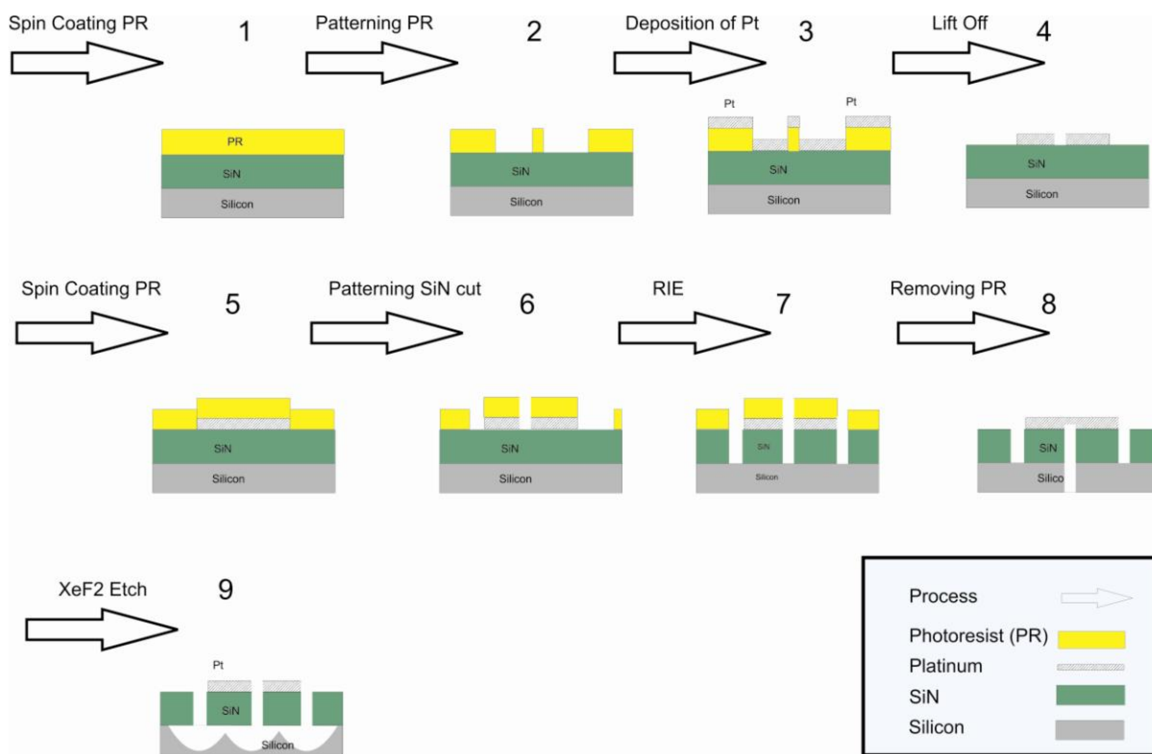

Figure 27. Process flow for fabrication of in-plane thermal conductivity test platform.

All of the platforms were fabricated using standard microfabrication techniques; see Figure 27. First a Si wafer with a 1 µm thick LPCVD SiN_x film is spin coated by 1.4 µm thick positive photoresist (PR). Consequently, 80 nm of platinum is deposited on the wafers by thermal evaporation. Afterwards, 2 µm thick positive PR is patterned on the wafers to protect the devices during (reactive ion etching). The SiN_x pattern is cut by RIE inside an atmosphere of

98% CF_4 and 2% O_2 plasma. Finally, the silicon underneath the devices is removed with a dry etch of XeF_2 at a pressure of 1 T.

Fabrication of the phononic crystals was undertaken using a focused ion beam technique developed as a result of this project. Two different phononic crystals comprised of air inclusions in a Si matrix were tested on the multi-use platform. Both used the same lattice spacing and r/a ratio. Each PnC had a lattice constant of 250 nm and a radius of 41 nm, which corresponds to an r/a ratio of 0.16 and critical length of 168 nm. The thickness of the Si was 250 nm (250 nm thick device layer on a SOI wafer), so the critical length is dominated by the spacing between inclusions. The difference between the PnCs is the lattice type; one used a simple cubic lattice and the other used a hexagonal lattice. Figure 28 shows SEM images of the PnCs. The measured radius for the simple cubic PnC was 41.5 nm ± 2 nm and the hexagonal PnC had a measured radius of 41 nm ± 2 nm.

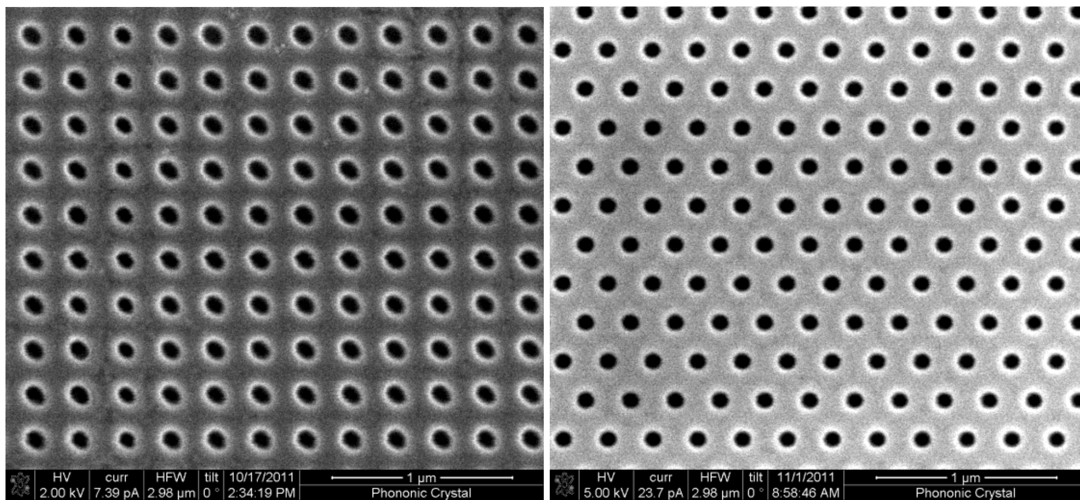

Figure 28. SEM images of PnCs measured with multi-use platform. a. Simple cubic PnC. b. Hexagonal PnC.

Both PnCs were fabricated with a focused ion beam, or FIB. The FIB for this work is FEI's Quanta 3D FEG dual beam system, which has both a FIB and SEM. The electron beam is mounted vertically, and the ion column is mounted 52° from vertical. The beam profile of the FIB has a Gaussian density distribution of Ga^+ ions, and it can be as small as 7 nm at full-width-half-maximum (FWHM). The accelerating voltage of the Ga^+ ions is 30 kV. For the devices fabricated in this work, a 50 nm protective layer of Ti was deposited on the device layer of the SOI wafer. By using a protective layer, surface damage by Ga^+ ions is confined to the Ti and does not reach the surface of the thin Si membrane between each via [34]. Protection of the Si surface also minimizes the possibility of Ga doping affecting the thermal conductivity. Once the vias are milled, the samples are dipped in 6:1 buffered oxide etch (BOE), which etches both Ti and the 2 μm thick BOX layer. Next, the samples are dried with a CO_2 critical dryer to prevent stiction failure. For more details about this process see Section 3.2 of this Report.

Since the PnC is not integrated into the test platform, it must be transferred on to the gap between the islands of the platform. The transfer process makes use of the dual beam FIB/SEM system that is also equipped with an Omniprobe™ and a Pt gas injection system. The

Omniprobe is equipped with a fine tipped W needle with high precision translation movements. A Pt gas injection system allows Pt to be deposited at user defined location and depth. First, a protective mask is milled which will be placed on top of the PnC during the transfer process. This is done to limit Ga doping of the PnC during the transfer to the test platform. Two tabs are left to suspend the protective layer so the Omniprobe can be attached. After cutting out the mask, it is welded to the tip of the Omniprobe with Pt and the tabs are then cut to fully release the mask. Next, the PnC is cut from its resting place. Again, two tabs are left to suspend the PnC so the mask can be placed on top. Once the protective layer is on top the PnC, it is welded to the PnC. Next, the tabs are cut and the PnC is transferred to the gap between the test platforms. With both ends of the PnC touching the Pt pads on the heater and sensing island, a thin strip of Pt is used to connect the PnC to the Pt pads. Last, the protective layer attached to the Omniprobe is removed. A picture of mounted PnC on a platform is shown in Figure 29.

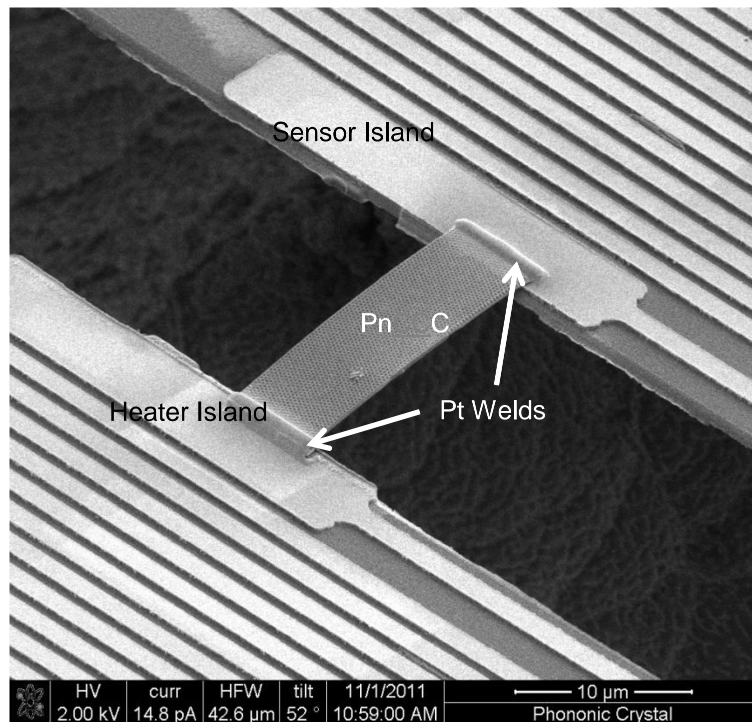

Figure 29. PnC mounted onto a thermal conductivity platform.

A thermal circuit of the test platform is shown in Figure 30. Heat generated by the heating island is labeled Q_H. Q_L refers to the heat that passes through a single suspended leg connected to the heating island, and Q_S is the heat that passes through the PnC and sensing island. T_H is the temperature of the heating island, T_S is the temperature of the sensing island, and T_A is the ambient temperature.

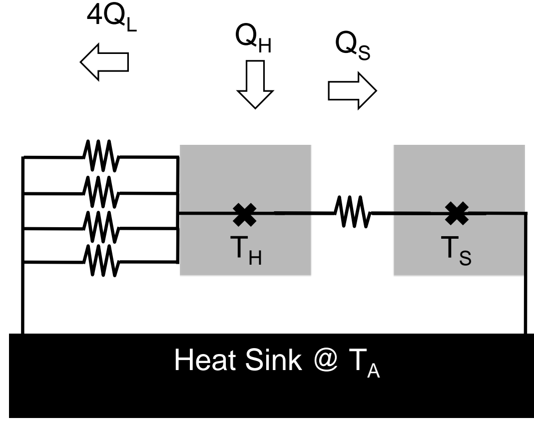

Figure 30. Electrical and Thermal Circuit of test platform.

The starting point for determining the thermal conductivity is straightforward; heat in equal heat out:

$$Q_H = Q_S + 4Q_L. \tag{28}$$

Heat loss through each leg is given by

$$Q_L = \frac{T_H - T_A}{R_L^{Th}} = \frac{\Delta T}{R_L^{Th}}, \tag{29}$$

where R_L^{Th} is the thermal resistance of a single suspended leg. Heat loss across the PnC is given by

$$Q_S = \frac{T_H - T_S}{R_{PnC}^{Th}} \approx \frac{T_H - T_A}{R_{PnC}^{Th}} = \kappa_{PnC} \frac{A_{PnC}}{L_{PnC}} \Delta T, \tag{30}$$

where R_{PnC}^{Th} is the thermal resistance of the PnC. Because the sensing island does not have free standing legs, the boundary condition of the constant ambient temperature is right beside the island instead and so the temperature of the sensing island is assume to be almost equal to ambient. Combining Equations 28 through 30 gives

$$Q_H = \frac{4\Delta T}{R_L^{Th}} + \kappa_{PnC} \frac{A_{PnC}}{L_{PnC}} \Delta T. \tag{31}$$

The relationship between resistance and temperature is given by

$$R = R_o + R_o \alpha \Delta T, \tag{32}$$

where R is the electrical resistance of the RTD at a given temperature, R_o is the electrical resistance of the RTD at the initial temperature, and α is the temperature coefficient of resistance. Substituting Eq. (32) into Eq. (31) gives

$$Q_H = \left[\kappa_{PnC} \frac{A_{PnC}}{L_{PnC}} + \frac{4}{R_L^{Th}} \right] \frac{R - R_o}{R_o \alpha}, \tag{33}$$

where κ_{PnC} is the thermal conductivity of the phononic crystal, and A_{PnC} and L_{PnC} are the cross-sectional area and length of the PnC respectively. By rearranging the terms in Eq. (33), a point-slope equation is reached

$$Q_H = \left[\kappa_{PnC} \frac{A_{PnC}}{L_{PnC}} + \frac{4}{R_L^{Th}} \right] \left[\frac{R}{R_o \alpha} \right] - \left[\kappa_{PnC} \frac{A_{PnC}}{L_{PnC}} + \frac{4}{R_L^{Th}} \right] \left[\frac{1}{\alpha} \right], \tag{34}$$

with R as the independent variable and a slope, m, given by

$$m = \left[\kappa_{PnC} \frac{A_{PnC}}{L_{PnC}} + \frac{4}{R_L^{Th}} \right] \frac{1}{R_o \alpha}. \tag{35}$$

If the thermal resistance of a single suspended leg is large compared to the thermal resistance of the PnC, then the second term in the bracket of Eq. (35) can be neglected. For a 100 µm long suspended leg, the thermal resistance is estimated to be 12 MK/W. If the PnC has a thermal conductivity near 10 W/m-K, a thickness of 250 nm, width of 6 µm, and length of 17 µm, then its thermal resistance is less than one-tenth of the leg. Neglecting the second term, the thermal conductivity of the PnC is given by

$$\kappa_{PnC} = \frac{m L_{PnC} R_o \alpha}{A_{PnC}}. \tag{36}$$

All of the PnC dimensions are measured with the SEM. The α-term is determined by calibrating the platform. R_o is measured during testing, and the slope m, is derived from the plot of input heat versus heater resistance. From these values and measurements, the thermal conductivity of the PnC can be calculated.

4.2. Cross-Plane Thermal Conductivity Measurement

4.1.2. Time Domain Thermoreflectance Technique

Pump-probe transient thermoreflectance techniques utilizing short pulsed lasers have been extensively used to measure thermal conductivity, κ, and thermal boundary conductance, h_K, of nanomaterials and interfaces of nanomaterials, such as κ in metal films [35], dielectric films [36], phase change materials [37], thermally anisotropic materials [38], superlattice structures [39], and layered nanolaminates [40, 41] and h_K across metal-metal [42] metal-dielectric [43-47] and metal-liquid [48] interfaces. These transient thermoreflectance techniques measure the change in reflectance of the surface of a material as a function of time after a short pulsed heating event. The change in reflectance is related to the temperature change of the electrons in the material, and the measured change in temperature as a function of time is then related to κ and h_K through a conduction heat equation. This experiment is referred to as time domain thermoreflectance (TDTR).

4.2.1. Cross-Plane TDTR

The experiments and analyses in this LDRD are focused on pulsed laser heating from a Ti:sapphire oscillator with a fundamental output of 90 fs pulses at 80 MHz (12.5 ns between laser pulses); the laser pulses are then further modulated at with an electro-optic modulator to create a modulated heating event at the sample surface, and the temperature decay on the surface of the samples from this modulated heating events are monitored over ~4 - 8 ns. The laser pulses are treated as delta functions in time due to the ultrashort pulse width compared to the time delay of the experiments. The thermal penetration depth of the modulated heat source is estimated by $\sqrt{D/(\pi f)}$, where D is the diffusivity and f is the modulation frequency. For most solids subjected to MHz thermal modulation rates, the thermal penetration depth is anywhere from 100 nm – 10 µm. To ensure mostly cross plane (one dimensional) transport, the laser spot size of the

modulated heating source should be greater than the thermal penetration depth. Typical TDTR experiments utilize pump spot sizes on the order of 10 μm. Therefore, for low diffusivity systems, the thermal transport measured in TDTR experiments is nearly entirely cross-plane due to the small thermal penetration depth.

In typical TDTR experiments, the pump and probe beams have spatially Gaussian intensity distributions when incident on the film surface. Therefore, depending on the relative sizes and overlap of the beams, the radial distributions of the pump beam could affect the temperature measured by the probe beam. In this case, the assumption a one dimensional heat transfer model may not be applicable since it assumes that the probe reflectance, or the measured change in temperature, is measuring a uniformly heated plane at the surface of the film. To correct for this, Cahill [49] derived an expression for $\theta(r)$, the temperature rise at the surface of the film, assuming radial spreading in a half-sphere from the pump pulse. This begins by considering the axially symmetric heat equation in cylindrical coordinates is given by

$$C_1 \frac{\partial \theta_1(r,z,t)}{\partial t} = \kappa_{1,z} \frac{\partial^2 \theta_1(r,z,t)}{\partial z^2} + \frac{\kappa_{1,r}}{r} \frac{\partial}{\partial r}\left(r \frac{\partial \theta_1(r,z,t)}{\partial r} \right), \tag{37}$$

where r is the radial coordinate, the subscript r and z denote the radial and cross plane conductivities, and C is the volumetric heat capacity. Taking the Hankel transform along the radial, planar dimension, then applying a Fourier transform, Eq. (37) leads to

$$\frac{\partial^2 \theta_1(r,z,\omega)}{\partial z^2} = q_{T,1}^2 \theta_1(r,z,\omega), \tag{38}$$

where ω is the angular frequency of the pump pulses and

$$q_T^2 = \frac{\kappa_r K^2 + iC\omega}{\kappa_z}, \tag{39}$$

where K is the transform variable. This anisotropic q was used by Schmidt *et al.* [38] to determine the directionally dependent thermal conductivities of graphite in anisotropic structures. In this work, however, we consider isotropic materials and we are only interested in cross plane properties, so $q_T^2 = K^2 + (iC\omega/\kappa)$.

The temperature change on the surface of the film due to heat flow through underlying materials is easily taken into account through Carslaw and Jaeger's solution for steady periodic temperature change in composite slabs [50]. A convenient implementation of this is presented by Feldman [51] and discussed here. The change in surface temperature of material 1 is given by

$$F(k) = \frac{1}{\gamma_1}\left(\frac{F_{T1}^+ + F_{T1}^-}{F_{T1}^- - F_{T1}^+} \right), \tag{40}$$

where F_{T1}^+ and F_{T1}^- are temperature change coefficients related to the forward and backward propagating waves on the surface (top side) of material 1 and where $\gamma = \kappa q_T$. The forward and backward propagating wave at the top side of material 1 are related to the waves on the bottom side through

$$\begin{bmatrix} F_{T1}^+ \\ F_{T1}^- \end{bmatrix} = \begin{bmatrix} \exp[-q_1 d_1] & 0 \\ 0 & \exp[q_1 d_1] \end{bmatrix} \begin{bmatrix} F_{B1}^+ \\ F_{B1}^- \end{bmatrix}, \tag{41}$$

where d is the material thickness. For material 1, the top side is assumed at the slab/air interface and the bottom side is assumed as the interface between material 1 and material 2 (i.e., film/substrate). Given a thermal boundary conductance, h_K, between material 1 and material 2, the temperature at the top of slab 2 is related to the temperature at the bottom side of slab 1 by

$$\begin{bmatrix} F_{B1}^{+} \\ F_{B1}^{-} \end{bmatrix} = \frac{1}{2} \begin{bmatrix} 1 + \dfrac{\gamma_2}{\gamma_1} - \dfrac{\gamma_2}{h_{K,12}} & 1 - \dfrac{\gamma_2}{\gamma_1} + \dfrac{\gamma_2}{h_{K,12}} \\ 1 - \dfrac{\gamma_2}{\gamma_1} - \dfrac{\gamma_2}{h_{K,12}} & 1 + \dfrac{\gamma_2}{\gamma_1} + \dfrac{\gamma_2}{h_{K,12}} \end{bmatrix} \begin{bmatrix} F_{T2}^{+} \\ F_{T2}^{-} \end{bmatrix}. \tag{42}$$

Assuming a bulk substrate, heat cannot reach the bottom side of slab 2 at rates comparable to the modulation frequency (semi-infinite), so there is no thermal buildup of waves and

$$\begin{bmatrix} F_{T2}^{+} \\ F_{T2}^{-} \end{bmatrix} = \begin{bmatrix} 0 \\ \exp[-q_2 d_2] \end{bmatrix}. \tag{43}$$

with Eqs. (40) – (42), this approach gives a straight forward method to solve for heat conduction through several materials and interfaces via successive implementation of Eqs. (41) and (42) for each layer and then Eq. (43) for the final, semi-infinite layer. This is much less computationally expensive than solving the heat equation in the time domain for each interface and material.

To determine the temperature oscillations on the surface of material 1 with the frequency domain model in Eq. (38) due to cooling from underlying layers described by Eqs. (41) – (43), a top surface boundary condition must be imposed. In TDTR, this is described by first convoluting Eq. (40) with the pump-beam distribution [38], given by

$$\theta(k) = F(k) \frac{A}{2\pi} \exp\left[\frac{-k^2 w_{PU}^2}{8} \right], \tag{44}$$

where w_{PU} is the $1/e^2$ radius of the pump beam, and then taking the weighted average of the surface temperature oscillations by the probe beam of $1/e^2$ radius w_{PR} to yield [49]

$$\theta(r,0,\omega) = \frac{A}{2\pi} \int_0^\infty F(k) \exp\left[\frac{-k^2 \left(w_{PU}^2 + w_{PR}^2 \right)}{8} \right] k\,dk \,. \tag{45}$$

Equation (45) gives the change in temperature as a function of heating event modulation frequency at the surface of the film. This axially symmetric thermal model has been used by several groups to determine h_K [46, 52] and, due to its simple extension to multilayer structures, thermal conductivity of thin layers and multilayered structures [36, 40, 41, 53-55]. Note, that in this development, the pump source is assumed to be applied only at the surface, so substrate effects on the pump distribution are nonexistent. Although Eq. (45) accounts for radial effects in TDTR, it does not give the response as a function of time, which is measured in TDTR. To examine the temporal evolution of Eq. (45), the response of the material systems to the laser and modulation repetition rates must be considered. This is described in detail through lock-in response functions.

Due to the relatively small change in voltage due to the probe thermoreflectance response as compared to the DC voltage from the reflected probe, a lock-in amplifier is used in TDTR data collection to monitor the temporal decay in the thermoreflectance response occurring at the modulation frequency of the heating event. The output of the lock-in amplifier serves to relate frequency domain models to the time domain. The lock-in output will be the magnitude, R, and

phase, ϕ, of the probe signal at the heating event modulation frequency. Mathematically, the lock-in output takes the form of [38]

$$R\exp[i(\omega_0 t+\phi)] = Z(\omega_0)\exp[i\omega_0 t], \tag{46}$$

where ω_0 is the modulation frequency of the pump pulses and $Z(\omega_0)$ is the transfer function of the lock-in. In the frequency domain, the transfer function can be represented as [49]

$$Z(\omega_0) = \frac{(2\pi)^2\chi}{\omega_s^2}\sum_{M=-\infty}^{\infty}\theta(\omega_0 + M\omega_s)\exp[iM\omega_s\tau], \tag{47}$$

where θ is calculated with Eq. (45), ω_s is the modulation frequency of the laser system (not the modulation frequency of the heating event; so for a Ti:Al_2O_3 oscillator, $\omega_s/2\pi$ is approximately 80 MHz), τ is the delay time between the pump and probe pulses, χ is a constant that is related to the gain of the electronics, the power of the pump and probe pulses, and the thermoreflectance coefficient of the material. The thermoreflectance coefficient, which relates the change in temperature from the model to the change in reflectance measured in the experiment, is a material property that is related to the band structure, electronic transitions, and dielectric function [56]. In the low perturbation regime (i.e., small temperature rise of the film compared to ambient) in which this work is focused, the change in reflectance is linearly related to the change in temperature and the thermoreflectance coefficient is a constant. From Eq. (47), the lock-in outputs are given by

$$X = \mathrm{Re}[Z(\omega_0)], Y = \mathrm{Im}[Z(\omega_0)], \tag{48}$$

where X and Y are the real and imaginary components of the measured frequency response, and

$$R = \sqrt{X^2 + Y^2}, \phi = \tan^{-1}\left[\frac{Y}{X}\right]. \tag{49}$$

By nature of Eq. (47), pulse-to-pulse heating and thermal accumulation due to pump modulation is taken into account with a frequency domain model (note that, in this work, when calculating temporal response with the frequency domain models, it is implied that the frequency domain models are used in conjunction with Eq. (47) to determine the time domain response). Although a similar model can be derived for pulse accumulation in the time-domain [38], it has not been used in previous works, most likely due to the numerical cost which negates the benefit of using the simplified model in the time domain. Even with exact analytical forms of the conduction thermal diffusion equation obtained by Laplace transforms [57], accounting for pulse accumulation can be computationally expensive compared to that in the frequency domain since, in the time domain, the solution must take into account the multiple pulses in the pump modulation envelope occurring every 12.5 ns while providing picosecond resolution in the analysis.

The thermal model and lock-in transfer function discussed above are applied to data determining h_K and κ from pump-probe measurements using the TDTR experimental setup at Sandia National Labs. The experimental setup, shown in Figure 31, is nearly identical to similar setups that exploit coaxial pump-probe geometries discussed in previous works [38, 58, 59]. The laser pulses in this specific experimental setup emanate from a Spectra Physics Mai Tai oscillator outputting 350 mW of power at a repetition rate of 80 MHz and pulse widths of 90 fs at a wavelength of 785 nm. The setup shown in Figure 31 differs from previous collinear setups by two slight modifications. First, the pulses are first passed through a pair of collimating lenses to

minimize probe divergence at the sample surface due to the variable delay stage; upon characterization with a sweeping knife edge [60], the probe (and pump) radius at minimum pump-probe delay is ~ 15 μm and exhibits less than 1 μm divergence at maximum delay. Then, the pulse train passes through an adjustable half-waveplate before being split into the pump and probe paths by a polarizing beam splitter cube (PBS); this fixes the pump and probe path as orthogonally polarized and the waveplate therefore allows for easy adjustment of the pump and probe powers; the relative pump and probe powers are adjusted to achieve a maximum thermoreflectance signal. We vary the temperature of the sample of interest by mounting the sample in a cryostat with optical access that can operate from 77 – 500 K.

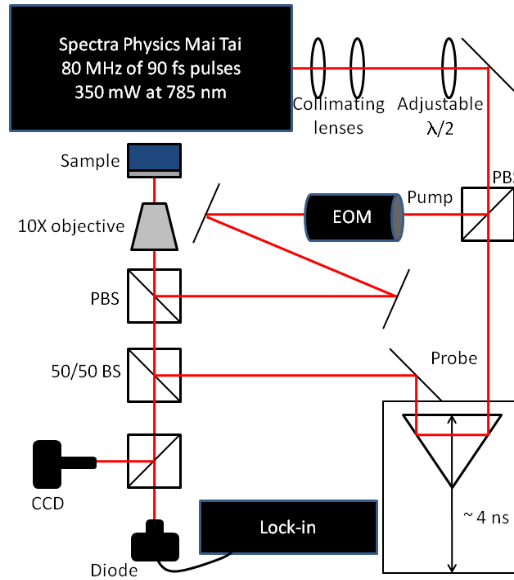

Figure 31. Schematic of TDTR experiment built at Sandia as part of this LDRD.

The data must be post processed to remove any electronic noise that would lead to unwanted signals. These signals would appear as a change in the imaginary component of the signal, Y, as τ crosses zero, since Y should not change as the pump-probe delay time goes from negative to positive. Schmidt *et al.* [38] determined the change in the real and imaginary components of the signals and calculated a phase noise to subtract from the data. Cahill [49] corrected for this by multiplying the signal by a small phase factor. Here, we employ the following correction: the change in the lock-in signals as the delay time crosses $\tau = 0$, ΔX and ΔY, are computed from the collected data. The measured signals are corrected by rotating the signal in the complex plane, so that the corrected values for X and Y are given by [61]

$$X_c = X\cos\left[\tan^{-1}\left[\frac{\Delta Y}{\Delta X}\right]\right] - Y\sin\left[\tan^{-1}\left[\frac{\Delta Y}{\Delta X}\right]\right], \tag{50}$$

and

$$Y_c = Y\cos\left[\tan^{-1}\left[\frac{\Delta Y}{\Delta X}\right]\right] + X\sin\left[\tan^{-1}\left[\frac{\Delta Y}{\Delta X}\right]\right]. \tag{51}$$

A similar method of data correction was employed by Costescu *et al.* [52] to correct the data for radial diffusion in the substrate. In practice, the phase of the lock-in is adjusted before each measurements so that Y is constant as the stage moves across $\tau = 0$ [49] so that Eqs. (50) and (51)

can be used simply as a check to ensure that the phase adjustment has removed the majority of the instrument noise. This also allows for the instrument noise to be quantified in terms of the lock-in phase so that this adjustment can be used in future measurements and analysis [62].

To evaluate the various thermophysical properties of interest, we must determine an appropriate range in which to fit the various models to the experimental data. For example, a given material system may be extremely sensitive to changes in h_K over a certain range but not κ. This aspect of the models is used to determine ranges in which to fit the various models to the data. Costescu *et al*. [52] defined a sensitivity factor as

$$S_p = \partial \ln\left[-\frac{X}{Y}\right] \Big/ \partial \ln[p], \tag{52}$$

where p is some thermophysical property of interest. To determine the sensitivity of h_K or κ over the pump probe delay time in the TDTR data, we perturb the value of h_K or κ by 1% in calculations of Eq. (52) so effectively our sensitivity becomes

$$S_p = 100\frac{Y}{X}\partial\left[\frac{X}{Y}\right], \tag{53}$$

where the derivative of the ratio is estimated by subtracting the model calculations from the perturbed model calculations. Figure 32 shows the sensitivities of the thermal transport from TDTR as a function of pump probe delay time for a 100 nm Al film on Si and SiO_2 substrates at room temperature assuming a 15 μm pump and probe spot size. In the sensitivity calculations, the thermal boundary conductance is taken as 200 MW m^{-2} K^{-1} for Al/Si and 50 MW m^{-2} K^{-1} for Al on SiO_2 [47, 63]. We use literature values for the thermal properties of the Al, Si, and SiO_2 [64]. There are two aspects of the sensitivity curve that are important when fitting the model to the TDTR data, the magnitude and the curvature. An optimal sensitivity curve will exhibit a large magnitude and variance over the pump-probe delay time. For example, the sensitivity to the thermal conductivity of the Si substrate is ideal since it is relatively large and very dynamic compared to that of SiO_2. The sensitivity to h_K across the Al/Si interface is also appealing but loses sensitivity around 500 – 1,000 ps. Note that the sensitivity of the model in the Al/SiO_2 system is primarily due to the thermal conductivity of the substrate. For low thermal conductivity structures, this is powerful if only the thermal conductivity needs to be determined and not h_K since it reduces the number of free parameters in the fit. We do not include the sensitivity to the Al film thermal conductivity since the TDTR measurements are nearly insensitive to this parameter over the majority of the pump-probe time delay. Assuming a diffusivity of Al as $D = 97.1\text{x}10^{-6}$ m^2 s^{-1}, the time it takes for the heat to diffuse through the film is given by $\approx d^2/D$ where d is the film thickness [64]. For a 100 nm Al film, the thermal energy has fully diffused through the film thickness after only 100 ps.

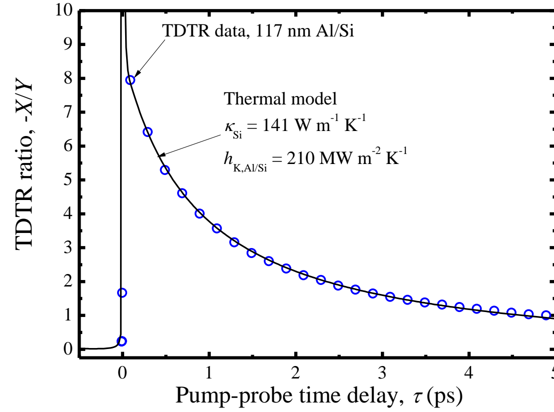

Figure 32. TDTR data from a 117 nm Al film evaporated on a Si substrate along with the best fit from the thermal model. The thermophysical properties determined from the model best fits are h_K = 210 MW m^{-2} K^{-1} for the Al/Si interface and κ = 141 W m^{-1} K^{-1} for the Si substrate.

TDTR data on a 117 nm Al film evaporated onto a single crystalline, lightly doped Si substrate are shown in Figure 33 along with the best fit from the thermal model. The thermal conductivity of the 117 nm Al film is 200 W m^{-1} K^{-1}, as determined from electrical resistivity measurement and the Wiedemann-Franz Law. Although this procedure for determining the Al thermal conductivity is really a measure of in-plane conductivity where the model requires cross plane, since the Al film is polycrystalline, it is valid to assume that the in-plane and cross plane conductivities are equivalent for an approximately 100 nm Al film. The thickness of the Al film was measured with picosecond ultrasonics, another powerful aspect of this TDTR experimental setup [65, 66]. The thermal model, which accounts for pulse accumulation and radial spreading, is fit to the data by adjusting $h_{K,12}$ and κ_2. The data shown here are the real component of the lock-in signal divided by the imaginary component; i.e., $-X/Y$. This approach of normalizing the signal by the imaginary component of the voltage cancels out detection noise and makes the signal insensitive to various experimental parameters that can be difficult to account for during data analysis [49]. This approach is the same as using the phase of the signal [38, 48]. Note that analyzing the ratio (i.e., $-X/Y$) also removes the requirement of scaling the model to the data, thereby giving more sensitivity in the fit to various thermophysical parameters.

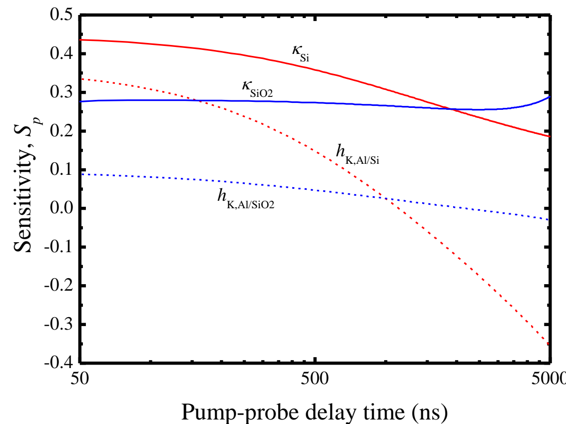

Figure 33. Thermal sensitivities in TDTR to h_K and κ of the substrate in 100 nm Al/Si and Al/SiO_2 systems.

4.2.2. In-Plane TDTR

Using the measurement approach and apparatus discussed above, TDTR measurements can easily be extended to interrogate suspended structures along with anisotropy in thermal conductivity. Using the thermal model outlined above, the TDTR signal can be interpreted on a suspended structure by simply prescribing the layer adjacent to the back end of the suspended structure as highly insulative. For example, for a structure that has a 100 nm Al transducer on a 500 nm Si membrane that is suspended, the thermal model would treat the "layer" underneath the Si (i.e., the air) as a highly insulative, semi-infinite material (this can be accomplished by arbitrarily setting the thermal conductivity and thermal boundary conductance for that layer to extremely low values). This is valid as long as convective and radiative losses are negligible from the rear face, which is valid for TDTR experiments due to the spot size and time domain of the measurement [67]. In-plane and cross-plane thermal conductivity measurements can be isolated by varying the pump and probe radii along with the modulation frequency. This aspect of TDTR is discussed in detail elsewhere [38, 63]. In brief, at high pump modulation frequencies and large spot sizes, the thermal transport in TDTR experiments is nearly entirely one-dimensional and cross-plane. Decreasing the spot size and modulation frequency leads to a larger in-plane thermal transport component during the measurements. Therefore, by taking two measurements on a sample (one with large spot sizes are high frequencies and one with small spot sizes at low frequencies), both in-plane and cross-plane thermal conductivities can be determined. Care must be taken during the in-plane measurements (small spot size and low frequency), however, since large uncertainties can be introduced into the determined κ due to uncertainties in the spot size and low frequency modulation can introduce relatively noisy signals due to $1/f$ ("pink") noise. In these cases, the spot sizes should be characterized as accurately as possible, along with minimizing any ellipticity in the spots and rigorous error analysis to insure accurate determination of the in-plane thermal conductivity.

5. RESULTS

This section summarizes the experimental results that were obtained and steps in the course of this program leading up to the validation of ***the doubling*** in the *ZT* value over that of bulk in a silicon phononic crystal membrane.

5.1. Experimental Measurements

5.1.1. Measurement of Thermal and Electrical Conductivity Reduction in PnCs

To investigate the impact of PnCs on the silicon thermal conductivity, various lattice constants and hole diameters in square lattices were prepared, as summarized in Table 2. The smallest design feature size was 200 nm, which was limited by the capability of the ASML lithography stepper in Sandia's Microelectronics Development Laboratory (MDL). The actual hole sizes had some discrepancy compared to the designed size. In general, holes with designed diameters smaller than 300 nm turned out to be smaller than the design, and ones with larger than 300 nm became larger than the actual design. Device ID-1 is the control device which does not have any holes in the silicon membrane. The limiting dimensions were determined as the minimum distance between two holes.

Table 2. Summary of designed hole pitches and diameters.

Device ID	1	2	3	4	5	6	7	8	9	10	11	12	13	14	15	16	17
A, lattice constant (nm)	N/A	500	500	600	600	600	700	700	700	700	700	800	800	800	800	800	900
D, design diameter (nm)	N/A	250	300	250	300	350	250	300	350	400	450	300	350	400	450	500	500
D_m, measured diameter (nm)	N/A	213.6	303.3	204.9	295.9	365.6	209	294.5	360.5	424.5	486.5	290.9	357.6	419.6	479.8	535	532.6
L_m, limiting dimensions(nm)	N/A	286.4	196.7	395.1	304.1	234.4	491	405.5	339.5	275.5	213.5	509.1	442.4	380.4	320.2	265	367.4

Because the exact sizes of phononic crystal holes are very critical for this study, we optically measured the actual fabricated hole sizes for all designed diameters. First, SEM images of 16~20 holes were captured from 10 different locations in the fabricated devices, and using the MATLAB image processing toolbox, the areas of holes were estimated by pixel counting and their corresponding diameters were calculated. Figure 34 explains the detailed image processing procedure, and the measured diameters using this method are summarized in Table 2. As seen in the table, the actual fabricated hole sizes had some discrepancies compared to the designed dimensions. In general, it was observed that holes with designed diameters smaller than 300 nm became smaller than the designed dimension, while holes designed for diameters larger than 300 nm turned out to be larger than the actual design. For all of the data analysis conducted in this study, the actual measured hole sizes were used instead of the designed hole sizes.

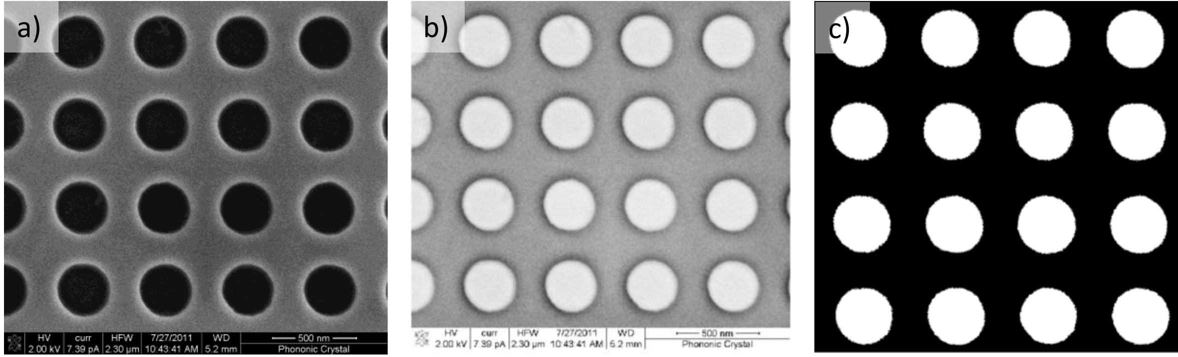

Figure 34. The steps of image processing for the hole size measurement. a) SEM images containing 16~20 holes were taken. b) Complementary images were made. c) By setting the gray threshold, the hole boundaries are determined and the number of white pixels were counted to calculated hole areas and diameters.

All the measured data are summarized in Figure 35 and Table 3. As can be seen in Figure 35, all the samples containing holes (phononic crystals) showed significant reduction in thermal conductivity compared to the control device (Device ID-1), which had no holes.

Table 3. Summary of the measured thermal conductivity values (300 K).

Device ID	**1**	**2**	**3**	**4**	**5**	**6**	**7**	**8**	**9**	**10**	**11**	**12**	**13**	**14**	**15**	**16**	**17**
A, lattice constant (nm)	N/A	500	500	600	600	600	700	700	700	700	700	800	800	800	800	800	900
D_m, measured diameter (nm)	N/A	213.6	303.3	204.9	295.9	365.6	209	294.5	360.5	424.5	486.5	290.9	357.6	419.6	479.8	535	532.6
L_m, limiting dim. (nm)	N/A	286.4	196.7	395.1	304.1	234.4	491	405.5	339.5	275.5	213.5	509.1	442.4	380.4	320.2	265	367.4
mean k_m (W/mK)	104.0	63.3	42.4	73.7	56.3	42.8	79.4	65.7	54.1	43.3	32.6	72.2	63.4	53.5	44.4	35.8	45.1
st. dev k_m (W/mK)	1.4	1.3	1.6	1.5	1.3	1.4	1.0	1.4	1.2	1.4	1.3	1.1	1.1	1.1	1.2	1.2	1.0

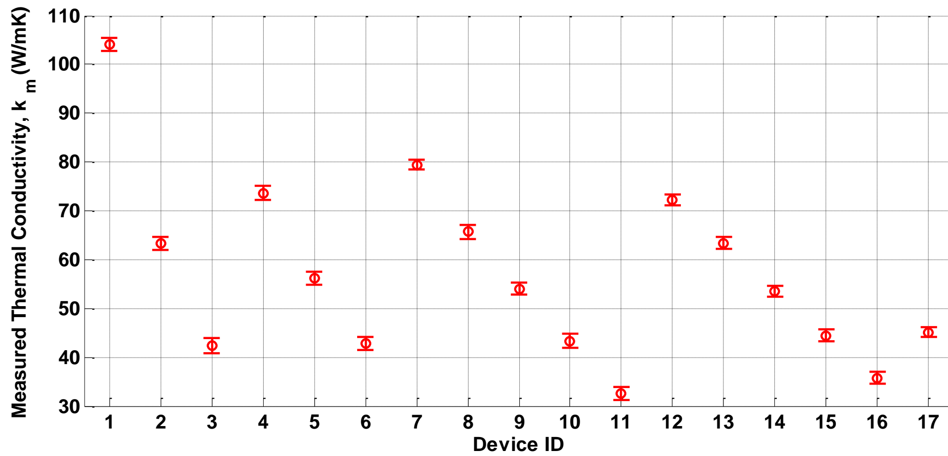

Figure 35. Measured thermal conductivity values. The control device (Device ID-1), which has no holes, measured k_m = 104 W m^{-1} K^{-1}; this is consistent with literature values for 500 nm-thick single crystal silicon.

To better understand the thermal effects of the PnC, the first step is to evaluate how much of a contribution to the reduction in thermal conductivity came from simple volume reduction when introducing the air holes. The Maxwell-Eucken model [26, 68] is one of the most widely used methods to estimate the reduction in conductivity due to the volume removal effect. The Eucken factor is given as

$$F_{Eucken} = \frac{1-\phi}{1+2\phi/3}, \tag{54}$$

where ϕ is the porosity of the material. This empirical model is based on randomly distributed spherical pores, but is known to agree well with many general cases. We have also conducted ANSYS FEM analysis for the case of cylindrical holes arranged in a square lattice as shown in Figure 36a. This ANSYS simulation captures only classical volume reduction effect, not any phononic effects. As shown in the comparison plot in Figure 36b, the Maxwell-Eucken model approximates the trend of the volume reduction effect. However, compared to the ANSYS FEM results, the Maxwell-Euken precision is limited. In this study we have used F_{FEM} (volume reduction effect factor from ANSYS FEM), instead of F_{Eucken}, which is shown as the red curve in Figure 36b.

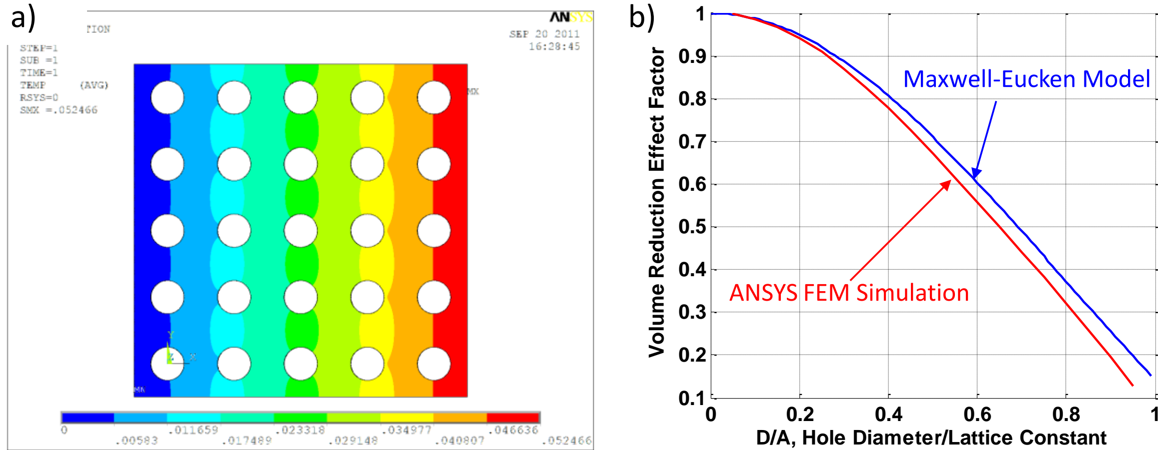

Figure 36. a) ANSYS FEM simulation for the effective conductivity reduction by introducing periodic holes. b) Volume reduction effect factors comparison between ANSYS FEM simulation model and Maxwell-Eucken model.

Table 4 and Figure 37 compare the relative thermal and electrical conductivity compared to the control sample for each device design as well as their corresponding, F_{FEM}. As can be seen, for all samples, the ratio of the thermal conductivities, $k_m/k_{m,control}$, (relative thermal conductivity with respect to the control device), were much lower than that predicted from ANSYS FEM simulation. In contrast, the ratio of the electrical conductivities, $\sigma_m/\sigma_{m,control}$ (relative electrical conductivity with respect to the control device), measured from n-type doped samples with the same hole pitches and diameters, match very well with F_{FEM}, the ANSYS FEM predictions due to the volume reduction effect. These results suggest that inclusion of sub-micron periodic holes reduced the thermal conductivity much more than the contribution from the volume reduction effect, whereas the electrical conductivities are reduced simply by the amount of volume reduction.

Table 4. Comparison between $k_m/k_{m,control}$ (relative thermal conductivity with respect to the control device), $\sigma_m/\sigma_{m,control}$ (relative electrical conductivity with respect to the control device), and F_{FEM} (modeled volume reduction effect from ANSYS FEM).

Device ID	1	2	3	4	5	6	7	8	9	10	11	12	13	14	15	16	17
A (nm)	N/A	500	500	600	600	600	700	700	700	700	700	800	800	800	800	800	900
D_m, (nm)	N/A	213.6	303.3	204.9	295.9	365.6	209	294.5	360.5	424.5	486.5	290.9	357.6	419.6	479.8	535	532.6
$k_m/ k_{m,control}$	1	0.608	0.408	0.708	0.541	0.412	0.763	0.632	0.520	0.416	0.313	0.694	0.609	0.514	0.427	0.344	0.434
$\sigma_m/ \sigma_{m,control}$	1	0.744	0.532	0.823	0.668	0.535	0.864	0.747	0.647	0.543	0.434	0.802	0.726	0.641	0.556	0.473	0.568
F_{FEM}	1	0.750	0.551	0.834	0.679	0.547	0.871	0.757	0.655	0.551	0.447	0.813	0.729	0.645	0.558	0.478	0.568

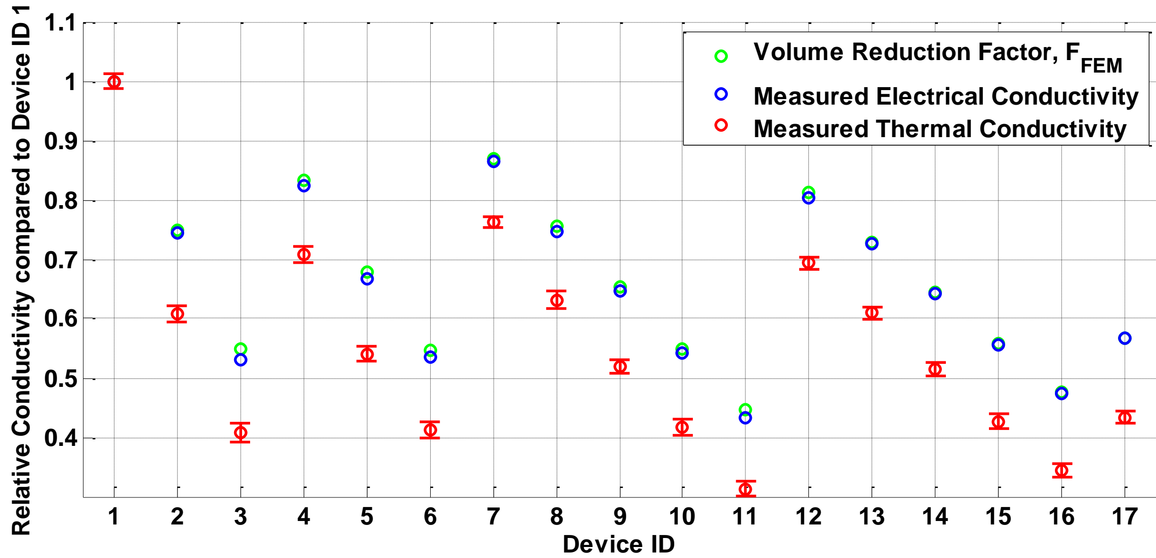

Figure 37. Comparison between $k_m/k_{m,control}$ (relative thermal conductivity with respect to the control device), $\sigma_m/ \sigma_{m,control}$ (relative electrical conductivity with respect to the control device), and F_{FEM} (reduction effect factor from ANSYS FEM). The measured $\sigma_m/ \sigma_{m,control}$ match very well with F_{FEM} for all Device IDs; some data points are difficult to distinguish because they exactly overlap with each other. However, the $k_m/k_{m,control}$ ratios are much smaller than F_{FEM} for all cases, inferring a reduction in the thermal conductivity that is beyond the contribution from the volume reduction effect.

To evaluate phononic impact on thermal conductivity, all measured relative thermal conductivity values are normalized by F_{FEM}, i.e.,

$$k_n = \frac{k_m/k_{m,control}}{F_{FEM}}. \quad (55)$$

This k_n indicates how much the thermal conductivity is reduced beyond the contribution from the volume reduction effect. For example, Device ID-11 had a measured k_n = 0.696 in Table 5, which means thermal conductivity was reduced by an additional 30.4%, even after taking the volume reduction effect into account.

Table 5. Summary of k_n, relative thermal conductivity values ($k_m/k_{m,control}$) normalized by ANSYS FEM volume reduction effect factors (F_{FEM}).

Device ID	1	2	3	4	5	6	7	8	9	10	11	12	13	14	15	16	17
A, lattice constant (nm)	N/A	500	500	600	600	600	700	700	700	700	700	800	800	800	800	800	900
D_m, measured diameter (nm)	N/A	213.6	303.3	204.9	295.9	365.6	209	294.5	360.5	424.5	486.5	290.9	357.6	419.6	479.8	535	532.6
L_m, limiting dim. (nm)	N/A	286.4	196.7	395.1	304.1	234.4	491	405.5	339.5	275.5	213.5	509.1	442.4	380.4	320.2	265	367.4
mean k_n	1	0.805	0.736	0.844	0.790	0.747	0.871	0.829	0.787	0.750	0.696	0.847	0.830	0.792	0.759	0.714	0.759
st. dev. k_n	0	0.006	0.017	0.008	0.007	0.013	0.008	0.009	0.007	0.013	0.017	0.007	0.003	0.005	0.009	0.013	0.007

Figure 38 compares the normalized thermal conductivity, k_n, versus limiting dimension (minimum spacing between holes) with the same lattice constant. For all measured devices, k_n consistently decreases as the limiting dimension decreases, implying that incoherent scattering plays a significant role in the thermal conductivity reduction.

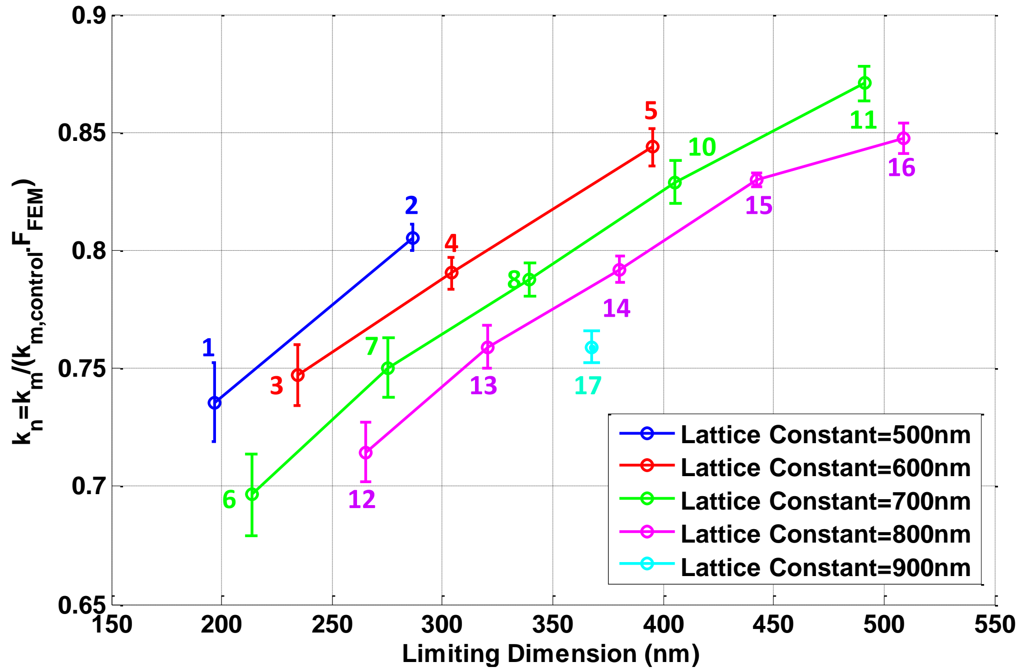

Figure 38. Comparison of k_n versus limiting dimension with the same lattice constant. As the limiting dimension decreases, the k_n decreases, which indicates that incoherent scattering plays a significant role to reduce thermal conductivity of phononic crystals. Numbers adjacent the data points are the Device IDs. Each data point is averaged from 6 measured devices.

Figure 39 compares k_n versus lattice constant at the same limiting dimension; k_n decreases as the lattice constant increases even with the same limiting dimension. These differences in k_n indicate that incoherent scattering is not the only mechanism contributing to the reduction in thermal conductivity beyond the volume reduction effect. A schematic in Figure 40 describes a hypothetical explanation for this phenomenon. At a given limiting dimension, as the lattice constant increases the two Bragg resonant frequencies, $f_{\Gamma\text{-}X}$ and $f_{\Gamma\text{-}M}$, of the phononic crystals approach each other. Therefore, it is possible that at a certain lattice constant a phononic

bandgap opens, and as the lattice constant increases the bandgap widens, enhancing coherent scattering and resulting in a further reduction in thermal conductivity. It is well known that vacuum/solid phononic crystals only open a bandgap at very large filling fractions and that the bandgap widens as the filling fraction increases [22].

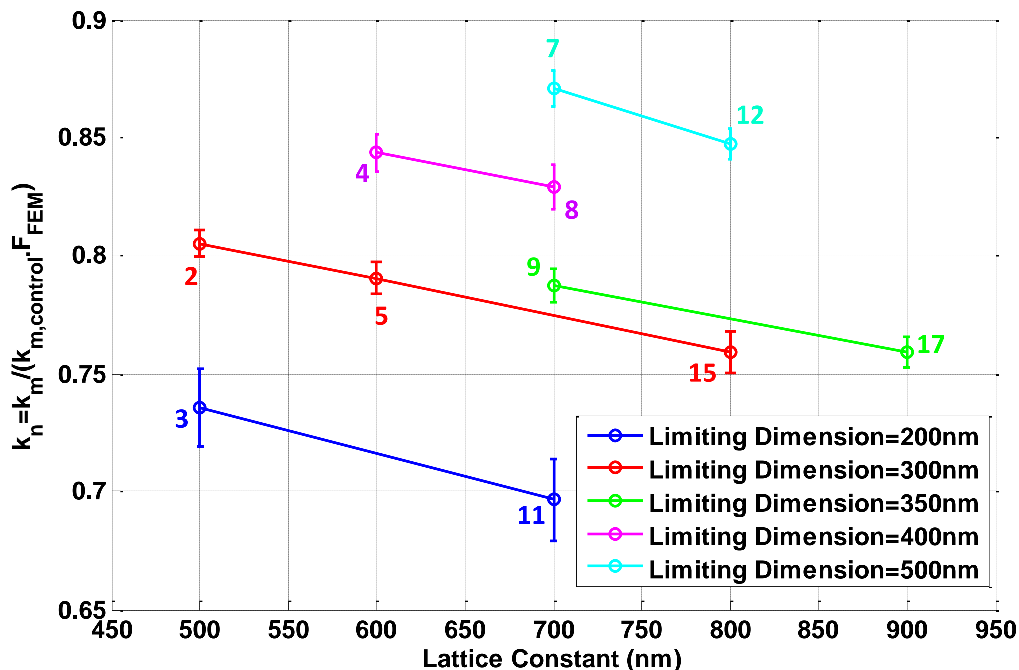

Figure 39. Comparison of k_n versus lattice constant with the same limiting dimension. Even with the same limiting dimensions, k_n decreases, as the lattice constant increases, which infers that incoherent scattering is not the only mechanism for the thermal conductivity reduction. Numbers adjacent the data points are the Device IDs. Each data point is averaged from 6 measured devices.

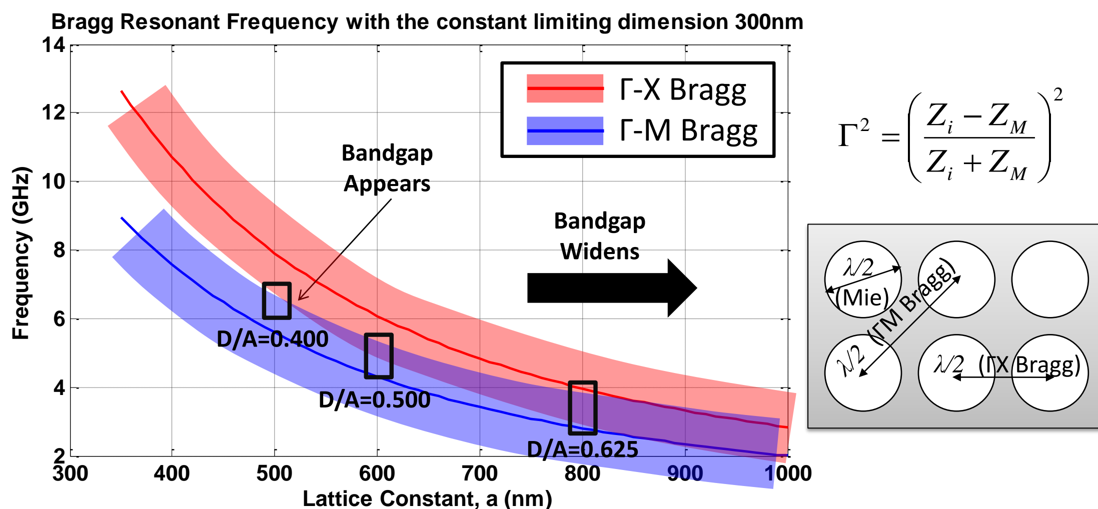

Figure 40. Hypothetical schematic explaining coherent scattering enhancement at a given limiting dimension. As the lattice constant increases, the two Bragg resonant frequencies approach each other, opening a phononic bandgap at some point which widens as the lattice constant increases.

In summary, in single crystal silicon phononic crystals the thermal conductivity, unlike electrical conductivity, is reduced much more than what is predicted by the simple volume reduction effect. The primary contribution to this further reduction in thermal conductivity beyond the volume reduction effect is incoherent scattering at small limiting dimensions between the holes, but is supplemented by coherent scattering from the periodically placed sub-micron-sized holes.

5.1.2. Dependence of Thermal Conductivity on Lattice Type and Topology

Each suspended island test platform (see Section 4.1.2) was calibrated prior to transferring a PnC to ensure the platform itself behaved linearly as expected and to determine α separately for the heater and sensor. During the calibration process, the temperature of the die containing the test platform was ramped up from 20 to 60° C in increments of 5° C and then back down in similar increments. At each temperature the resistances of the heater and sensing islands were sampled five times. Figure 41 shows the calibration data from one of the test platforms. Both the heater and sensor show linear trends across a 40° C temperature range.

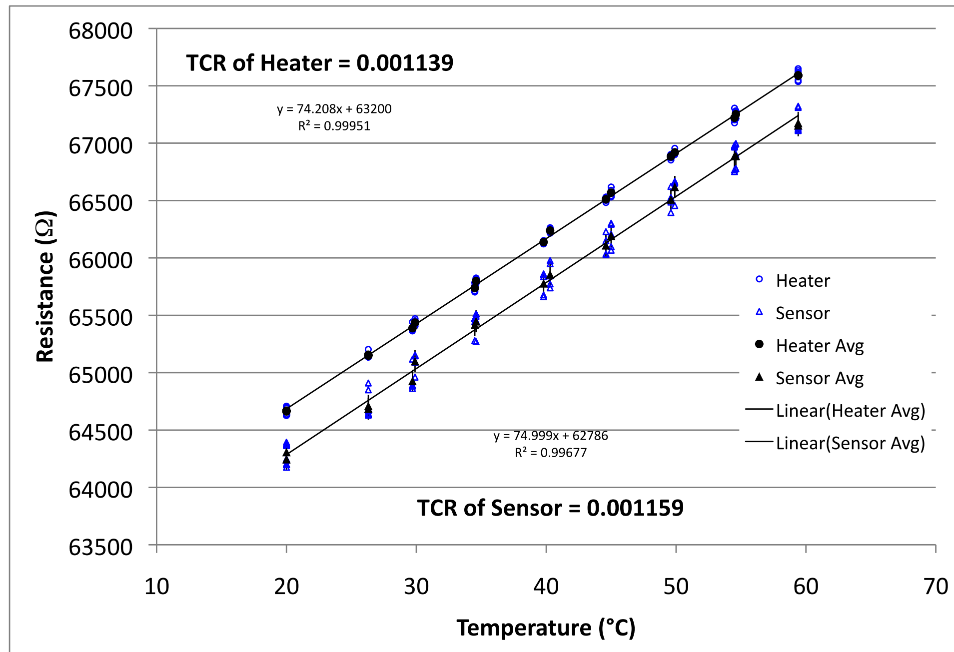

Figure 41. Calibration data from a test platform. Black refers to the heater island and blue refers to the sensor island. Both the heater and sensor showed linear trends across a 40° C temperature range.

After calibrating the platforms and transferring the PnCs, the test platform was placed under vacuum (< 1 mTorr) and the heat input vs. resistance relationship was determined. Testing the system in vacuum conditions ensured minimal heat was lost due to convection. Input power to the heater was ramped up and down from 1 µW up to 10 µW twice. At each input power, the resistances of the heater and sensing islands were sampled five times for a total of 20 measurements at each input power level. Figure 42 shows the plot of input power versus heater resistance for the hexagonal PnC.

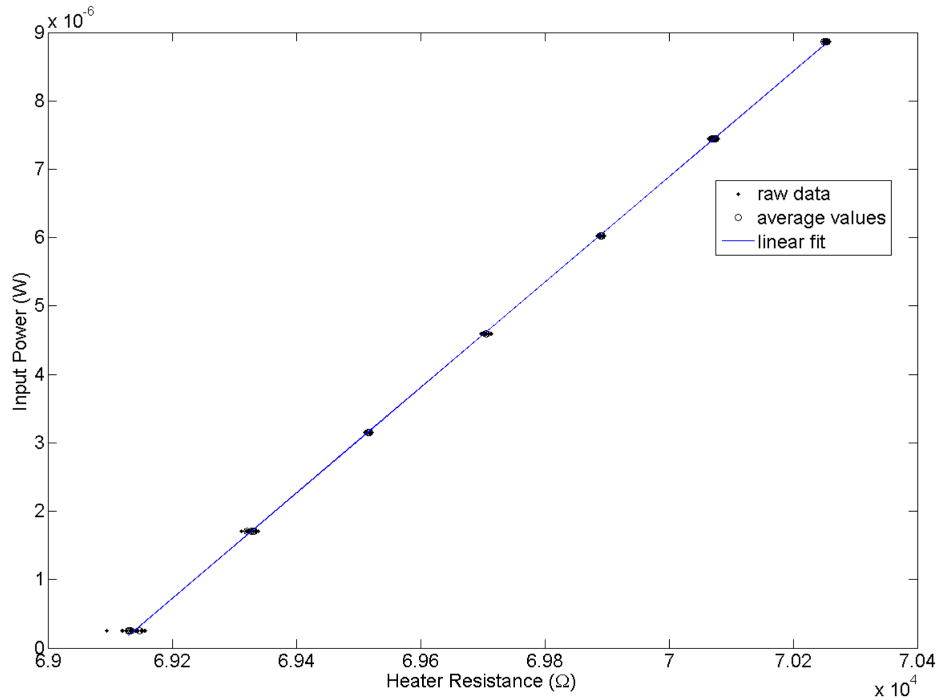

Figure 42. Plot of input power vs. heater resistance for the hexagonal PnC.

Table 6 lists the preliminary measured thermal conductivity values for the hexagonal ("Hex") and simple cubic ("Sqr") PnCs. The last column takes porosity into account for a Si film with the same thickness. For a 250 nm thick Si film, the thermal conductivity goes from a bulk value of 148 W/m-K down to 80 W/m-K [69]. If the porosity of the PnC is accounted for, then the thermal conductivity drops to approximately 70 W/m-K [68]. Based on the large difference between the porous thermal conductivity value and the measured thermal conductivity of the PnC, it is clear that simply removing material does not account for the ability of the PnC to reduce the thermal conductivity of silicon. This is evidence that the PnC itself creates coherent scattering that reduces the thermal conductivity of Si. If it were based solely on incoherent scattering, one would expect the porous and PnC thermal conductivity values to be roughly equal.

Table 6. Results of thermal conductivity for hexagonal and simple cubic PnC

Lattice Type	Thickness (nm)	Lattice Spacing (nm)	Via Diameter (nm)	Porosity	κ_{PnC} (W/m-K)	κ_{porous} (W/m-K)
Hex	250	250	82	0.058	5.7	73.2
Sqr	250	250	83	0.084	5.9	70.3

5.1.3. Full ZT Characterization of PnC Samples

Test structures for *ZT* characterization were designed similarly to the thermal conductivity test structures. As shown in Figure 43, in a symmetric bridge structure, serpentine heater/temperature sensor is again installed at the center, however half of the bridge was n-type doped (Ph) and the other was p-type doped (B). Also, at the bridge ends, electrical contacts we were provided. When heat is supplied at the bridge center, the temperature gradient induces

electricity due to the thermoelectric effect. Therefore, by measuring the voltage potential and current at the bridge ends, device thermoelectric characteristics can be measured.

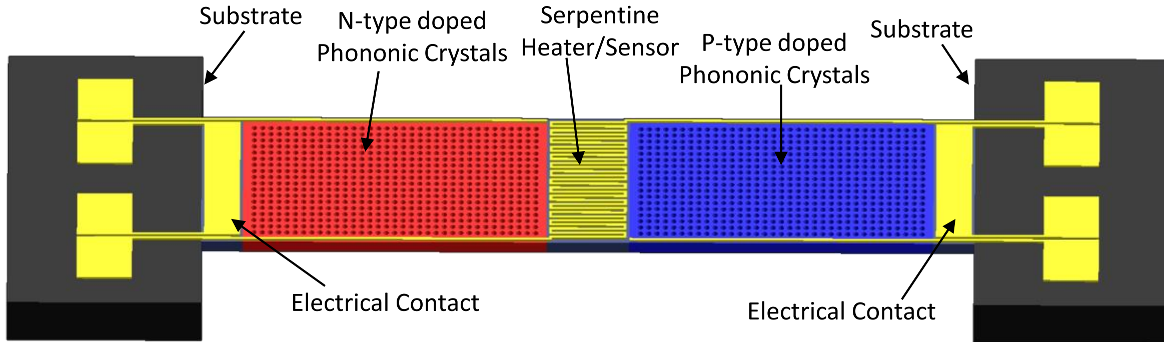

Figure 43. A schematic of the *ZT* measurement test structure design. A phononic crystal bridge is suspended from the substrate. One half of the bridge is doped n-type while the other half is doped p-type. Electrical contacts are provided at the bridge ends to measure the amount of thermoelectrically induced current and voltage when heat is supplied at the bridge center.

The fabrication process of *ZT* measurement device is similar to that of thermal conductivity test structures, except for some extra steps required for doping and electrical contact. Figure 44 shows the schematics of the *ZT* measurement device fabrication process. Starting from SOI wafers, the wafers are first locally doped n-type and p-type using phosphorous and boron implantation, respectively (Figure 44a and Figure 44b). The target doping concentration is $10^{20}/cm^3$ for both dopants. Next, an undoped amorphous silicon insulation layer is deposited, followed by high temperature annealing. Electrical vias to the doped region are patterned penetrating the insulation layer (Figure 44c). Aluminum traces, bondpads, and heaters/temperature sensors are defined (Figure 44d), followed by the PnC and release trench etching (Figure 44e). Finally, the test structure is release using a HF vapor etch (Figure 44f).

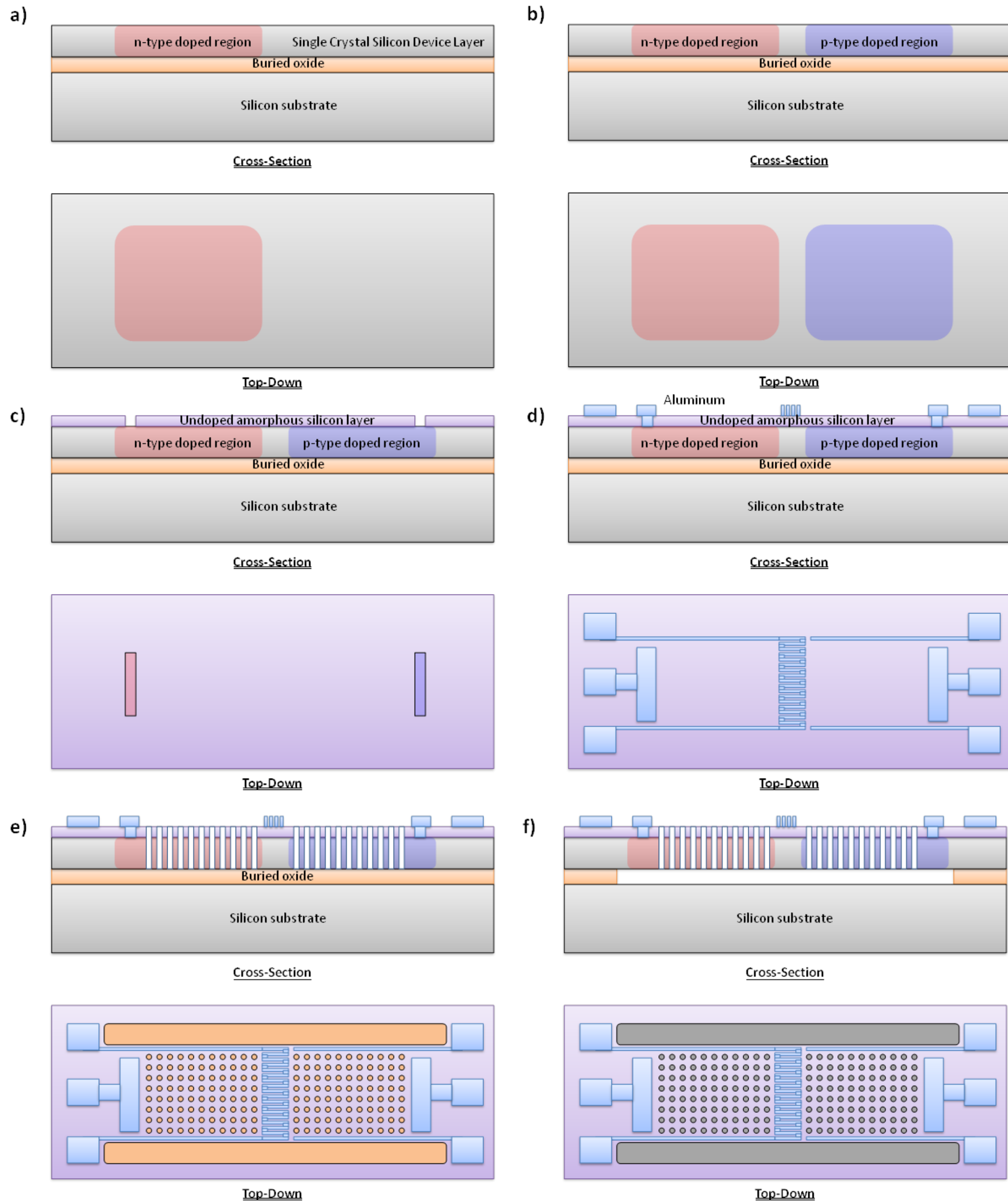

Figure 44. Schematics of the fabrication process for the *ZT* measurement structures.

The recent *ZT* measurement test structure fabrication run had an issue with the high temperature annealing equipment leaving the stress in the a-Si insulation layer unrelieved; as a result, after the HF release all the bridge structures were snapped down to the substrate. Currently, another fabrication run is ongoing resolving this issue. At the time of this report, we have measured only the electrical conductivities of the devices that have not been HF released. The *ZT* measurement test structures are still under fabrication, and once the fabrication is completed the *ZT* characteristics of the phononic crystal structures will be measured. However, since the Seebeck coefficient of the air holes is essentially zero, it is anticipated that the PnC patterning using only

air holes will result in an overall Seebeck coefficient equivalent to that of the doped silicon matrix. Assuming that this indeed is the case, our results indicate an increase in *ZT* by a factor of up to 1.5 over that of an unpatterned slab and by up to a factor of 2 over that of bulk silicon. Figure 45 below shows a summary of the anticipated *ZT* values for some of our PnC samples.

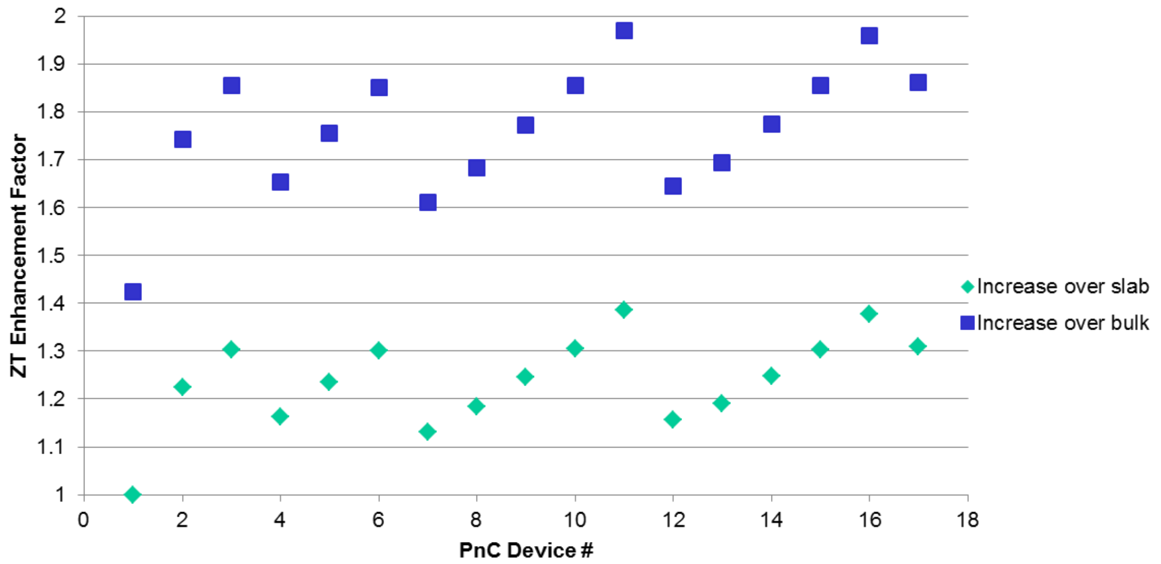

Figure 45. Sumary of predicted *ZT* enhancement for the fabricated PnC devices.

6. CONCLUSIONS AND FUTURE OUTLOOK

This work represents a revolutionary advance in the engineering of thermoelectric materials for optimal, high-*ZT* performance. We have demonstrated the significant reduction of the thermal conductivity of silicon using phononic crystal structuring using MEMS-compatible fabrication techniques and in a planar platform that is amenable to integration with typical microelectronic systems. The measured reduction in thermal conductivity as compared to bulk silicon was about a factor of 20 in the cross-plane direction [26], and a factor of 6 in the in-plane direction. Since the electrical conductivity was only reduced by a corresponding factor of about 3 due to the removal of conductive material (i.e., porosity), and the Seebeck coefficient should remain constant as an intrinsic material property, this corresponds to an effective enhancement in *ZT* by a factor of 2. Given the number of papers in literature devoted to only a small, incremental change in *ZT*, the ability to boost the *ZT* of a material by a factor of 2 *simply by reducing thermal conductivity* is groundbreaking.

The results in this work were obtained using silicon, a material that has benefitted from enormous interest in the microelectronics industry and that has a fairly large thermoelectric power factor. In addition, the techniques and scientific understanding developed in the research can be applied to a wide range of materials, with the caveat that the thermal conductivity of such a material be dominated by phonon, rather than electron, transport. In particular, this includes several thermoelectric materials with attractive properties at elevated temperatures (i.e., greater than room temperature), such as silicon germanium and silicon carbide. It is reasonable that phononic crystal patterning could be used for high-temperature thermoelectric devices using such materials, with applications in energy scavenging via waste-heat recovery and thermoelectric cooling for high-performance microelectronic circuits.

The only part of the *ZT* picture missing in this work was the experimental measurement of the Seebeck coefficient of our phononic crystal devices. While a first-order approximation indicates that the Seebeck coefficient should not change significantly from that of bulk silicon, we were not able to actually verify this assumption within the timeframe of the project. Additionally, with regards to future high-temperature applications of this technology, we plan to measure the thermal conductivity reduction factor of our phononic crystals as elevated temperatures to confirm that it does not diminish, given that the nominal thermal conductivity of most semiconductors, including silicon, decreases with temperature above room temperature. We hope to have the opportunity to address these concerns and further advance the state-of-the-art of thermoelectric materials in future projects.

7. REFERENCES

1. G. J. Snyder and E. S. Toberer, Complex thermoelectric materials, in *Nat. Mater.* Vol. 7, No. 2, pp. 105-14, February 2008.
2. J. R. Sootsman, D. Y. Chung and M. G. Kanatzidis, New and Old Concepts in Thermoelectric Materials, in *Angewandte Chemie International Edition* Vol. 48, No. 46, pp. 8616-39, 2009.
3. H. J. Goldsmid, *Introduction to Thermoelectricity*. Springer Berlin Heidelberg, Berlin, Heidelberg, Berlin, Heidelberg, 2009.
4. , !!! INVALID CITATION !!!
5. S. M. Lee, D. G. Cahill and R. Venkatasubramanian, Thermal conductivity of Si-Ge superlattices, in *Appl. Phys. Lett.* Vol. 70, No. 22, pp. 2957-59, 2 June 1997.
6. R. Venkatasubramanian, Lattice thermal conductivity reduction and phonon localizationlike behavior in superlattice structures, in *Phys. Rev. B, Condens. Matter* Vol. 61, No. 4, pp. 3091-97, 15 January 2000.
7. R. Venkatasubramanian, E. Siivola, T. Colpitts and B. O'Quinn, Thin-film thermoelectric devices with high room-temperature figures of merit, in *Nature* Vol. 413, No. 6856, pp. 597-602, 11 October 2001.
8. L. D. Hicks, T. C. Harman, X. Sun and M. S. Dresselhaus, Experimental study of the effect of quantum-well structures on the thermoelectric figure of merit, in *Phys. Rev. B, Condens. Matter* Vol. 53, No. 16, pp. R10493-R96, 15 April 1996.
9. Y. Mune, H. Ohta, K. Koumoto, T. Mizoguchi and Y. Ikuhara, Enhanced Seebeck coefficient of quantum-confined electrons in SrTiO[sub 3]/SrTi[sub 0.8]Nb[sub 0.2]O[sub 3] superlattices, in *Appl. Phys. Lett.* Vol. 91, No. 19, pp. 192105-3, 2007.
10. I. El-Kady, R. H. Olsson, III and J. G. Fleming, Phononic band-gap crystals for radio frequency communications, in *Appl. Phys. Lett.* Vol. 92, No. 23, pp. 233504-1-3, 9 June 2008.
11. M. F. Su, R. H. Olsson, Z. C. Leseman and I. El-Kady, Realization of a phononic crystal operating at gigahertz frequencies, in *Appl. Phys. Lett.* Vol. 96, No. 5, p. 053111 (3 pp.), 1 February 2010.
12. R. H. Olsson, III and I. El-Kady, Microfabricated phononic crystal devices and applications, in *Meas. Sci. Technol.* Vol. 20, No. 1, p. 012002 (13 pp.), January 2009.
13. D. P. Sellan, E. S. Landry, J. E. Turney, A. J. H. McGaughey and C. H. Amon, Size effects in molecular dynamics thermal conductivity predictions, in *Physical Review B* Vol. 81, No. 21, p. 214305, 2010.
14. D. P. Sellan, J. E. Turney, A. J. H. McGaughey and C. H. Amon, Cross-plane phonon transport in thin films, in *J. Appl. Phys.* Vol. 108, No. 11, p. 113524, 2010.
15. P. E. Hopkins, C. M. Reinke, M. F. Su, R. H. O. III, E. A. Shaner, Z. C. Leseman, J. R. Serrano, L. M. Phinney and I. El-Kady, Massive reduction in the thermal conductivity of single crystalline silicon by phononic crystal patterning, in *submitted to Nano Letters*,
16. A. Ward and D. A. Broido, Intrinsic phonon relaxation times from first-principles studies of the thermal conductivities of Si and Ge, in *Physical Review B* Vol. 81, No. 8, p. 085205, 2010.
17. M. G. Holland, Analysis of lattice thermal conductivity, in *Phys. Rev.* Vol. 132, No. 6, pp. 2461-71, 15 Dec. 1963.
18. C. Kittel, *Introduction to Solid State Physics*. Wiley, Hoboken, NJ, 2005.

19. M. M. Sigalas and E. N. Economou, Elastic and acoustic wave band structure, in *J. Sound Vib.* Vol. 158, No. 2, pp. 377-82, 22 October 1992.
20. M. S. Kushwaha, P. Halevi, G. Martinez, L. Dobrzynski and B. Djafari-Rouhani, Theory of acoustic band structure of periodic elastic composites, in *Phys. Rev. B, Condens. Matter* Vol. 49, No. 4, pp. 2313-22, 15 January 1994.
21. J. O. Vasseur, P. A. Deymier, B. Djafari-Rouhani, Y. Pennec and A. C. Hladky-Hennion, Absolute forbidden bands and waveguiding in two-dimensional phononic crystal plates, in *Phys. Rev., B, Condens, Matter Mater. Phys.* Vol. 77, No. 8, pp. 085415-1-15, 15 February 2008.
22. C. M. Reinke, M. F. Su, R. H. Olsson III and I. El-Kady, Realization of optimal bandgaps in solid-solid, solid-air, and hybrid solid-air-solid phononic crystal slabs, in *Appl. Phys. Lett.* Vol. 98, No. 6, p. 061912, 2011.
23. M. T. Dove, *Introduction to Lattice Dynamics*. Press Syndicate of the University of Cambridge, New York City, NY, 1993.
24. J. Tersoff, New empirical approach for the structure and energy of covalent systems, in *Physical Review B* Vol. 37, No. 12, pp. 6991-7000, 1988.
25. J. Tersoff, Empirical interatomic potential for silicon with improved elastic properties, in *Physical Review B* Vol. 38, No. 14, pp. 9902-05, 1988.
26. P. E. Hopkins, C. M. Reinke, M. F. Su, R. H. Olsson, E. A. Shaner, Z. C. Leseman, J. R. Serrano, L. M. Phinney and I. El-Kady, Reduction in the thermal conductivity of single crystalline silicon by phononic crystal patterning, in *Nano Letters* Vol. 11, No. 1, pp. 107-12, 2010.
27. P. D. Prewett and D. K. Jefferies, Characteristics of a gallium liquid metal field emission ion source, in *J. Phys. D, Appl. Phys.* Vol. 13, No. 9, p. 1747, 1980.
28. J. Orloff, *Handbook of Charged Particle Optics*. CRC Press, Boca Raton, FL, 2009.
29. J. F. Ziegler, J. P. Biersack and M. D. Ziegler, *SRIM - The Stopping and Range of Ions in Matter*. SRIM Co., 2008.
30. L. C. Linares and S. S. Li, An Improved Model for Analyzing Hole Mobility and Resistivity in p-Type Silicon Doped with Boron, Gallium, and Indium, in *Journal of The Electrochemical Society* Vol. 128, No. 3, pp. 601-08, 1981.
31. M. Asheghi, Thermal conduction in doped single-crystal silicon films, in *J. Appl. Phys.* Vol. 91, No. 8, p. 5079, 2002.
32. A. I. Hochbaum, R. Chen, R. D. Delgado, L. Wenjie, E. C. Garnett, M. Najarian, A. Majumdar and Y. Peidong, Enhanced thermoelectric performance of rough silicon nanowires, in *Nature* Vol. 451, No. 7175, pp. 163-67, 10 January 2008.
33. P. Kim, L. Shi, A. Majumdar and P. L. McEuen, Thermal Transport Measurements of Individual Multiwalled Nanotubes, in *Phys. Rev. Lett.* Vol. 87, No. 21, p. 215502, 2001.
34. Goettler, D. F. et al., Realization of a 33 GHz Phononic Crystal Fabricated in a Freestanding Membrane. AIP Advances (Accepted).
35. C. A. Paddock and G. L. Eesley, Transient thermoreflectance from thin metal films, in *J. Appl. Phys.* Vol. 60, No. 1, pp. 285-90, 1 July 1986.
36. Y. K. Koh and D. G. Cahill, Frequency dependence of the thermal conductivity of semiconductor alloys, in *Phys. Rev. B* Vol. 76, p. 075207, 2007.
37. H.-K. Lyeo, D. G. Cahill, B.-S. Lee and J. R. Abelson, Thermal conductivity of phase-change material $Ge_2Sb_2Te_5$, in *Appl. Phys. Lett.* Vol. 89, p. 151904, 2006.

38. A. J. Schmidt, X. Chen and G. Chen, Pulse accumulation, radial heat conduction, and anisotropic thermal conductivity in pump-probe transient thermoreflectance, in *Review of Scientific Instruments* Vol. 79, p. 114902, 2008.
39. W. S. Capinski, H. J. Maris, T. Ruf, M. Cardona, K. Ploog and D. S. Katzer, Thermal-conductivity measurements of GaAs/AlAs superlattices using a picosecond optical pump-and-probe technique, in *Phys. Rev. B* Vol. 59, No. 12, pp. 8105-13, 1999.
40. C. Chiritescu, D. G. Cahill, N. Nguyen, D. Johnson, A. Bodapati, P. Keblinski and P. Zschack, Ultralow thermal conductivity in disordered, layered WSe_2 crystals, in *Science* Vol. 315, pp. 351-53, 2007.
41. R. M. Costescu, D. G. Cahill, F. H. Fabreguette, Z. A. Sechrist and S. M. George, Ultra-low thermal conductivity in W/Al_2O_3 nanolaminates, in *Science* Vol. 303, pp. 989-90, 2004.
42. B. C. Gundrum, D. G. Cahill and R. S. Averback, Thermal conductance of metal-metal interfaces, in *Phys. Rev. B* Vol. 72, p. 245426, 2005.
43. P. E. Hopkins, P. M. Norris, R. J. Stevens, T. Beechem and S. Graham, Influence of interfacial mixing on thermal boundary conductance across a chromium/silicon interface, in *J. Heat Transfer* Vol. 130, p. 062402, 2008.
44. P. E. Hopkins, R. J. Stevens and P. M. Norris, Influence of inelastic scattering at metal-dielectric interfaces, in *J. Heat Transfer* Vol. 130, p. 022401, 2008.
45. R. J. Stoner and H. J. Maris, Kapitza conductance and heat flow between solids at temperatures from 50 to 300 K, in *Phys. Rev. B* Vol. 48, pp. 16373-87, 1993.
46. H.-K. Lyeo and D. G. Cahill, Thermal conductance of interfaces between highly dissimilar materials, in *Phys. Rev. B* Vol. 73, p. 144301, 2006.
47. R. J. Stevens, A. N. Smith and P. M. Norris, Measurement of thermal boundary conductance of a series of metal-dielectric interfaces by the Transient Thermoreflectance Technique, in *J. Heat Transfer* Vol. 127, No. 3, pp. 315-22, 2005.
48. A. Schmidt, M. Chiesa, X. Chen and G. Chen, An optical pump-probe technique for measuring the thermal conductivity of liquids, in *Review of Scientific Instruments* Vol. 79, p. 064902, 2008.
49. D. G. Cahill, Analysis of heat flow in layered structures for time-domain thermoreflectance, in *Rev. Sci. Instrum.* Vol. 75, No. 12, pp. 5119-22, Dec 2004.
50. H. S. Carslaw and J. C. Jaeger, Section 3.7. Steady periodic temperature in composite slabs, pp. 109-112, in *Conduction of Heat in Solids, 2nd (2003) Ed.* Vol. No. pp. 109-12, 1959.
51. A. Feldman, Algorithm for solutions of the thermal diffusion equation in a stratified medium with a modulated heating source, in *High Temperatures-High Pressures* Vol. 31, pp. 293-98, 1999.
52. R. M. Costescu, M. A. Wall and D. G. Cahill, Thermal conductance of epitaxial interfaces, in *Phys. Rev. B* Vol. 67, p. 054302, 2003.
53. C. Chiritescu, D. G. Cahill, C. Heibeman, Q. Lin, c. Mortensen, N. T. Nguyen, D. Johnson, R. Rostek and H. Bottner, Low thermal conductivity in nanoscale layered materials synthesized by the method of modulated elemental reactants, in *J. Appl. Phys.* Vol. 104, p. 033503, 2008.
54. R. M. Costescu, A. J. Bullen, G. Matamis, K. E. O'Hara and D. G. Cahill, Thermal conductivity and sound velocities of hydrogen-silsequioxane low-*k* dielectrics, in *Phys. Rev. B* Vol. 65, p. 094205, 2002.

55. Y. K. Koh, Y. Cao, D. G. Cahill and D. Jena, Heat-transport mechanisms in superlattices, in *Adv. Func. Mat.* Vol. 19, pp. 610-15, 2009.
56. P. E. Hopkins, Effects of electron-boundary scattering on changes in thermoreflectance in thin metal films undergoing intraband transitions, in *J. Appl. Phys.* Vol. 105, p. 093517, 2009.
57. Y. Ezzahri, S. Grauby, S. Dilhaire, J. M. Rampnoux and W. Claeys, Cross-plan Si/SiGe superlattice acoustic and thermal properties measurement by picosecond ultrasonics, in *J. Appl. Phys.* Vol. 101, p. 013705, 2007.
58. D. G. Cahill, W. K. Ford, K. E. Goodson, G. D. Mahan, A. Majumdar, H. J. Maris, R. Merlin and S. R. Phillpot, Nanoscale thermal transport, in *J. Appl. Phys.* Vol. 93, No. 2, pp. 793-818, 15 January 2003.
59. D. G. Cahill, K. E. Goodson and A. Majumdar, Thermometry and thermal transport in micro/nanoscale solid-state devices and structures, in *J. Heat Transfer* Vol. 124, pp. 223-41, 2002.
60. R. J. Stevens, A. N. Smith and P. M. Norris, Signal analysis and characterization of experimental setup for the transient thermoreflectance technique, in *Review of Scientific Instruments* Vol. 77, p. 084901, 2006.
61. A. J. Schmidt, Optical characterization of thermal transport from the nanoscale to the macroscale, in *Mechanical Engineering* Vol. Doctor of Philosophy, No. pp. 2008.
62. A. J. Schmidt, R. Cheaito and M. Chiesa, A frequency-domain thermoreflectance method for the characterization of thermal properties, in *Review of Scientific Instruments* Vol. 80, p. 094901, 2009.
63. P. E. Hopkins, J. R. Serrano, L. M. Phinney, S. P. Kearney, T. W. Grasser and C. T. Harris, Criteria for cross-plane dominated thermal transport in multilayer thin film systems during modulated laser heating, in *J. Heat Transfer* Vol. 132, p. 081302, 2010.
64. F. Incropera and D. P. DeWitt, *Fundamentals of Heat and Mass Transfer*. Wiley and Sons, Inc., New York City, NY, 1996.
65. C. Thomsen, J. Strait, Z. Vardeny, H. J. Maris, J. Tauc and J. J. Hauser, Coherent phonon generation and detection by picosecond light pulses, in *Phys. Rev. Lett.* Vol. 53, pp. 989-92, 1984.
66. C. Thomsen, H. T. Grahn, H. J. Maris and J. Tauc, Surafce generation and detection of phonons by picosecond light pulses, in *Phys. Rev. B* Vol. 34, pp. 4129-38, 1986.
67. A. N. Smith, J. L. Hostetler and P. M. Norris, Nonequilibrium heating in metal films: an analytical and numerical analysis, in *Numerical Heat Transfer, Part A* Vol. 35, No. 8, pp. 859-73, 1999.
68. A. Eucken, Forschung auf dem Gebiete des Ingenieurwesens, in Vol. No. pp. 3/4 VDI Forschungsheft 353, 1932.
69. Y. S. Ju and K. E. Goodson, Phonon scattering in silicon films with thickness of order 100 nm, in *Appl. Phys. Lett.* Vol. 74, No. 20, pp. 3005-07, 1999.

APPENDIX A: PUBLICATIONS, CONFERENCES, AND AWARDS

A.1. Journal Publications

1. C. M. Reinke, M. F. Su, R. H. Olsson III, and I. El-Kady, "Realization of optimal bandgaps in solid-solid, solid-air, and hybrid solid-air-solid phononic crystal slabs," *Applied Physics Letters,* vol. 98, p. 061912, 2011.
2. P. E. Hopkins, L. M. Phinney, P. T. Rakich, R. H. Olsson, and I. El-Kady, "Phonon considerations in the reduction of thermal conductivity in phononic crystals," *Applied Physics A,* vol. 103, pp. 575-579, 2011.
3. M. F. Su, R. H. Olsson, Z. C. Leseman, and I. El-Kady, "Realization of a phononic crystal operating at gigahertz frequencies," *Applied Physics Letters,* vol. 96, p. 053111, 2010.
4. Y. M. Soliman, M. F. Su, Z. C. Leseman, C. M. Reinke, I. El-Kady, and R. H. Olsson III, "Phononic crystals operating in the gigahertz range with extremely wide band gaps," *Applied Physics Letters,* vol. 97, pp. 193502-1-3, 2010.
5. Y. M. Soliman, M. F. Su, Z. C. Leseman, C. M. Reinke, I. El-Kady, and R. H. Olsson III, "Effects of release holes on microscale solid-solid phononic crystals," *Applied Physics Letters,* vol. 97, p. 081907, 2010.
6. P. E. Hopkins, C. M. Reinke, M. F. Su, R. H. Olsson, E. A. Shaner, Z. C. Leseman, J. R. Serrano, L. M. Phinney, and I. El-Kady, "Reduction in the thermal conductivity of single crystalline silicon by phononic crystal patterning," *Nano Letters,* vol. 11, pp. 107-112, 2010.
7. D. Goettler, M. Su, Z. Leseman, Y. Soliman, R. Olsson, and I. El-Kady, "Realizing the frequency quality factor product limit in silicon via compact phononic crystal resonators," *Journal of Applied Physics,* vol. 108, p. 084505, 2010.
8. R. H. Olsson III and I. El-Kady, "Microfabricated phononic crystal devices and applications," *Measurement Science & Technology,* vol. 20, p. 012002, 2009.
9. P. E. Hopkins, P. T. Rakich, R. H. Olsson III, I. F. El-kady, and L. M. Phinney, "Origin of reduction in phonon thermal conductivity of microporous solids," *Applied Physics Letters,* vol. 95, p. 161902, 2009.
10. R. H. Olsson III, I. F. El-Kady, M. F. Su, M. Tuck, and J. G. Fleming, "Microfabricated VHF acoustic crystals and waveguides," *Sensors and Actuators A (Physical),* vol. 145-146, pp. 87-93, 2008.

A.2. Conferences

A.2.1. Organized Conferences

Phononics 2011: 1st International Conference on Phononic Crystals, Metamaterials, and Optomechanics, Santa Fe, NM, May 19 - June 2, 2011.

A.2.2. Conference Presentations

1. C. M. Reinke, M. F. Su, R. H. Olsson III, Z. C. Leseman, M. Hussein, and I. El-Kady, “Computationally efficient plane-wave expansion band structure calculations for phononic

crystal devices," *ASME 2011 International Mechanical Engineering Conference and Exposition*, Denver, CO, 2011.

2. D. F. Goettler, P. Hopkins, "Reduction of thermal conductivity in silicon via ion implantation and phononic crystal patterning," *ASME 2011 International Mechanical Engineering Conference and Exposition*, Denver, CO, 2011.
3. C. T. Harris, B. Kim, C. M. Reinke, P. E. Hopkins, R. H. Olsson III, I. El-Kady, E. A. Shaner, and J. Sullivan, "Thermal conductivity measurements of silicon thin films with periodically arrayed nanoscale perforations," *ASME 2011 International Mechanical Engineering Conference and Exposition*, Denver, CO, 2011.
4. B. L. Davis and M. I. Hussein, "Thermal transport studies of silicon-based phononic-crystal thin films," *ASME 2011 International Mechanical Engineering Conference and Exposition*, Denver, CO, 2011.
5. I. El-Kady, M. F. Su, C. M. Reinke, P. E. Hopkins, E. A. Shaner, R. H. Olsson III, D. F. Goettler, and Z. C. Leseman, "Manipulating thermal phonons: a phononic crystal route to hi-ZT thermoelectrics," *ASME 2011 International Mechanical Engineering Conference and Exposition*, Denver, CO, 2011.
6. M. F. Su, D. F. Goettler, Z. C. Leseman, C. M. Reinke, R. H. Olsson III, and I. El-Kady, "Designing high-Q phononic crystal resonators," *ASME 2011 International Mechanical Engineering Conference and Exposition*, Denver, CO, 2011.
7. R. H. Olsson III, M. Ziaei-Moayyed, B. Kim, C. M. Reinke, I. El-Kady, M. F. Su, D. F. Goettler, and Z. C. Leseman, "Microfabricated phononic crystal devices for radio frequency communications," *ASME 2011 International Mechanical Engineering Conference and Exposition*, Denver, CO, 2011.
8. M. Ziaei-Moayyed, C. M. Reinke, M. F. Su, I. El-Kady, and R. H. Olsson III, "Silicon carbide phononic crystals for RF and microwave communication systems," *ASME 2011 International Mechanical Engineering Conference and Exposition*, Denver, CO, 2011.
9. D. F. Goettler, S. Alaie, and Z. C. Leseman, "Effect of phononic crystal lattice on thermal conductivity in silicon," *ASME 2011 International Mechanical Engineering Conference and Exposition*, Denver, CO, 2011.
10. S. Alaie, I. El-Kady, Z. C. Leseman, "On the validity of 2D numerical simulation of bandgap for slab of phononic crystals," *Phononics 2011 - 1st International Conference on Phononic Crystals, Metamaterials, and Optomechanics*, Santa Fe, NM, 2011.
11. T. E. Beechem, P. E. Hopkins, C. M. Reinke, M. F. Su, B. Kim, C. T. Harris, D. Goettler, M. Ziaei-Moayyed, E. A. Shaner, Z. C. Leseman, R. H. Olsson III, A. McGaughey, and I. El-Kady, "Thermal conductivity reduction in phononic crystals: interplay of coherent versus incoherent scattering," *Phononics 2011 - 1st International Conference on Phononic Crystals, Metamaterials, and Optomechanics*, Santa Fe, NM, 2011.
12. B. Kim, J. Nguyen, E. A. Shaner, I. El-Kady, and R. H. Olsson III, "Thermal conductivity reduction in lithographically patterned single crystal silicon phononic crystal structures," *Phononics 2011 - 1st International Conference on Phononic Crystals, Metamaterials, and Optomechanics*, Santa Fe, NM, 2011.
13. R. H. Olsson III, B. Kim, M. Ziaei-Moayyed, C. M. Reinke, M. F. Su, Y. M. Soliman, Z. C. Leseman, and I. El-Kady, "Micromachined phononic band-gap crystals and devices," *Phononics 2011 - 1st International Conference on Phononic Crystals, Metamaterials, and Optomechanics*, Santa Fe, NM, 2011.

14. D. F. Goettler, M. F. Su, R. H. Olsson III, I. El-Kady, and Z. C. Leseman, "Fabrication of 2-D phononic crystals via focused ion beam," *Phononics 2011 - 1st International Conference on Phononic Crystals, Metamaterials, and Optomechanics*, Santa Fe, NM, 2011.
15. D. F. Goettler, B. Kim, R. H. Olsson III, Z. C. Leseman, C. M. Reinke, and I. El-Kady, "The effect of phononic crystal lattice type and lattice spacing on the reduction of bulk thermal conductivity in silicon and silicon nitride," *Phononics 2011 - 1st International Conference on Phononic Crystals, Metamaterials, and Optomechanics*, Santa Fe, NM, 2011.
16. M. Ziaei-Moayyed, C. M. Reinke, M. F. Su, I. El-Kady, and R. H. Olsson III, "Silicon carbide phononic crystals for communication, sensing, and energy management," *Phononics 2011 - 1st International Conference on Phononic Crystals, Metamaterials, and Optomechanics*, Santa Fe, NM, 2011.
17. M. F. Su, D. F. Goettler, Z. C. Leseman, and I. El-Kady, "Designing high-Q compact phononic crystal resonators," *Phononics 2011 - 1st International Conference on Phononic Crystals, Metamaterials, and Optomechanics*, Santa Fe, NM, 2011.
18. M. Ziaei-Moayyed, M. F. Su, C. Reinke, I. F. El-Kady, and R. H. Olsson III, "Silicon carbide phononic crystal cavities for micromechanical resonators," *2011 IEEE 24th International Conference on Micro Electro Mechanical Systems (MEMS 2011),* pp. 1377-13811381, 2011.
19. I. El-Kady, M. F. Su, C. M. Reinke, P. E. Hopkins, D. Goettler, Z. C. Leseman, E. A. Shaner, and R. H. Olsson III, "Manipulation of thermal phonons: a phononic crystal route to high-ZT thermoelectrics," *Photonics West 2011 - Proceedings of the SPIE,* vol. 7946, p. 794615, 2011.
20. C. Reinke, I. El-Kady, E. Shaner. M. Su, R. Camacho, D. Goettler, P. Hopkins, R. Olsson, and Z. Leseman. "Implications and applications of manipulating phonons from the thermal to the RF domain," *ASME 2010 International Mechanical Engineering Congress & Exposition*, Vancouver, CA, 2010.
21. C. M. Reinke, M. Su, M. Ziaei-Moayyed, R. H. Olsson III, and I. El-Kady, "Investigation of Full bandgaps in silicon phononic crystal membranes with tungsten and air inclusions," *2010 International Ultrasonics Symposium,* pp. 519-522522, 2010 2010.
22. M. Ziaei-Moayyed, M. F. Su, C. M. Reinke, I. El-Kady, and R. H. Olsson III, "Silicon carbide phononic crystals for ultrahigh f.Q micromechanical resonators," *2010 International Ultrasonics Symposium,* pp. 519-522522, 2010 2010.
23. R. H. Olsson III, M. F. Su, P. T. Rakich, and I. El-Kady, "Micro and nano fabricated phononic crystals: technology and applications," *META '10 - 2nd International Conference on Metamaterials, Photonic Crystals and Plasmonics*, Cairo, Egypt, 2010.
24. Y. M. Soliman, D. F. Goettler, Z. C. Leseman, I. El-Kady, and R. H. Olsson III, "Effects of release hole size on microscale phononic crystals," *SEM 2009 Annual Conference & Exposition on Experimental & Applied Mechanics*, Albuquerque, NM, 2009.
25. D. Goettler, Y. Soliman, M. Su, R.H. Olsson III, Z. C. Leseman, and I. El-Kady, "Theoretical study of phononic bandgaps in multiple lattices and directions," *2009 MRS Fall Meeting & Exhibit*, Boston, MA, 2009.
26. Y. Soliman, D. Goettler, M. Su, I. El-Kady, Z. C. Leseman, and R. H. Olsson III, "Release Holes Size Effects in Acoustic Bandgap Crystals," *2009 MRS Fall Meeting & Exhibit*, Boston, MA, 2009.
27. R. H. Olsson III, S. X. Griego, I. El-Kady, M. Su, Y. Soliman, D. Goettler, and Z. Leseman, "Ultra high frequency (UHF) phononic crystal devices operating in mobile communication bands," in *IEEE International Ultrasonics Symposium*, Rome, Italy, 2009, pp. 1150-1153.

A.1. Patents

R. H. Olsson III, I. El-Kady, P. E. Hopkins, C. M. Reinke, and B. Kim, “Synthetic Thermoelectric Materials Comprising Phononic Crystals,” SD#: 10663, 06/09/2011 (provisional).

DISTRIBUTION

1 Dept. of Mechanical and Aerospace Engineering
University of Virginia
Attn: P. Hopkins
122 Engineer's Way, Room 331
Charlottesville, VA 22904-4746

1	MS0885	T. Aselage	1810
1	MS1069	R. Olsson	1719
1	MS1069	Z. Leseman	1719
1	MS1069	B. Kim	1719
1	MS1069	M. Ziaei-Moayyed	1719
1	MS1071	C. Boye	1720
1	MS1078	W. Hermina	1710
1	MS1079	G. Herrera	1700
1	MS1080	D. Goettler	1719
1	MS1082	M. Descour	1725
3	MS1082	I. El-Kady	1725
1	MS1082	C. Reinke	1725
1	MS1415	F. McCormick	1110
1	MS1415	E. Shaner	1128
1	MS1415	T. Beechem	1112

1	MS 0359	D. Chavez, LDRD Office	1911
1	MS0161	Legal Technology Transfer Center	11500
1	MS 0899	RIM-Reports Management	9532 (electronic copy)

Sandia National Laboratories